

# **GAS PHASE RAMAN SPECTROSCOPY USING HOLLOW WAVEGUIDES**

by

**Michael Paul Buric**

B.S. in Electrical Engineering, University of Pittsburgh, 2003

M.S. in Electrical Engineering, University of Pittsburgh, 2005

Submitted to the Graduate Faculty of  
The Swanson School of Engineering in partial fulfillment  
of the requirements for the degree of  
Doctor of Philosophy in Electrical Engineering

University of Pittsburgh

2010

UNIVERSITY OF PITTSBURGH  
SWANSON SCHOOL OF ENGINEERING

This dissertation was presented

by

Michael Buric

It was defended on

March 19th, 2010

and approved by

Kevin Chen, PhD, Electrical and Computer Engineering

Steven Woodruff, PhD, Department of Energy, NETL

William Stanchina, PhD, Electrical and Computer Engineering

Hong-Koo Kim, PhD, Electrical and Computer Engineering

Minhee Yun, PhD, Electrical and Computer Engineering

David Snoke, PhD, Physics and Astronomy

Dissertation Director: Joel Falk, PhD, Electrical and Computer Engineering

Copyright © by Michael Buric

2010

# **GAS PHASE RAMAN SPECTROSCOPY USING HOLLOW WAVEGUIDES**

Michael Buric, PhD

University of Pittsburgh, 2010

The detection and characterization of molecular gases in a given sample is a relatively difficult challenge. Usually, this task is relegated to expensive and time consuming processes like mass spectrometry and gas chromatography. Furthermore, numerous industrial applications require such gas-phase analysis for pollution and process control. In particular, the operation of large natural gas-fired turbine generators requires real-time analysis of constituent hydrocarbon concentration in order to provide energy content information about the gaseous fuel, and subsequently, inputs for controlling fuel/air ratio and burner temperature. Herein, a novel technique for studying gaseous samples is presented which uses a new collection method for Raman spectroscopy. In our technique, gasses are introduced inside the light-guiding core of a hollow waveguide. Either lengths of hollow-core photonic-bandgap fiber or internally reflective capillary waveguides are used to both contain sample gases and collect Raman photons. The optical confinement characteristics of these types of hollow-waveguides allow a high power-density laser beam to propagate a long distance along with the low-volume gaseous sample. We have shown analytically that the Raman signal strength (power) collected using our gas cells can be hundreds of times larger than that which can be obtained in free-space. Along with this improvement in collected Raman power comes shorter minimum interrogation times and higher sensitivities to trace

gasses. In general, the technique paves the way for the construction of a gas Raman spectrometer with low-cost components and high-accuracy.

## TABLE OF CONTENTS

<b>PREFACE</b> .....	<b>XV</b>
<b>1.0 INTRODUCTION TO GAS SENSING</b> .....	<b>1</b>
<b>1.1 GAS SENSING TECHNIQUES</b> .....	<b>2</b>
<b>1.2 RAMAN SPECTROSCOPY</b> .....	<b>7</b>
<b>1.3 DISSERTATION ORGANIZATION</b> .....	<b>11</b>
<b>2.0 RAMAN CONFIGURATIONS AND POWERS</b> .....	<b>13</b>
<b>2.1 COLLECTING SCATTERED POWER</b> .....	<b>13</b>
<b>2.2 GAS RAMAN MEASUREMENTS WITH A SPECTROMETER</b> .....	<b>15</b>
<b>2.3 RAMAN COLLECTION IN A WAVEGUIDE</b> .....	<b>18</b>
<b>2.4 WAVEGUIDE LOSS AND DIRECTION</b> .....	<b>20</b>
<b>2.5 PRINCIPLES OF PHOTONIC BANDGAP FIBER</b> .....	<b>23</b>
<b>2.6 RAMAN COLLECTION IN A PBF</b> .....	<b>28</b>
<b>3.0 ATMOSPHERIC RAMAN EXPERIMENTS</b> .....	<b>33</b>
<b>3.1 FREE SPACE ATMOSPHERIC COLLECTION</b> .....	<b>34</b>
<b>3.2 FORWARD SCATTERING IN HC-PBF</b> .....	<b>38</b>
<b>3.3 BACKWARD SCATTERING IN HC-PBF</b> .....	<b>45</b>
<b>3.4 DETECTORS AND THEIR CHARACTERISTICS</b> .....	<b>47</b>
<b>4.0 HYDROCARBON SENSING AND NOISE REDUCTION</b> .....	<b>54</b>
<b>4.1 VISIBLE WAVELENGTH FORWARD SCATTERING</b> .....	<b>55</b>
<b>4.2 VISIBLE WAVELENGTH BACKWARD SCATTERING</b> .....	<b>62</b>
<b>4.3 NEAR-IR BACKSCATTERING</b> .....	<b>70</b>

4.4	SILICA RAMAN NOISE REDUCTION .....	77
5.0	GAS FLOW AND DYNAMICS IN PBF.....	85
5.1	PRINCIPLES OF CAPILLARY GAS FLOW .....	85
5.2	HC-PBF SENSOR RESPONSE TIME.....	91
6.0	MICRO-VOLUME GAS RAMAN.....	96
6.1	GAS CHROMATOGRAPHY BACKGROUND.....	97
6.2	THE HYBRID GC-RAMAN SYSTEM.....	100
6.3	GC RAMAN SENSOR EXPERIMENTS.....	102
6.4	CLADDING SEALS AND CONTAMINATION .....	110
7.0	METAL LINED CAPILLARY WAVEGUIDE THEORY .....	115
7.1	MULTIMODE WAVEGUIDE COLLECTION.....	116
7.2	REFLECTIVE WAVEGUIDE MODES .....	119
7.3	LARGE WAVEGUIDE DETECTOR MATCHING .....	131
8.0	RAMAN SENSING EXPERIMENTS USING METAL-LINED CAPILLARY WAVEGUIDES.....	142
8.1	CAPILLARY RAMAN SPECTRA AND NOISE .....	143
8.2	SUPPORT FOR CAPILLARY RAMAN THEORIES .....	151
8.3	FURTHER CAPILLARY CHARACTERIZATION.....	156
9.0	INSTRUMENTATION ENGINEERING.....	161
9.1	SHORT WAVELENGTH PUMPING.....	162
9.2	SPECTROMETER ALTERNATIVES .....	169
9.3	CONCLUSIONS AND SUMMARY .....	176
	BIBLIOGRAPHY .....	179

## LIST OF TABLES

Table 1 – Raman cross-sections of common gases [2,29] .....	10
Table 2. Molecular Diameters [2] .....	88
Table 3 - Estimated detection limits (PPM) for different systems.....	159

## LIST OF FIGURES

Figure 1 Spontaneous Raman energy transitions [46] .....	8
Figure 2 - Traditional Raman collection configurations.....	16
Figure 3 Cross section of an HC-PBF [41].....	24
Figure 4 - Periodicity schematic: 1D Bragg Grating, 2D Periodic Structure, and 3D Photonic Crystal [45] .....	24
Figure 5 - PBF drawing procedure [48].....	26
Figure 6 – Figures of merit for PBF [48].....	27
Figure 7 – Commercial HC-PBF transmission bands [41,42] .....	28
Figure 8 – Free space Raman collection system. The pump beam is positioned $2*f$ from $L_2$ and $L_2$ is positioned $2f$ from the spectrometer entrance slits, where $f$ is the focal length of $L_2$ . .....	34
Figure 9 – Holographic edge filter transmission spectrum [49] .....	35
Figure 10 – Czerny-Turner spectrometer internal light path [50], A: Input, B: Entrance slits, C: Collimating Mirror, D: Dispersion grating, E: Focusing mirror, F: Detector plane or slits, G: Output.....	36
Figure 11 – Free space Raman spectrum .....	37
Figure 12 – Forward scattering experimental setup.....	39
Figure 13 – Fiber-to-fiber butt-coupling schematic.....	39
Figure 14 – PBF forward scattering spectrum in air.....	41

Figure 15 – Silica Raman spectrum from fused silica fiber. The x-axis is reversed and scaled in terms of wave-numbers instead of wavelength [51].....	43
Figure 16 – Modified forward scattering configuration .....	43
Figure 17 – Modified forward scattering spectrum in air .....	44
Figure 18 – Backward scattering Raman collection system .....	45
Figure 19 – PBF backward scattering spectrum in air. Raman lines are visible from nitrogen and oxygen in ambient air. A background of silica Raman is present along with some residual pump-light.....	46
Figure 20 – Typical PMT components [53].....	48
Figure 21 – PMT pulse distribution [55] .....	50
Figure 22 – Common photodiode responsivities [52].....	51
Figure 23 – Experimental setup, forward scattering.....	55
Figure 24 – Microscope image, fiber-to-fiber butt-coupling.....	56
Figure 25 – Forward scattering single gas spectra.....	58
Figure 26 – Forward scattering, multi-hydrocarbon spectra.....	60
Figure 27 – Backscattering system with gas handling.....	63
Figure 28 – 1D CCD array pixel data (spectra). a) CH <sub>4</sub> spectrum centered at 605.4nm and b) CO <sub>2</sub> spectrum centered at 551nm .....	65
Figure 29 – Methane rotational substructure about the 2917cm <sup>-1</sup> line .....	66
Figure 30 – CO <sub>2</sub> Raman peak magnitude versus gas concentration.....	67
Figure 31 – A) top: methane 2917cm <sup>-1</sup> Raman line intensity (counts/.02s) and B) bottom: CO <sub>2</sub> 1388cm <sup>-1</sup> Raman line intensity (counts/.05s) under varying gas pressure. B) includes a plot recorded under descending pressure without vacuum at the output to illustrate residual gases in the fiber.....	69
Figure 32 – Near IR backscattering system based on HC-800 fiber.....	71
Figure 33 – 785nm Microlaser L4785-95-TE output spectrum.....	71

Figure 34 – Ti:sapphire efficiency and output power, beamsplitter transmission (90 degree), and HC-800 fiber transmission .....	73
Figure 35 – 2D cooled silicon CCD array detector noise .....	74
Figure 36 – Vacuum spectrum .....	75
Figure 37 – Single gas spectra (top left to bottom right): nitrogen, methane, ethane, propane, carbon dioxide .....	76
Figure 38 - HC-580 mode field pattern [41] .....	78
Figure 39 PBF spatial filtering experimental setup .....	79
Figure 40 – Atmospheric Raman spectra; a) no spatial filtering b) 10 $\mu$ m spatial filter in the image plane .....	79
Figure 41 – 2D Raman scattering image in air .....	83
Figure 42 – Methane rotational Raman spectrum .....	84
Figure 43 – Flow regimes and Knudsen Number [34] .....	87
Figure 44 – HC-PBF predicted filling times .....	90
Figure 45 – Predicted time evolution of PBF pressure [34] .....	91
Figure 46 – Raman peak response to gas flow .....	92
Figure 47 – Methane Raman filling (top) /evacuation (bottom) times with changing temperature .....	93
Figure 48 – Nitrogen filling/evacuation times, HC-800 .....	94
Figure 49 - Common gas chromatography system components .....	98
Figure 50 - Example GC trace from a natural gas mixture .....	99
Figure 51 - Diagram of proposed GC Raman hybrid system .....	100
Figure 52 - Experimental Raman GC sensor components .....	102
Figure 53 -GC Raman spectral/time response to applied CO <sub>2</sub> .....	104
Figure 54 - CO <sub>2</sub> Raman line time-response for various injector volumes .....	105
Figure 55 - Normalized Raman GC sensor response .....	106

Figure 56 - Raman GC sensor system flow diagram with component volumes.....	107
Figure 57 - CO <sub>2</sub> and Ethane time response in the GC/Raman sensor .....	108
Figure 58 - GC/Raman sensor response with He and N <sub>2</sub> carrier gasses.....	109
Figure 59 - Micro-injection and bulk gas transfer speed comparison .....	110
Figure 60 - SEM micrograph of fusion-sealed PBF .....	112
Figure 61 - Magnitude of the transverse electric field of the EH <sub>11</sub> mode in a dielectric waveguide .....	117
Figure 62 - Silver, gold, and aluminum reflectivity at normal incidence .....	118
Figure 63 - Method of silver tubing plating in small diameter capillaries [61].....	119
Figure 64 - Reflective capillary waveguide diagram.....	120
Figure 65 - Example mode loss vs. angle in a hollow guide. Inset: blowup of data from 0-20°. About 726 modes propagate below 60°. .....	125
Figure 66 - Collectable Stokes Raman power from a 320µm I.D. 1-m long silver-lined capillary.....	126
Figure 67 - Collectable Stokes power normalized with respect to species and laser power vs. angle for different hollow-waveguide lengths .....	127
Figure 68 - Collectable Stokes power normalized with respect to species and laser power vs. angle for different hollow-waveguide diameters .....	128
Figure 69 - Collectable Stokes power calculated using the characteristic equations or the Crenn simplification.....	131
Figure 70 – Single-mode coupling and magnification.....	133
Figure 71 - Fiber bundle diagram: individual fibers shown in different colors.....	137
Figure 72 - Fiber bundle design example .....	140
Figure 73 - Diagram of experimental capillary Raman system .....	144
Figure 74 - Preliminary capillary Raman spectrum, A: Nitrogen line centered at 584.5nm with mercury calibration lines at 577 and 579nm. B: Oxygen line at 559nm. ..	146

Figure 75 - Raman spectrum from an air filled capillary, 514.5nm pump wavelength, 320 $\mu$ m ID, 1-m long.....	147
Figure 76 - Raman spectrum from an air filled silver-lined capillary, 320 $\mu$ m ID, 1-m long, 775nm pump wavelength.....	148
Figure 77 - Capillary noise sources .....	149
Figure 78 - 659nm laser diode spectrum.....	150
Figure 79 - CCD array detector image of 659nm pumped, 1-m long, 320 $\mu$ m ID silver-lined capillary with 75psi N <sub>2</sub> . x-axis: wavelength, y-axis: real image space .....	150
Figure 80 - Capillary input/output polarization .....	152
Figure 81 - Angular dependence of collected Stokes power from a silver-lined 320 $\mu$ m ID capillary.....	154
Figure 82 - 632.8nm HeNe laser power throughput in a 530 $\mu$ m ID 2-m long silver-lined capillary measurements are labeled with $\diamond$ symbols, and the simulation is shown with the solid red curve.....	155
Figure 83 - Methane Raman line rise time in silver-lined capillaries A: 320 $\mu$ m ID 150psi, diode array recording B: 530 $\mu$ m ID 200psi, single photodiode recording .....	157
Figure 84 - Reference 'air' spectrum for SNR determination, 100mm efl pump launch lens, linear Background Subtraction, 514.5nm Pump, 1second integration, .1mm and .5mm slits.....	158
Figure 85 - BlueRay laser diode spectra (a) and peak wavelength (b).....	164
Figure 86 - TEC temperature and thermocouple resistance.....	164
Figure 87 - Initial 405nm pumped Raman spectrum in PBF (no gas-Raman lines discernable) .....	166
Figure 88 - Silica Raman noise in HC-440 fiber .....	167
Figure 89 - Atmospheric Raman inside HC-440 with a ~405nm pump .....	168
Figure 90 - Example gas-Raman spectrum recorded on a miniature spectrometer [79] .....	171
Figure 91 - Multi-line gas Raman detection without a spectrometer.....	174

Figure 92 - Spectrometer-less instrument operation with methane.  $\diamond$  -data points recorded with the spectrometer operating with a 3nm bandwidth.  $\square$  – data points recorded without the spectrometer using a 15nm bandpass filter..... 175

## **PREFACE**

I would like to thank Kevin Chen and Joel Falk for their guidance and teaching during my time at Pitt and their extensive work on this project. I would also like to thank Ben McMillen, Chuck Jewart, Di Xu, Tong Chen, Baujun Liu, and Qing Qing Wang for their help in the lab. I would like to recognize Steve Woodruff at NETL for collaborating with us and conducting excellent research. Finally, thanks to my mom and my family for their ongoing support and encouragement.

## 1.0 INTRODUCTION TO GAS SENSING

Let us assume that we are presented with a gaseous sample of unknown composition. Our goal is to determine the constituents of the sample, as well as the relative concentrations of those constituents to high accuracy. Furthermore, we would like an empirical update on those concentrations roughly every second. Currently, there are no existing techniques that can provide such short sampling time, along with complete indifference to the molecular species in the sample. The desire for this sort of gas-phase analysis provides the motivation for this dissertation, and has spawned a plethora of new techniques in optical spectroscopy.

In particular, we are motivated by a partnership with the Department of Energy to find sensing solutions to determine the composition of natural gas. In the United States, natural gas is produced and imported from a number of different sources. Although natural gas is primarily comprised of methane, it can contain up to about 10% of other hydrocarbon gases like ethane and propane [37]. Contaminants like oxygen, carbon dioxide, carbon monoxide, water vapor, and nitrogen usually occur in trace quantities. In most residential and commercial applications, simple burning of a natural gas mixture does not require a priori knowledge of the gas's thermal energy content or exact combustion characteristics. However, in large natural gas-fired turbine generators and other high-power high-temperature combustors, detailed information about the natural gas mixture is extremely useful. If the relative constituent concentrations in a natural gas mixture are known a priori, the thermal energy content and approximate flame-speed can be

extrapolated. This allows precise control of combustion equipment for maximizing efficiency and reducing pollutant emissions [2, 72-76].

In addition to allowing the optimization of burner parameters, detailed gas analysis helps prevent problems associated with natural gas importation. In practice, natural gas imported from overseas tends to contain much larger concentrations of non-methane hydrocarbons. This imported fuel can have a much higher BTU content than its domestic counterpart. When a ‘slug’ of such fuel reaches a natural gas turbine, it can quickly destabilize operation and result in severe damage to the turbine. This, of course, can also be avoided through the use of a quick and accurate gas analysis system. Given the current trend in the desire to produce synthetic fuels from coal, the introduction of syngas into American natural gas pipelines is becoming more and more likely [38]. In order to safely and effectively use this fuel, we will need to be able to measure its composition both during the manufacturing process, and in delivery lines. In addition to these two immediate applications, there are undoubtedly countless other industrial processes and research applications that would benefit from quick and accurate gas analysis. A plethora of possible applications exist in the monitoring of greenhouse gases, forensic trace gases, pharmaceutical reactions, mining, respiratory analysis, power transformer monitoring for electrical transmission, and industrial chemical production [2].

## **1.1 GAS SENSING TECHNIQUES**

In an attempt to better understand the challenges of fast and accurate gas sensing, we undertook a brief evaluation of existing techniques currently in use for gas composition analysis. Obviously, a number of well-proven gas sensor technologies are in use today. After a careful review, we

noted that each of these technologies has distinct disadvantages when applied to the quick analysis of natural gas or other samples of completely unknown composition. Some of the techniques evaluated included electrochemical sensors, mass spectrometry, gas chromatography, optical absorption, and Raman spectroscopy.

The most common gas-sensor in use around the world today is the simple electrochemical sensor. In such a sensor, a pair of chemically sensitized electrodes is housed inside a gas-permeable enclosure. The gas of interest oxidizes one of the electrodes and reduces the other, which creates a measurable voltage across the electrodes. The availability of inexpensive low-noise circuitry for the conversion of small electrical signals into recordable gas concentrations makes these sensors extremely inexpensive. In fact, electrochemical methods are the primary means for producing personal gas-safety monitors and environmental air quality monitoring systems.

Unfortunately, a number of significant drawbacks exist with regard to electrochemical sensors. First, such sensors rely on the induced oxidation/reduction reaction produced when a certain species diffuses into the sensor. This reaction is limited by a number of factors including the mechanical diffusion rate of gasses into the sensor. Relying on a constant diffusion rate to provide linear sensor output with concentration essentially limits such a device's measurable concentration range. It would probably be necessary to change a sensor's gas diffusion membrane in order to change the sensor's range from 0-100ppm to 1-100% for example. Secondly, the reality of relying on the rate of a chemical reaction to provide gas concentration information means that the sensor is usually susceptible to temperature and pressure changes. Foremost is the tendency of electrochemical sensors to falsely identify other species similar to the species of interest. For example, a simple carbon-dioxide sensor may erroneously report the

presence of CO<sub>2</sub> when it is in fact in the presence of carbon-monoxide. This prospect of cross-sensitivity makes electrochemical sensors wholly unsuitable for applications requiring careful discrimination between species. Finally, electrochemical reactions are notoriously slow, and such sensors are often intended to provide a reading in 30-60 seconds [4].

In the realm of trace-gas analysis, the gold standard is usually recognized to be the gas chromatography (GC) process. In gas chromatography, a sample is injected into a long narrow tube (known as a column) lined or packed with special structures designed to retain the sample for a short period of time. Samples are then forced through the tubing using an inert carrier gas, and detected and identified via a number of different techniques as they emerge from the other end of the chromatography column. There are a number of obvious drawbacks to this technique given the need for an elution column. First, the instrument is designed to allow the slow and metered flow of samples for careful measurement. Column retention times are often measured in minutes, and therefore are hundreds of times slower than needed for real-time monitoring. Secondly, numerous different types of columns, each having different retention characteristics, are required for use with various different compounds.

In addition to having difficulties brought on by long retention times and varied equipment for different compounds, gas chromatography still does not definitively provide identification of a molecular compound in and of itself. GC requires a variety of detectors, each designed to definitively identify compounds as they elute from the column. The most common detector is a flame-ionization detector, which relies on a hydrogen flame to ionize a combustible sample. The resulting ions are then measured with a sensitive ammeter. Current measurements essentially correspond to the proportion of reduced carbon atoms in the sample, which can be used for identification. This technique is extremely limited, and cannot be used to characterize non-

combustible gases at all. Also common to the GC process is the Thermal Conductivity Detector. This device is basically a heated element surrounded by a gaseous sample. Heat is lost by the element due to its surrounding's measurable conductivity, which can be used for identification. The obvious problem here is that numerous different compounds have approximately the same thermal conductivity, making the technique non-discriminatory.

In the defense of gas chromatography as a gas sampling technique, much can be said with respect to the merits of mass spectrometry and nuclear magnetic resonance (NMR) detection. A mass spectrometer is essentially any device that separates particles based solely on their mass to charge ratio. This means that mass spectrometers are definitive in species identification, as well as being capable of providing constituent concentration information. Unfortunately, using a mass-spectrometer to measure pipeline natural gas is a bit like using dynamite for trout-fishing. Mass spectrometers are prohibitive in cost and complexity that they will probably never be able to replace the other much cheaper sensor technologies. In addition, these devices are usually somewhat large due to the ion path and ion detection equipment necessary for operation. One can make similar comments about nuclear magnetic resonance detectors. Therein, a huge (usually super-cooled) magnet is needed to create measurable molecular resonances. Although NMR is definitive to particular molecules or even isotopes, it is far too complicated and expensive a technique for use in any sort of inexpensive portable device. In addition, both of these techniques are usually used at the output of a GC column, and therefore suffer the same speed drawbacks as any type of GC [3].

In light of the other gas detection techniques described above, absorption spectroscopy is probably the most promising and appropriate technique for use with different molecular gases of interest. In essence, every molecule absorbs light at specific wavelengths determined by the

vibrational or rotational structure of the molecule itself. This results in sharp bands of attenuation which can be used for gas detection. The transmittance  $T$  (ratio of throughput intensity to input intensity) of light passing through a given sample follows the Beer-Lambert law:

$$\text{Equation 1: } T = \frac{I_1}{I_0} = e^{-\alpha \cdot l} = e^{-n \cdot l \cdot \sigma}$$

where  $\sigma$  is the absorption cross section at a particular wavelength,  $n$  is the concentration of the species being measured, and  $l$  is the interaction length. In practice, absorption spectroscopy is usually a rather simple process involving a light source, a sample cell, and a detector. Of course, it is necessary to employ a light source with a wavelength overlapping at least one absorption line in the sample. If all possible samples are considered, a non-gas-specific absorption cell would need to employ numerous light sources covering a large spectrum from X-ray to IR. Also, the narrow nature of molecular absorption lines means that a narrow linewidth laser or optical dispersive element is required for measurements. The best absorption measurement systems employ wavelength-tunable lasers that allow comparison of the absorbed to fully-transmitted signal. Very accurate systems employ sinusoidal wavelength tuning and second-harmonic detection for the elimination of noise. Unfortunately, currently available tunable lasers offer extremely limited tuning ranges, making a single source for the detection of all species impossible [5].

Although absorption spectroscopy can be used to identify any gas, it may be necessary to have several light sources and detectors present to do so. For many applications, infrared absorption spectroscopy provides enough information about particular compounds of interest to disregard other portions of the spectrum. Because a broad spectrum of IR light is easily produced using a heated filament, and large portions of that spectrum can be quickly measured

using a scanning interferometer and single detector, FTIR (Fourier Transform Infrared Spectroscopy) has become the most popular method of conducting absorption measurements. Despite its advantages, the FTIR system still only measures IR absorptions. In addition, it usually requires an expensive IR detector and cryogenic cooling to eliminate local heat-noise.

## 1.2 RAMAN SPECTROSCOPY

In the search for suitable gas sensing technologies, it was determined that Raman scattering exhibited many of the characteristics necessary for wide-ranging applications. Before we can detail the utility of the technique and its applications, we must first conduct a brief review of Raman scattering in general, along with some discussion of the drawbacks of these sorts of optical sensing systems.

Raman scattering is an optical process inherent in nature which has the ability to characterize or differentiate various molecules based upon the vibrational or rotational energy quantization in all matter. Figure 1 schematically depicts this process in which light interacts with matter in Raman interactions. One of several things can happen when a photon of a particular wavelength with corresponding radian frequency  $\omega_{\text{pump}}$  strikes an atom or molecule. The photon may be scattered elastically (not gaining or losing energy as a result of its collision), or it may undergo an inelastic scattering process (in which it either gains or loses energy from the molecule with which it recently collided). There is a relatively small chance that the photon in question will undergo Raman scattering. This is a process in which the incident photon emerges after the collision with a frequency shifted by exactly the same frequency separating two of the molecule's vibrational or rotational energy levels. The green line in Figure 1 depicts

Stokes scattering. Therein, the incident photon is absorbed and re-emitted with a frequency equal to its original frequency minus the natural vibrational frequency of the target molecule. In the purple line in Figure 1, the incident photon is absorbed and re-emitted with a frequency equal to its original frequency plus the molecule's first vibrational frequency. This is known as anti-stokes scattering.

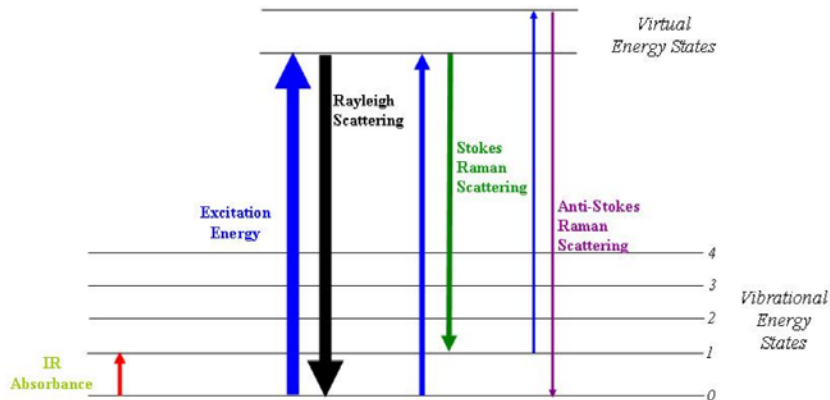


**Figure 1 Spontaneous Raman energy transitions [46]**

Several important revelations may ensue from this brief description. First, we note that Raman scattering is an observed shift in incident radiation towards longer or shorter wavelengths. This shift is defined by the vibrational (or rotational) characteristics of the target molecule itself. Therefore, if a species is Raman active, it's Raman spectrum will be indicative of that species. Many species are in fact Raman active; which makes the technique valuable and discriminatory for numerous solids, liquids, and gasses. Finally, we see that the resultant Stokes and anti-Stokes radiation is centered about the excitation wavelength, ensuring that detection is simplified through appropriate choices in pump wavelength.

As with any probe-and-measurement technique, there are a myriad of problems when applied to sensor technology. Raman is no exception. Firstly, Raman scattering is by definition a scattering process. Raman photons are emitted from a target sample in all directions. This makes Raman photons rather difficult to capture in an optical system and subsequently measure

(as we will see in Chapter 2). Similar to Brillouin scattering or third-harmonic generation, Raman scattering is a higher-order nonlinear optical process. All such phenomena are usually weak effects in nature. Furthermore, we note that anti-Stokes radiation is much weaker than Stokes radiation due to the fact that a photon must strike an atom already in an excited molecular-state (that hasn't emitted or relaxed yet). Anti-Stokes radiation is then weaker by a factor of  $e^{-h\nu/(kT)}$  (where  $h$  is Planck's constant,  $\nu$  is the photon energy,  $k$  is Boltzmann's constant, and  $T$  is the temperature).

Historically, Raman scattering is rather difficult to observe. The first such observations were carried out by C.V. Raman in 1928. His original observations were made well before the advent of laser light. Remarkably, he used simple glass filters and the bright mid-day sun to observe the first Raman optical effect. Today, we have well characterized the vibrational effects of numerous different molecules. Table 1 is a list of some common gasses along with their respective Raman cross sections relative to the nitrogen  $2331\text{cm}^{-1}$  cross section of  $2.3 * 10^{-31}\text{cm}^2/\text{sr}$  when pumped at 532nm. Note that these numbers are all extremely small. Essentially, they represent the ratio of the number of incident photons that will generate a Raman photon upon collision in a sample versus the number that will not generate Raman photons. The cross-section is not a function of density, interaction length, or solid angle. Furthermore, the relative intensity of Stokes radiation is inversely proportional to the fourth-power of the Stokes wavelength. This means that the strongest Raman is produced by the shortest pump wavelength for any molecule. In many cases this too can be a drawback as short (UV to visible) wavelength lasers (ion lasers, frequency doubled lasers) are often more expensive than their mass produced IR telecommunications counterparts (solid state) [1].

Table 1 – Raman cross-sections of common gases [2,29]

Component	Raman shift (cm <sup>-1</sup> )	Relative* Raman scattering cross section $\Sigma$
Methane, CH <sub>4</sub>	2917	8.6
	1535	0.1
Ethane, C <sub>2</sub> H <sub>6</sub>	2914	15.0
	993	1.2
Propane, C <sub>3</sub> H <sub>8</sub>	2908	19.6
	870	1.6
n-Butane, C <sub>4</sub> H <sub>10</sub>	2890	15.6
	827	1.9
iso-Butane, C <sub>4</sub> H <sub>10</sub>	2880	8.4
	794	2.8
Ethylene, C <sub>2</sub> H <sub>4</sub>	3020	6.4
	1623	2.1
	1342	2.8
Carbon dioxide, CO <sub>2</sub>	1388	1.1
	1285	0.8
Nitrogen, N <sub>2</sub>	2331	1.0
Oxygen, O <sub>2</sub>	1555	1.0
Carbon monoxide, CO	2143	0.9
Hydrogen, H <sub>2</sub>	4156	3.9

Despite these complications, we feel that Raman spectroscopy is a powerful tool that can be harnessed to produce a gas sensing system with previously unattainable speed and accuracy. The inherent vibration-based (or rotation based) nature of the effect makes it definitive for gas identification; while its output signal power varies linearly with sample density, making it ideal for concentration analysis. In addition to being a fundamentally suitable principle, we note that the characteristics of detection are also inherently simple. The longest Raman shift is exhibited by the smallest molecule: hydrogen. This molecule's 4156 cm<sup>-1</sup> shift, along with the chosen pump wavelength, dictate the largest possible detection bandwidth for a Raman experiment. With the choice of excitation wavelength being made by the researcher, we can dictate the measurement wavelength range as we see fit. Thus, choices can be made with regard to detector sensitivities, cost of pump lasers, and absorption in a given material or sample cell. The only

basic challenge to be overcome is that Raman in gasses is a very weak phenomena requiring careful measurement techniques or (as we will show) novel sensing geometries [1].

### **1.3 DISSERTATION ORGANIZATION**

In the following dissertation, we intend to detail the research and construction of a Raman gas analysis system capable of being used for rapid natural gas characterization, or the quick examination of any gaseous mixture. In order to clarify the inception and improvements upon the Raman gas sensing system, we will first start with a brief treatise on collecting scattered optical power. This will contain a review of various sensing geometries with respect to gas-Raman. We will also detail two relatively new sensing geometries using internally-reflective capillary tubing and hollow-core photonic crystal fiber as the gas-containing cell and Stokes light collector.

Chapter 3.0 of this dissertation begins the experimental work designed as verification of predictions regarding the use of novel gas sensing geometries. Contained therein is work designed to illustrate the noted superiority of photonic bandgap fiber gas cells as the container of choice for gas Raman experiments. We also detail the advantages of forward-wave versus backward-wave scattering in all-fiber configurations using atmospheric gasses.

Chapter 4.0 includes preliminary results for hydrocarbon and other gas sensing. We analyze specific gas-Raman results and discuss the noise present in current Raman measurements. We also discuss methods for noise mitigation including a successful spatial filtering technique, as well as issues regarding modern optical filter technology.

Chapter 5.0 is a detailed study of gas flow in this particular sensor design. It details experimental predictions and findings related to gas flow and other fluidics issues.

Chapter 6.0 reports results obtained by combining our prototype Raman gas sensor with a gas chromatography system. The Raman system is presented here as an alternative to other GC detectors as opposed to a stand-alone sampling system. Exchange rate properties and micro-volume sampling issues are discussed.

Chapters 7.0 and 8.0 report on the use of a different type of waveguide structure produced by lining the inside surface of a hollow glass capillary tube with a reflective metal coating. This sort of capillary waveguide system will be studied in comparison to the PBF system described in chapters three and four. Chapter 7.0 describes the a theoretical model for the optical collection characteristics of metal-lined hollow waveguides, while Chapter 8.0 accounts Raman experiments carried out with commercially available guides. This work expands the single-mode analysis of PBF into a multimode analysis for the larger diameter capillary waveguides.

Finally, Chapter 9.0 concludes this dissertation with some theoretical and experimental designs for miniaturizing and commercializing the Raman gas sensing system. Methods of miniaturization and system cost reduction are elaborated. Rudimentary experimental results pertaining to system miniaturization and simplification are demonstrated. Ultimately, we conclude with suggestions for further possible system improvements and research.

## **2.0 RAMAN CONFIGURATIONS AND POWERS**

It should be clear that the largest foreseeable challenge in Raman gas sensing, or Raman sensing of any type, is measuring the extremely small number of Raman photons produced by exciting a sample. To illustrate this problem, we will detail the power produced and collected in various configurations. This chapter will include standard geometries like the “tight focusing” free-space technique. Then we will briefly examine the use of reflective capillary tubing for use as the Raman gas cell and Stokes light collector. Finally, the use of a hollow-core photonic bandgap fiber will be reviewed in the same capacity. By examining the characteristics of such waveguides, we can show that HC-PBF and reflective capillaries make useful Raman cells [8].

### **2.1 COLLECTING SCATTERED POWER**

The very nature of utilizing spontaneous Raman scattering involves the collection of a diffuse (scattered) optical signal. In most cases, the pump light used to initiate Raman is provided by a laser beam. Any such beam will (at best) propagate in a diffraction limited fashion, with focusing and expansion properties governed by the wavelength of the propagating beam and the quality of that beam. If the total power in the pump beam is given by  $P_o$ , then the total Stokes Raman power ( $P_s$ ) is given by:

**Equation 2:**  $P_s = KL \cdot 4\pi \cdot P_0$

where  $L$  is the length of interaction between the pump beam and the sample, and  $K = \rho \cdot k_r$ ; where  $\rho$  is the density of the sample and  $k_r$  is the Raman cross section for a particular gas. This equation assumes that the Raman light, which is scattered in all directions, can be totally captured, and that effects due to polarization dependence of scattering can be ignored. A more realistic relation is given by:

**Equation 3:**  $P_s = KL\Omega_0 P_0$

where  $\Omega_0$  is the solid angle which can be collected by the collection optics or detector.

Several important conclusions can be drawn from this simple description of collectable power. First, any comparison of Raman collection techniques is essentially a comparison of the product of  $L \cdot \Omega_0$  (known as *entendue*). Better collection systems will either collect a larger solid angle of Raman radiation, or will increase the interaction length of the pump beam through the sample. The clever optics aficionado will immediately wish to add a system of lenses to collect more light. As we will see in the following sections, imaging lenses designed to magnify the interaction space by  $M$  (magnification  $>1$ ) in some free-space collection configurations will have the effect of reducing  $L$  by  $M$  and increasing  $\Omega_0$  by  $M^2$ . Thus, the total Raman signal is increased by  $M$ . Real detection systems have some finite area; given either by the area of the detector itself, or by a spectrometer's slits, etc. Therefore, the actual size and acceptance angle of the detection equipment will ultimately place a limit on extent of useful magnification optics [36]. The ultimate result of such limitation is that novel new methods must be researched in order to increase the total amount of collectable Raman light for high-sensitivity applications.

## 2.2 GAS RAMAN MEASUREMENTS WITH A SPECTROMETER

Dating back to early Raman experiments, the rudimentary method for measuring Raman signals has been through the use of a dispersive grating spectrometer. In such an instrument, an incoming beam is dispersed by a movable grating whose diffracted output is re-focused onto a detector of some sort. The resolution of the instrument is usually determined by a pair of vertical slits at the input and output of the device. While some spectrometers have been manufactured with horizontal slits, we will hereafter consider only vertical slit orientation to avoid confusion. Slit width, grating dispersion, and focal length determine the spectral resolution of such a device. Slit height is usually limited by the height of the detector, and is usually on the order of 10-1000X slit width. We can see that slit width in Raman measurements limits wavelength resolution, and also the amount of useable magnification in a contrary fashion.

Given a gaseous sample, a grating spectrometer, and a diffraction-limited laser beam; there are only a few conceivable geometrical configurations by which to measure Raman light [6]. We can consider the three most common methods being axial, 90° horizontal, and 90° vertical. Figure 2 illustrates these configurations. In any of these cases, a gaseous sample is contained in a transparent cell, occupying a large volume in front of the spectrometer. In the axial case, the laser is aimed directly through the sample into the spectrometer. For simplicity, we will consider a single collection lens between the sample and the entrance slits. In this scenario, it is best to focus the pump beam such that its focus is as small as possible and centered inside the sample. The interaction length will be approximately given by twice the Rayleigh Range of the pump beam's focus, and the acceptance angle will be determined by the spectrometer's optics or the input lens (whichever has the smaller angular acceptance). In this case, increasing spectral resolution (smaller slits) drastically reduces collected Raman power. In

addition, pump light which is many orders of magnitude stronger than emitted Raman must not be allowed to scatter inside the instrument and reach the detector, obscuring Raman signals. To actually employ this method, researchers typically use either a holographic pump-rejection filter or an expensive double or triple spectrometer system [1].

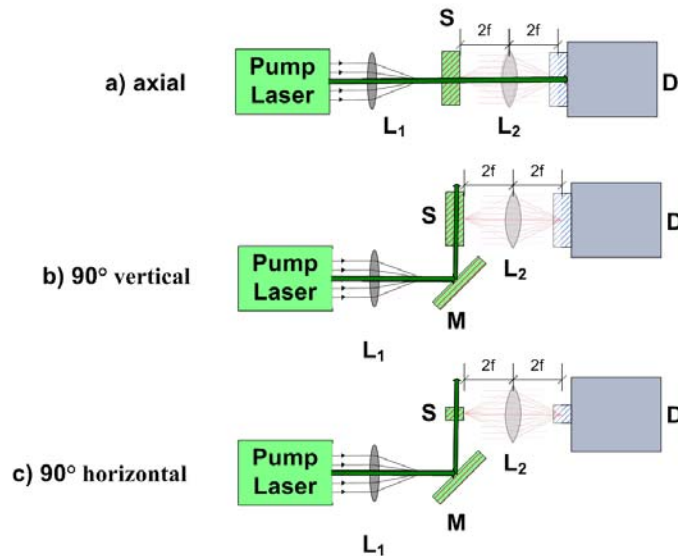


**Figure 2 - Traditional Raman collection configurations**

Among these simple configurations, it is obvious that 90° scattering systems are far more appropriate than axial scattering methods. If the pump beam is directed perpendicular to the entrance slits, the interaction length is determined by the slit width. When the pump beam is directed parallel to the spectrometer's entrance slits, the interaction length can effectively be as long as the height of the slits. Because slit height is considerably larger than slit width, the most efficient method of collecting Raman with these tools is to direct the pump beam parallel to the entrance slits (usually indicating a vertical direction given the orientation of most spectrometer slits), while being focused to a waist directly in the center of the slits. Because we assumed a diffraction limited beam, we may also assume that such a beam may be focused such that its waist is equal to or smaller in diameter to the slit width, and that its depth of field is longer than

the slit height. Such conditions are readily achievable with a visible wavelength laser with a small diameter beam (several millimeters), and a focusing lens with a reasonable focal length (~1m focal length is required in the visible for a ~100um diameter beam waist). Again, a single collection lens is used to image the beam waist onto the entrance-slit plane. Providing 1:1 imaging preserves the maximum collected solid angle, and allows the spectrometer slits to be set at the width of the beam waist for optimal resolution.

We can effectively re-write Equation 3 to include the inherent features of the grating spectrometer in accounting collected Raman power. Spectrometers have an acceptance angle

usually given as an  $f\#$ , where  $\Omega_s = \pi[\frac{1}{2 \cdot f\#}]^2$ . Therefore, collected Stokes power is:

$$\text{Equation 4: } P_s = KH\pi \cdot [\frac{1}{2 \cdot f\#}]^2 \cdot P_0$$

where the specific interaction length for this case (H=L) is the height of the spectrometer slits, and  $f\#$  is the spectrometer acceptance f-number,  $P_0$  is the input pump power,  $K$  is the gas's Raman cross section times the gas density (as defined previously), and magnification (M) is unity. It should be noted that spectrometer entrance slits are usually less than 1cm high, and common acceptance angles are usually between .01str and .2str (f/9 to f/2). If we consider an f/6 spectrometer and a 100mW 514.5nm argon-ion pump beam with perfect spectrometer collection efficiency, the maximum Stokes Raman power we can collect in 1-atm nitrogen gas is given by

$$\begin{aligned} \text{Equation 4: } P_s &= KH\pi \cdot [\frac{1}{2 \cdot f\#}]^2 \cdot P_0 = \\ &= 2.6 * 10^{-31}(\text{cm}^2/\text{molecule*sr}) * 6.022*10^{20}(\text{molecules/cm}^3) * 1\text{cm} * \pi * [1/(2*6)]^2 * 100\text{mW} \\ &= 3.4*10^{-13} \text{ Watts.} \end{aligned}$$

These physical properties make collecting a significant amount of Stokes light very difficult in this configuration. That is why numerous researchers have sought to improve upon collection geometries [9-14].

### 2.3 RAMAN COLLECTION IN A WAVEGUIDE

A major innovation in Raman collection techniques was the utilization of a length of metal or dielectric internally-reflective tubing as the gas cell and Raman collector [9-17, 40]. Placing the Raman gas-sample inside a length of tubing which also serves as a light collector seems to be an obvious improvement, but in fact, there are pros and cons to such a configuration. In order to characterize the optical properties of such a length of tubing, we should first consider how light propagates inside a length of any type of hollow structure. In a capillary (tube) waveguide, light might be guided by the mechanism of total internal reflection (TIR). That is the property by which rays propagating at angles within the critical angle for a given optical index-difference are reflected, thus propagating down the tube in a series of “bounces”. For a dielectric capillary tube whose wall has an index of refraction  $n_2$ , and whose core has an index of refraction  $n_1$ , the critical angle is given by:

$$\text{Equation 5: } \theta_c = \sin^{-1}\left(\frac{n_2}{n_1}\right)$$

Foremost, the index of refraction of the sample in the core must be greater than the index of refraction of the walls in order for TIR to occur in a dielectric guide. Most gases have an index of refraction close to 1.0, which makes them incompatible with uncoated glass-capillary TIR systems [30].

Extensive work has been done using standard glass capillaries and *liquids* with higher indices than the capillary walls. Gas Raman experiments have also been conducted which relied on grazing incidence to propagate a high-loss EH<sub>11</sub> mode in an uncoated tube [18-22]. This method has been reported to offer gains 30-50 times greater than free space configurations, and is presumably limited by the high-loss propagation [17]. It is also impossible to collect a large solid-angular output in this fashion, due to the high loss associated with higher-order modes.

In the absence of materials with indices of refraction less than 1.0 at optical wavelengths, researchers have also explored capillaries with internal metallic reflective coatings to serve as Raman cells. Results have been promising enough to encourage our own experimentation with reflective capillaries, which will be covered in Chapters 7 and 8. In general, it is difficult for reflective capillary systems to be produced with low-loss, due to difficulties in placing reflective coatings inside the tubing. Promising schemes which would utilize hollow Bragg fiber (basically a capillary with layered internal coatings providing an optical bandgap or distributed-reflector over a range of wavelengths) have also been daunted by the difficulties associated with producing even coatings.

Despite these difficulties, we can still attempt to optimize a capillary tube for Raman collection. First, it is necessary to determine the diameter of such a tube for use as a gas cell. In general, the numerical aperture required to capture a diffraction-limited (Gaussian) expanding beam is given by:

$$\text{Equation 6: } NA = n \cdot \sin(\theta) = \frac{2\lambda}{\pi D}$$

where  $n$  is the index of refraction,  $\lambda$  is the wavelength of light, and  $D$  is the beam waist diameter at the  $1/e^2$  point. Note that the beam waist diameter falls in the denominator of this equation. This provides a clue as to the angular relationships that may exist in various collection

waveguides. Regardless of whether or not the waveguide is small enough to ensure single mode propagation at a particular wavelength, we can be sure that a smaller tube will propagate fewer modes, and therefore a smaller angular output [30]. Thus, we should choose the capillary diameter such that our detection equipment collects a full acceptance-cone without any magnification. Also, the tube diameter has severe impacts on the flow of sample gases. Therefore, it may be more important to ensure that sample gas flows at an appropriate rate rather than have a perfectly illuminated detection system. Because such waveguide systems will generally be multimode in nature and will exhibit far different properties than their single-mode (PBF) counterparts, we will save the majority of the analysis of reflective capillary waveguides for Chapter 7.

## 2.4 WAVEGUIDE LOSS AND DIRECTION

We noted previously that a great deal of propagation loss can be present in currently available waveguides. This factor will be the primary determinant of the useful length of a Raman cell. The loss at a particular wavelength in a waveguide ( $\alpha$  – Napiers/m) is determined by a number of different factors. For now, we will consider that this loss is not a function of length or angle (which we will later prove to be not strictly true). In the case of PBF, the loss is a function of the core and cladding geometry, as well as the presence of fiber-drawing defects and imperfections. In a reflective capillary, the loss is primarily caused by the internal metal coating's reflectivity and surface roughness of the internal coating. In either case, pump light enters the waveguide at one end with a power  $P_0$ . Loss at the pump wavelength is given as  $\alpha_p$ . At any point (x) along the length (L) of the waveguide, the pump power is:

**Equation 7:**  $dP(x) = P_0 e^{-\alpha_p x}$

The Raman power generated at that point will be:

**Equation 8:**  $dP_R(x) = \sigma P_0 e^{-\alpha_p x}$

where  $\sigma$  is the product of the Raman cross section of the molecular species in question and the density of that species. In the forward-scattering case, with loss at the Raman wavelength given by  $\alpha_R$ , the Stokes signal generated at  $x$  will emerge from the other end of the tube with power:

**Equation 9:**  $dP_{R0}(x) = \sigma P_0 e^{-\alpha_p x} e^{-\alpha_R(L-x)}$

This is because the differentially-generated Stokes signal must travel a distance of  $(L - x)$  to arrive at the tube output. We must then integrate over the length of the tube to find the total forward Stokes output power:

**Equation 10:**  $P_{Rfwd} = \int_0^L \sigma P_0 e^{-\alpha_p x} e^{-\alpha_R(L-x)} dx$

Integrating and simplifying the above expression yields:

**Equation 11:**  $P_{Rfwd} = \sigma P_0 e^{-\alpha_R L} \cdot \frac{1}{\alpha_R - \alpha_p} \cdot [e^{(\alpha_R - \alpha_p)L} - 1]$

In the case where the loss at the pump and Stokes wavelengths are the same, this expression simplifies to:

**Equation 12:**  $P_R = \sigma P_0 L e^{-\alpha L}$

The backward-generated Stokes collection is slightly less complicated. In this case, the same derivation may be followed, except the differentially-generated Stokes light must travel over a length of  $(x)$ , instead of  $(L - x)$  to reach the collection end of the tube. Total collected Raman output power is given by:

**Equation 13:**  $P_R = \sigma P_0 \cdot \frac{1}{\alpha_R + \alpha_p} \cdot [e^{-(\alpha_R + \alpha_p)L} - 1]$

In a similar simplification, the same loss at pump and Stokes wavelengths leads to a combined loss of:

$$\text{Equation 14: } P_R = \sigma P_0 \cdot \frac{-1}{2\alpha} \cdot [e^{-2\alpha L} - 1]$$

Several important conclusions should be drawn from this power collection analysis. Firstly, we note that the backward collection efficiency in a capillary with finite loss is more efficient than forward collection. That is because the pump light is strongest at the input end as it enters the waveguide. The strongest Raman signals are generated in the end closest to the pump-light entrance. The strength of the differentially-generated Raman signal decreases as we move towards the back-end of the waveguide because of the transmission loss. The Raman light that is produced near the front (pump-input) end of the waveguide traveling in the backward-wave direction experiences no loss, as it exits the guide directly. The Stokes light emitted near the back-end (pump output) of the tube must undergo loss over the entire length as it travels back through the tube for collection. In the forward-scattering direction, the largest Stokes signal must undergo the most loss as it travels the length of the tube before exiting. The smaller portion of the Stokes signal generated near the back-end of the tube undergoes the least loss as it exits the tube directly. If we take the ratio of Equation 12 / Equation 14 we arrive at:

$$\text{Equation 15: } \frac{P_{R\_forward}}{P_{R\_backward}} = \frac{\sinh(\alpha L)}{\alpha L}$$

This ratio implies the factor of improvement realized when using backward scattering collection instead of forward scattering collection [47]. Because of this advantage, collection systems that utilize the backward wave configuration should produce larger signals than those with forward collection. In addition, a number of mechanical differences will be noted which will often play a

large role in the choice of one coupling system over another. These differences will primarily be discussed in Chapter 4.

## **2.5 PRINCIPLES OF PHOTONIC BANDGAP FIBER**

Since the advent of single-mode optical fiber more than 50 years ago, the light-containing core of the fiber has always been a solid material. This, as we alluded to previously, is because the index of refraction in the core must be higher than that of the cladding in order to achieve the necessary total-internal-reflection conditions for propagation. For years a number of fiber-optic sensors were developed with varying types of “evanescent wave” detection schemes. These sensors measure the small portion of light leaking into the fiber cladding (characterized by the loss in the fiber) which interacts with the surrounding medium, thus allowing various substances to produce repeatable optical effects. This is, of course, an extremely limited technique for several reasons. Firstly, the sample is not caused to interact with the propagating pump beam very efficiently. Secondly, if scattering is the aim of the sensor, there is no means to collect scattered evanescent light outside the fiber core. These problems are all overcome through the use of a unique and different type of optical fiber [8,15,16,23-28].

Hollow core photonic bandgap fiber (HC-PBF or simply PBF) represents a new paradigm in optical confinement technologies. It is, in essence, a small capillary tube surrounded by a glass honeycomb of smaller capillary tubes; all of which are filled with air. Figure 3 is an SEM cross-sectional image of a piece of photonic bandgap fiber. The walls and surrounding supporting structure of the PBF are made of solid un-doped amorphous silica glass, which is additionally clad in a protective plastic jacket. In PBF, light is actually guided in the hollow air-

filled core, with only a small portion of light evanescing into the cladding layers. From its advent, researchers have known that such a structure would be a useful tool for sensing due to the prospect of interaction of a small-volume laser beam with substances injected into the fiber core. Hereafter, we demonstrate such utility.

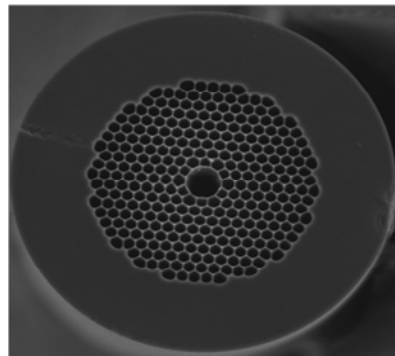


**Figure 3 Cross section of an HC-PBF [41]**

The concept of photonic bandgap guidance is one which may be outlined carefully in mathematical terms using Maxwell's equations for field propagation, along with the proper boundary conditions imposed by the fiber cladding structure [45]. Because these derivations are well known, and represent the basis for a number of photonic crystal simulation software tools, we will simply invoke a basic understanding here. The concept of the Bragg grating has indeed been widely understood for decades. Figure 4 is used to represent the analogy between a 2D Bragg grating and a 3D photonic crystal.

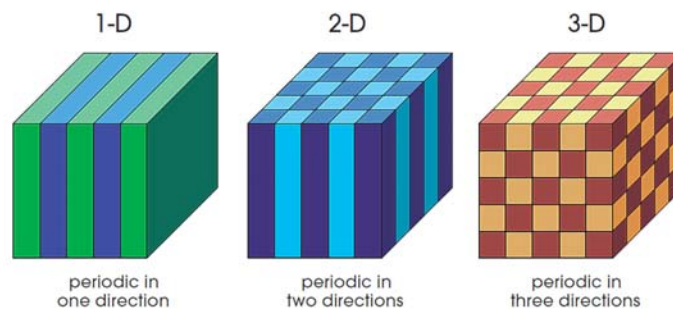


**Figure 4 - Periodicity schematic: 1D Bragg Grating, 2D Periodic Structure, and 3D Photonic Crystal**

[45]

A one-dimensional Bragg grating is simply a stack of alternating layers of two different materials with different indices of refraction. Any light striking the surface of the 1D Bragg grating will partially reflect and partially transmit into the stack. The subsequent transmitted portion striking the second layer of the stack will, in turn, also be partially transmitted and partially reflected. When light of the correct wavelength (given by Equation 16) strikes the Bragg grating, all of the reflections from layers of thickness  $d$  in the stack are in phase, and add coherently to produce a strong reflection at that wavelength. Another way of thinking about this action is to declare that the stack has a 1-dimensional bandgap that does not allow propagation of light of a particular wavelength through the grating [30].

**Equation 16:**  $2d \sin(\theta) = n\lambda$

We can generalize the 1D Bragg grating into a 2D structure by wrapping the dielectric Bragg stack about a central axis. The bandgap now encircles points in the center of the newly formed tube. In practice, it is difficult to produce evenly-alternating layers of two different materials on the inside of a small capillary tube. For that reason, the accepted method is to employ a number of large capillary tubes which are drawn together using standard optical-fiber drawing techniques to produce a PBF structure (see Figure 5). The resulting product is made entirely of a web of amorphous fused silica. The alternation of air holes and silica walls act similarly to alternating layers in a Bragg stack. Because there is a large difference in the indices of refraction for air and silica (1.0 and  $\sim 1.5$  respectively), the existence of connecting silica struts between subsequent layers of glass does not eliminate the possibility of creating a bandgap in the fiber [48].

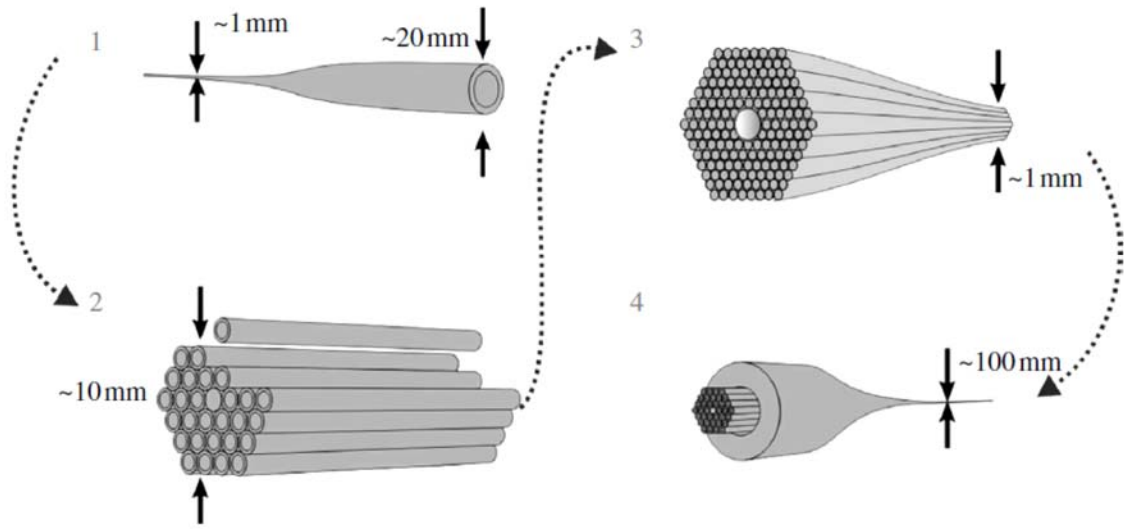


**Figure 5 - PBF drawing procedure [48]**

Quite a few advances have been made in the field of HCPBF fabrication. The currently accepted fabrication technique involves stacking a number of small glass capillaries and removing several from the center of the stack to create a void for the core. Then, drawing is performed as it would be with regular solid fiber, although care is taken not to collapse the core and cladding holes during the drawing process. We note that the core diameter is usually on the order of the diffraction limited spot size, while the cladding holes are of much smaller diameters (perhaps 5 to 20 times smaller). Loss in such fibers has been shown to be very low (as little as 1.7dB/km – [7]), with tradeoffs existing between the width (nm) of the bandgap and the loss in the core. Benabid clarifies the tradeoffs between core size and loss by assigning a figure of merit to particular PBFs [48] in a stimulated Raman experiment. We later develop our own figure of merit for the spontaneous Raman case. The figure of merit derived by Benabid is given by:

$$\text{Equation 17: } F_{om} = \lambda \frac{L_{eff}}{A_{eff}}$$

where  $\lambda$  is the wavelength of guided light,  $L_{eff}$  is the effective constant intensity interaction

length of the PBF (limited by its losses) and  $A_{eff}$  is the effective cross-sectional mode area.

Figure 6 shows how PBFs with various loss values compare.

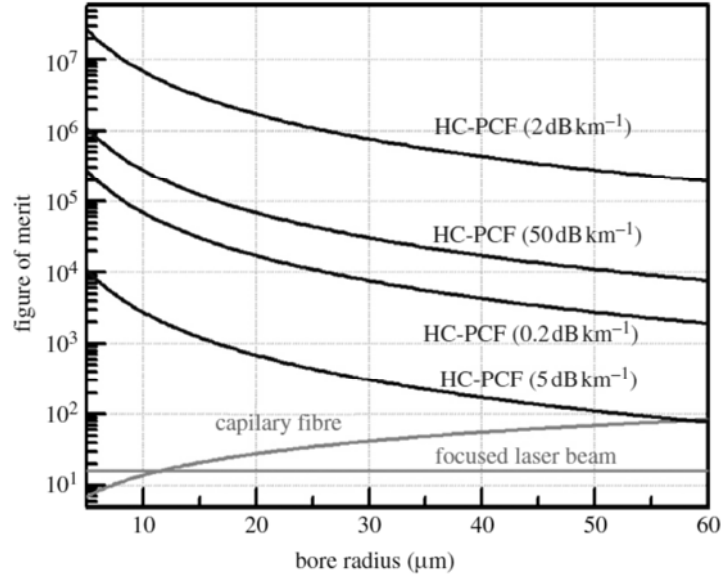
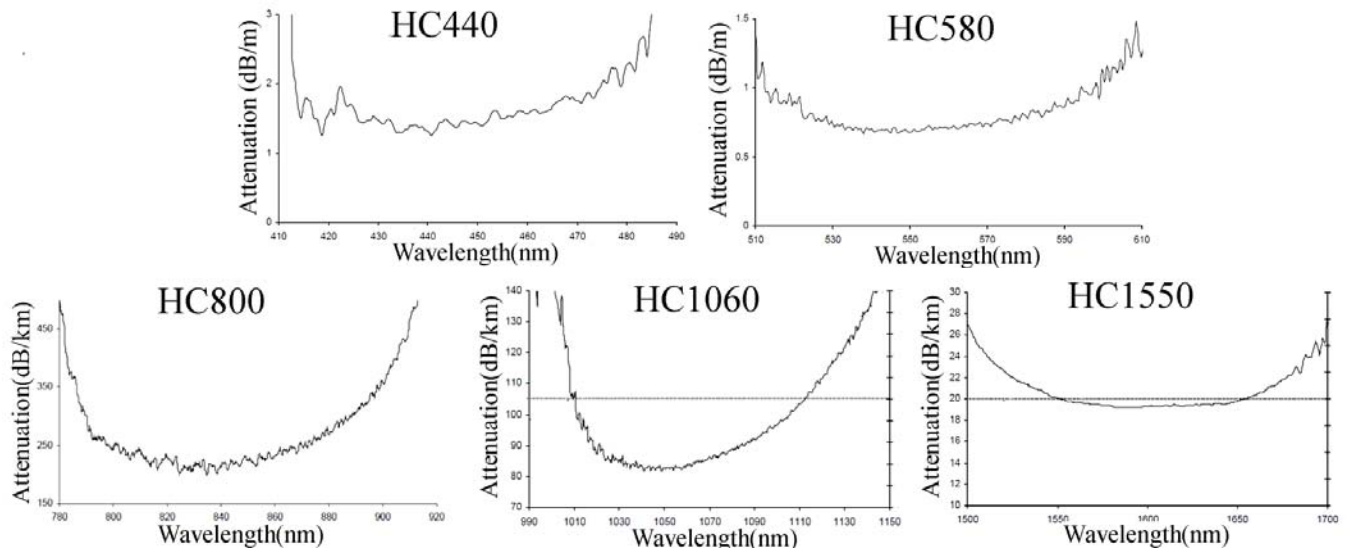


Figure 6 – Figures of merit for PBF [48]

Given the huge merits in the unnatural confinement of a laser beam to a near diffraction-limited spot size over a very long length, it is believed that an extremely effective Raman scattering sensor system can be produced to exploit this advantage. Previously, a number of researchers have successfully implemented PBF for absorption spectroscopy and stimulated emission sources [23-28]. Currently, a number of different HC-PBFs exist commercially. Most of these are manufactured in small quantities by Crystal Fibre and Corning Glass for experimental purposes. Figure 7 is a plot of transmission loss in several available commercial PBFs. Each fiber operates in a slightly different wavelength range, usually with less than 1dB/m loss over a wide range of transmission band. These fibers were chosen for analysis due to their availability and visible or near-IR transmission bands. They represent the best possible commercial choices for gas-Raman sensing applications. We intend to detail the use,

implementation, and resultant sensing characteristics of several of these fibers in the production of a useful Raman gas sensor.



**Figure 7 – Commercial HC-PBF transmission bands [41,42]**

## 2.6 RAMAN COLLECTION IN A PBF

We propose a novel system in which a gaseous analyte of unknown composition is injected into a length of PBF under pressure. A pump laser beam is focused into the fiber core along with the sample gas. Inside the fiber core, pump/gas interaction will result in Rayleigh scattering losses, and a small portion of Raman scattering. The fiber will guide scattered Raman photons generated in the fiber core whose propagation angles fall within the numerical aperture of the fiber. At either end, spontaneous Stokes scattering inside the bandgap wavelength range will emerge as a single Gaussian mode. This light will then be collected and analyzed to determine the composition of the gasses in the core. In this section, we will make a comparison between this proposed technique and a traditional 90-degree scattering technique for gas-Raman

collection. We also estimate the magnitude of Stokes power collected in a number of available PBFs [41,42, etc.].

If we re-examine the fibers suggested in section 2.4, we note that if we accept losses in the  $\sim 1\text{dB/m}$  range, transmission bandwidth can be as large as  $\sim 100\text{nm}$ . One of our goals is to be able to view vibrational Raman peaks from every imaginable gas mixture using a single length of fiber. As was observed, the first vibrational peak produced by pure hydrogen gas exhibits the largest known gas-Raman Stokes shift, due to the low mass of the hydrogen molecule. This number represents the maximum necessary bandwidth of a PBF for gas Raman sensing. If we wish to observe Stokes shifts, naturally the pump wavelength should be placed closest to the left-hand (short wavelength) side of the fiber's transmission band. There is, of course, the need to ensure high transmission of both the pump and Stokes wavelengths in order to ensure the largest Raman signals.

To gain a visceral understanding of the magnitude of improvements on Raman scattering collection enabled by PBF, we must first enumerate the Stokes power collected in a free-space 90-degree scattering configuration using a grating spectrometer. As we noted earlier, collected Stokes power is primarily a function of collected solid angle and interaction length as per Equation 3. Let us assume we are working with a grating spectrometer with an entrance aperture of  $f/6$ , and a slit height of  $1\text{cm}$ . Raman scattering is to be collected from a vertical  $514.5\text{nm}$  argon-ion laser beam brought to a focus in front of and parallel to the entrance slits of the  $f/6$  spectrometer; i.e. in the standard 90-degree scattering configuration discussed previously. In order to properly collect the Stokes radiation, it is most effective to image the Stokes source onto the spectrometer entrance slits. This requires choosing a lens that will fill the angular entrance aperture of the spectrometer completely; i.e., a lens with the ratio of focal length/clear aperture

(diameter) ratio  $< 6$ . The clear aperture of the lens must be larger than the confocal parameter (twice the Rayleigh range) of the pump beam focus in order to image the entire pump-focus and collect all possible Stokes scattering generated in the higher power-density region. This lens is placed a distance of  $2*f$  away from both the entrance slits and the pump-beam focus to satisfy image-formation conditions. Since our aperture (slit) is 1cm high, the required beam waist will be implied by the confocal parameter (b):

$$\text{Equation 18: } b = \frac{\pi\omega_0^2}{\lambda} > 1cm$$

$$\text{or } \omega_0 = \sqrt{\frac{b\lambda}{\pi}} > 40\mu m$$

In order to achieve a  $40\mu m$  beam waist diameter, we must also choose the correct lens to focus the pump beam to a waist in front of the slits. For this we refer to Equation 19, which assumes a diffraction limited Gaussian beam. Therein,  $d$  is the beam waist diameter ( $1/e^2$ ),  $f$  is the focal length of the pump focusing lens, and  $D$  is the diameter of the collimated pump beam ( $1/e^2$ ) incident on the lens:

$$\text{Equation 19: } d = \frac{4\lambda f}{\pi D}$$

$$\text{or } f = \frac{dD\pi}{4\lambda}$$

Given a 3mm diameter input beam, we must select a pump-focusing lens with a focal length of at least 18cm. Under these conditions, the spectrometer entrance slits may be closed to no less than  $40\mu m$  under perfect imaging conditions. In a more realistic scenario, given alignment errors and lens aberration, the slits should realistically be set to no less than twice that value. Overall, our selection of lenses implies a maximum collectable Stokes signal. The length/angle product (or figure of merit, or entendue) for this case is about:

**Equation 20:**  $E_{spec} = \Omega_{spec} \cdot L_{spec}$

or  $E_{spec} = \left[\frac{1}{2 \cdot f\#}\right]^2 H \approx 7 \cdot 10^{-5}$

Similar arguments can be made for our proposed PBF collection system. The figure of merit for Raman collection is similarly based on entendue. We must first determine the angular acceptance of the fiber in order to compare it to that of our theoretical measurement spectrometer. Often, fiber manufacturers will simply provide a numerical aperture (NA) value for a particular fiber. This is usually the most accurate value to be used in determining collection efficiency. If that data is not available, we can calculate the angular acceptance angle of the single-mode fiber as being the same as the far-field diffraction angle of a Gaussian beam [30]:

**Equation 21:**  $\theta = \lambda / (\pi \omega_0)$  or  $\Omega \approx \pi \theta^2 = \pi \lambda^2 / (\pi \omega_0)^2 = \lambda^2 / A$

where  $\theta$  is the diffraction angle and  $\omega_0$  is the mode-field radius ( $1/e^2$ ). This technique is valid because a standard single-mode fiber will propagate a single Gaussian core-mode. A PBF will propagate a similar core-mode. If we numerically consider the second fiber illustrated in Figure 7 (HC-580), we note a mode area of  $\sim 2.6 \cdot 10^{-11} \text{ m}^2$ , yielding an angular acceptance of  $\sim .010 \text{ str}$ . This is the same as  $f\#/5$ . We thus realize that the angular acceptance of most available single-mode fibers is similar in magnitude to popular single-spectrometers with  $\sim < 1 \text{ m}$  focal lengths.

The real genesis in collection efficiency becomes apparent when we consider the full length-angle product in a length of PBF. We noted that acceptance angles are similar for conventional spectrometer-based collection systems operating in free space and HC-PBFs. In the spectrometer case, the interaction length is limited by slit height or confocal beam parameter; whichever is the lesser. In the PBF case, the interaction length is determined by the useable length of the fiber itself! Of course, limitations are placed on the length of the fiber by transmission losses. In the forward-scattering technique, a clear maximum in the output

power/fiber length curve is defined because increases in length generate more Stokes radiation, which is limited by increased transmission losses. In the backscattering case, an infinitely long fiber is possible, but further length additions will result in continuously decreasing power returns. Thus, it may be useful to employ a length which is tailored such that the pump beam strength has exhausted some large portion of its input energy before exiting the fiber. In either case, the use of fibers with low losses (<1dB/m) implies long possible interaction lengths. If available losses were in fact exactly 1dB/m in the backscattering configuration, a fiber of more than 8-meters in length could be employed with a pump beam emerging at  $1/e^2$  times its input intensity. That implies a figure of merit for the fiber configuration of:

$$\text{Equation 22: } F_{PBF} = \Omega_{PBF} \cdot L_{PBF} \approx .08$$

This figure of merit is approximately 1100 times larger than our figure of merit for a common spectrometer configuration. In fact, fibers with even lower losses may increase possible figures of merit by several times. As we will show later (see Chapter 5), the ultimately useable length of PBF in a gas cell experiment is often governed by the *time* required to inject a gaseous sample into the core, rather than by the losses in the fiber. Even so, useable lengths of greater than 1-meter are often reasonable; which still implies a 2-order of magnitude increase over free-space configurations. It will be the goal of Chapter 3.0 to report enhancements actually measured in free-space and PBF collection configurations. Therein, we have observed PBF figures-of-merit close to those suggested by theory.

### 3.0 ATMOSPHERIC RAMAN EXPERIMENTS

Since purporting large expected gains in Raman signal strengths using HC-PBF, we were eager to verify expectations and quantitatively prove advantages in signal collection using our proposed system. This meant performing Raman collection experiments both in free space and in lengths of HC-PBF. Then, collected power could be analyzed to verify expected signal gains. Thus, a standardized collection experiment was designed and operated with parameters allowing simple comparisons to be made. First, scattering was performed in free space using 90° scattering and 1:1 imaging collection of Raman signals from the gasses in ambient air. Then, a forward-scattering collection was performed in HC-PBF also containing ambient air only. Finally, a backscattering experiment was performed using the same length of HC-PBF containing ambient air. Results from these tests were compared to verify signal enhancements.

Parametrically, all three of these experiments were constrained to be as similar as possible. In order to facilitate effective free-space collection, it was necessary to work in a relatively short (visible) wavelength range to allow detection of atmospheric pressure gasses using available detectors. Again, this is due to the  $1/\lambda^4$  scaling of collected power with Raman wavelength. For these reasons, a Spectra Physics 2016 sub-watt argon-ion laser at 514.5nm was chosen as the experimental pump source. This wavelength also falls near the left-hand edge of the commercially-available HC-580 fiber bandgap; allowing the low-loss transmission of atmospheric gas-Raman signals of interest. The same grating spectrometer and PMT detector

were used for all three collection experiments. In each case, optics were chosen to maximize collected power, and produce the same spectral resolution. Where appropriate, the same set of holographic pump-rejection filters was used in all experiments, ensuring identical attenuation. Therefore, the collected power in each configuration was easily comparable so that figures-of-merit for each situation could be inferred.

### 3.1 FREE SPACE ATMOSPHERIC COLLECTION

Figure 8 displays the experimental setup for free-space Raman collection:

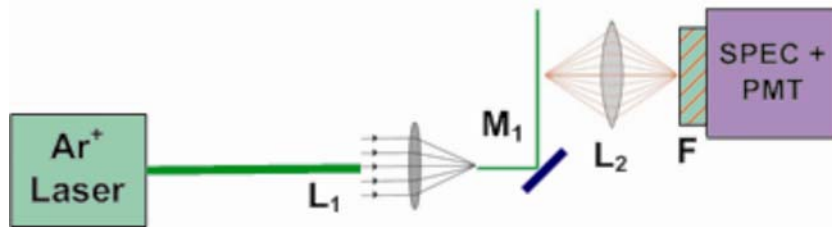


**Figure 8 – Free space Raman collection system. The pump beam is positioned  $2*f$  from  $L_2$  and  $L_2$  is positioned  $2f$  from the spectrometer entrance slits, where  $f$  is the focal length of  $L_2$ .**

The  $\sim 100\text{mW}$ ,  $1.4\text{mm}$  diameter,  $514.5\text{nm}$  pump beam was first directed through a  $\frac{1}{2}\text{-m}$  focal length singlet to produce a  $\sim 150\mu\text{m}$  diameter beam waist at the lens's focus. The converging beam then struck a  $45^\circ$  front surface silver mirror to be directed vertically in front of the slits of a measurement spectrometer. The pump beam propagated  $16\text{-cm}$  away from the entrance slit. A  $2.54\text{-cm}$  diameter,  $4\text{ cm}$  effective focal length (efl) lens provided  $M=1$  (unity magnification) imaging of the Stokes radiation onto the slit. (i.e., the distance between  $L_2$  and the pump beam is  $2f$ , and the distance between  $L_2$  and the spectrometer entrance slits is  $2f$ , where  $f = 4\text{cm}$ ) Directly in front of the slit, a Semrock long-pass edge filter was used to limit the amount of scattered pump light entering the spectrometer. Although the pump scattering in this

configuration is minimal, the pump-rejection filter was used to maintain similar optical paths in all experimental configurations. It is also noted that this holographic filter operates most effectively at small propagation angles, and is thus not used optimally when placed in the converging Raman-beam path in front of the spectrometer. The 180° transmission spectrum (in which light rays pass straight through the filter at 180° in a collimated beam) of this filter is shown in Figure 9:

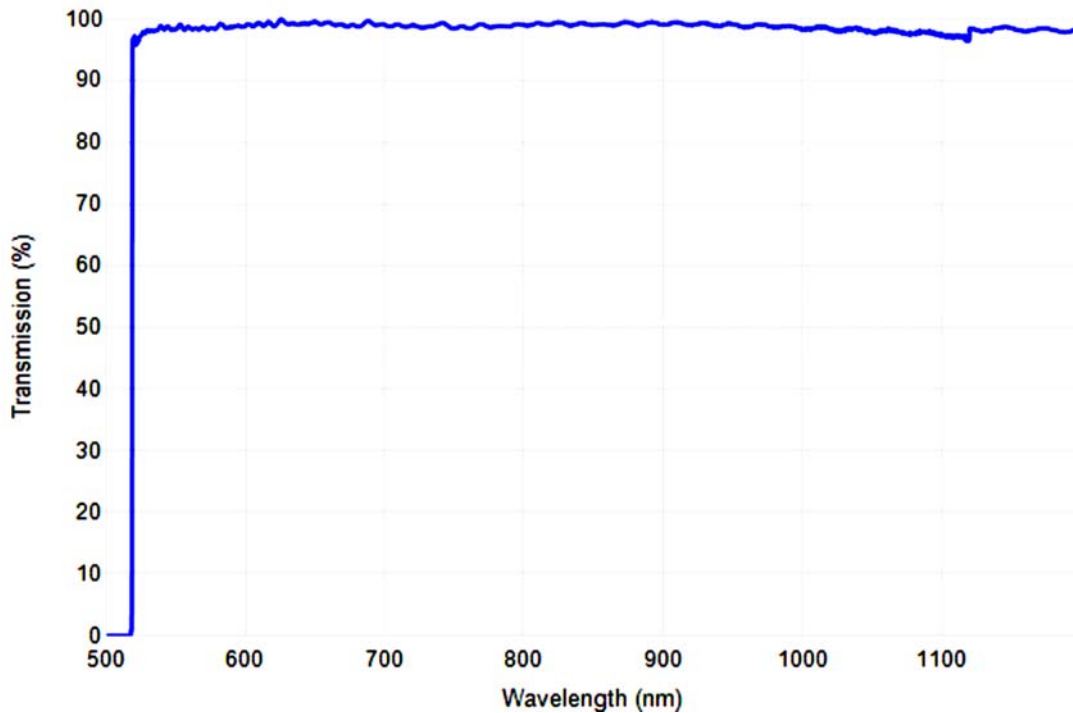


**Figure 9 – Holographic edge filter transmission spectrum [49]**

The spectral measurement system in these experiments consisted of a Horiba-Jobin-Yvon 55cm path length Czerny-Turner movable grating spectrometer with an EMI 9789 photomultiplier tube with high quantum efficiency in the visible range. A diagram of the optical path inside the spectrometer is shown in Figure 10:

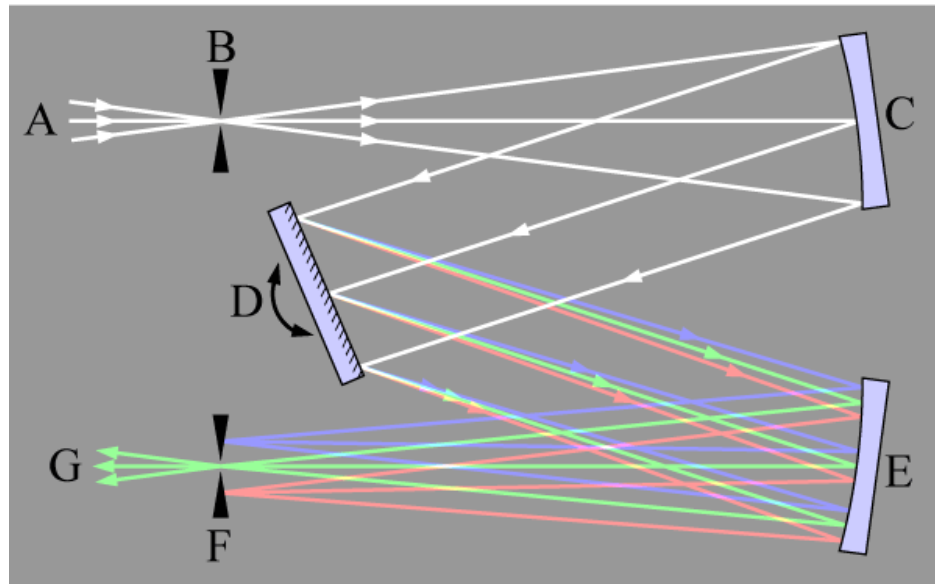


**Figure 10 – Czerny-Turner spectrometer internal light path [50], A: Input, B: Entrance slits, C: Collimating Mirror, D: Dispersion grating, E: Focusing mirror, F: Detector plane or slits, G: Output**

The spectrometer exhibited a dispersion of 1.37nm/mm, and entrance and exit slits were set to 0.5mm wide to allow for easy alignment of the free-space beam. This ensured a resolution of 0.685nm. Slits were 1cm high (maximum) to provide a maximum interaction length. For reference, the atmosphere in which Raman sensing was performed consisted of room-temperature air with a standard composition of ~78% nitrogen, ~21% oxygen, and ~1% other gasses.

A spectrum of the collected Raman light was measured on the EMI PMT and recorded using a pulse discriminator for photon counting with a frequency-to-voltage converter output of 100,000counts/V/second being sampled and recorded digitally. This spectrum is shown in Figure 11:

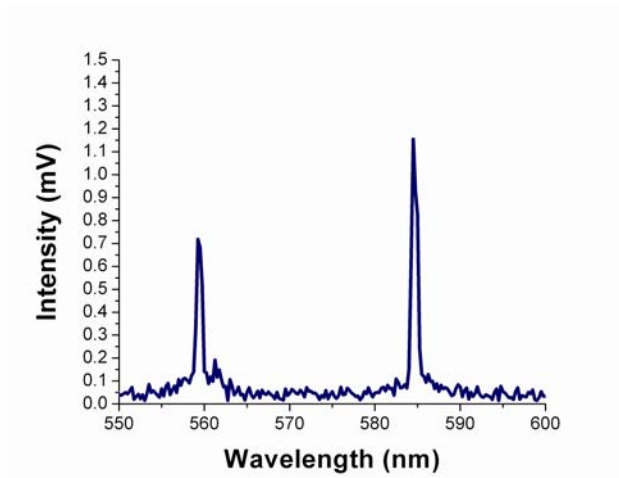


**Figure 11 – Free space Raman spectrum**

In the above spectrum, several important characteristics should be discussed. Firstly, there are two clear peaks from the vibrations of Nitrogen and Oxygen ( $2331\text{cm}^{-1}$  and  $1556\text{cm}^{-1}$ ) at  $584.6\text{nm}$  and  $559.3\text{nm}$  respectively. The magnitude of the detected Nitrogen Raman signal in the figure is about  $1.2\text{mV}$ . The background noise in the figure is mostly phototube dark current and pump-scattering. The following relation can be used to convert voltage readings into the actual power that could be collected based on the energy of a single photon:

$$\text{Equation 23: } P_s = VR \cdot \frac{1}{Q_1 Q_2} \cdot \frac{hc}{\lambda_s}$$

where  $V$  is the measured signal voltage above background,  $R$  is the output voltage ratio ( $100,000\text{counts/V/second}$ ),  $Q_1$  and  $Q_2$  are the quantum efficiencies of the detector and spectrometer,  $h$  is Planck's constant,  $c$  is the speed of light, and  $\lambda_s$  is the Stokes wavelength. Applying numerical values to our free space measurement indicates that the actual collectable power produced in free space at the Nitrogen resonance is on the order of  $4 \cdot 10^{-15}\text{W}$ . This calculation effectively divides out the effects of detector quantum efficiency and spectrometer mirror efficiency such that different wavelength Stokes signals can be compared regardless of detection efficiency at that wavelength. The actual number of counts recorded by the detector is

~1% of the total power entering the spectrometer because of a ~44% mirror efficiency and a ~2% detector quantum efficiency. Regardless of small errors, these values provide a straight-forward comparison to other Raman configurations.

Several other important features should be noted in the free-space Raman spectrum. Firstly, the ratio of the Nitrogen peak to the Oxygen peak does not exactly correspond to the relative cross sections of Nitrogen and Oxygen. This is primarily because of chromatic aberration in the imaging and focusing lenses causing imperfect focusing and some signal loss at the Oxygen wavelength. Alignment was performed using the Nitrogen wavelength as a reference. Second, there is also variation in the detection quantum efficiency over wavelength. If these two factors are eliminated, measured gas cross sections agree well with previous measurements in the literature. Finally, measured linewidths were shown to be instrument-limited, as gas Raman lines are rarely much wider than the pump-line. In this case, the chosen argon pump line was <10 GHz wide.

### **3.2 FORWARD SCATTERING IN HC-PBF**

It was next necessary to perform forward-scattering Raman intensity measurements using a setup similar to the rudimentary free-space configuration in order to confirm predicted enhancements. Figure 12 shows the experimental setup utilized. Therein, the same pump laser (514.5nm) was directed into a 10cm EFL aspheric singlet to be focused directly into a 1.5m length of HC-580 PBF. Coupling efficiency into the 4.2um core of the HC-580 was about 60%. The other end of the fiber was butt-coupled to a length of multi-mode solid-core fiber using a silicon v-groove and UV-curing epoxy.

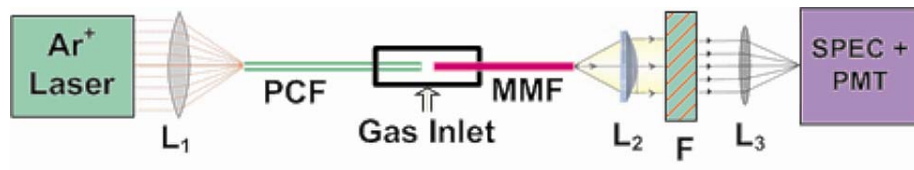


Figure 12 – Forward scattering experimental setup

A schematic of the butt-coupling described is shown in Figure 13. This technique essentially enables the use of this forward scattering configuration for gas-sensing purposes. Intuitively, we realize that several things must be accomplished in order to turn a length of PCF into a gas-sensor. Firstly, pump light must be effectively coupled into the fiber. Secondly, Raman light must also be efficiently collected from the fiber. Finally, there must be a method in which to introduce gasses into the fiber. Unfortunately, those are three things that would be best accomplished independently, despite the fact that a given length of fiber only has two ends at which we may perform some combination of the three coupling tasks.

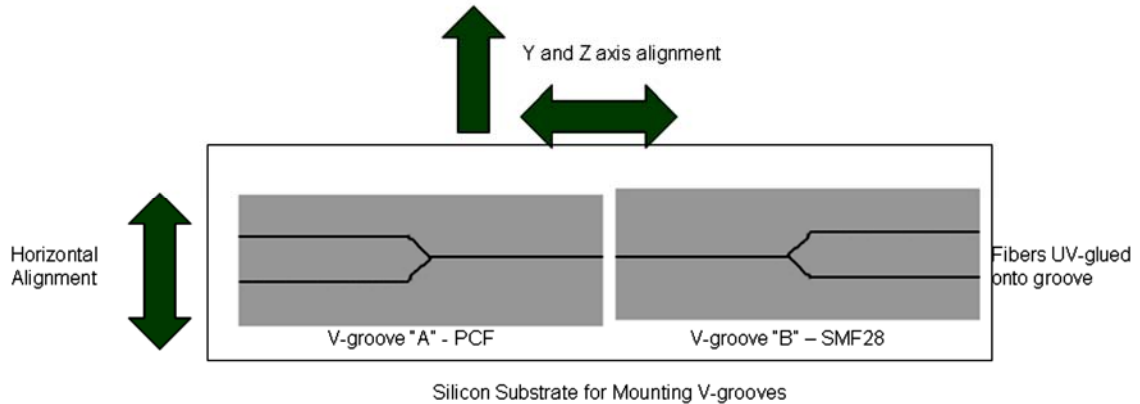


Figure 13 – Fiber-to-fiber butt-coupling schematic

In the forward scattering configuration, we determined that a butt-coupling is the most effective way to retrieve Raman light and simultaneously introduce test gasses. A butt-coupling is accomplished by placing a cleaved end from the HC-580 and one end from a length of solid-core multimode fiber on nano-positioning stages under magnified camera observation. Both fiber ends are placed in the precision-etched V-groove of a silicon fiber-terminator. UV-curing

glue is applied, and the relative positions of the two fibers are fixed. Measurement of coupled pump light during the curing stage ensures fairly good alignment. The purpose of this mounting configuration is to leave a several micron gap in between the two fibers. Then, the coupling assembly is placed into a high-pressure chamber with the two fibers exiting the chamber through graphite high-pressure capillary ferrules. The gap in between the two fibers allows gasses under pressure to enter the PBF for analysis, and exit through the atmospheric pressure pump-light input end of the fiber near the coupling lens.

The remainder of the forward-scattering setup is quite simple. Raman emissions emerge from the butt-coupled end of the HC-PBF along with a significant portion of the original pump light. These signals then enter the multimode fiber after expanding in free space over a few microns. The efficiency of this coupling (as measured with residual pump light before and after coupling) was found to be less than 20% in our most successful attempt. Light emerging from the multimode fiber was re-collimated in a  $\sim 1\text{cm}$  EFL fiber collimator. The collimated beam was passed through the same edge filter [31], and then focused into the measurement spectrometer with a 6cm singlet. Spectra were again recorded using the same detection system utilized in the free-space experiment.

Unfortunately, a number of problems were encountered when actually attempting to implement the forward-scattering experiment for atmospheric gas measurements. A significant amount of Raman light is lost in the coupling between fibers. This leads to unnecessary reduction of signals, which tends to offset the gains realized by using a PBF system. Also, the V-groove system was intended to ensure stable coupling in a variable-pressure chamber. Under the application of several atmospheres of pressure, this coupling method was found to grow increasingly unstable. This is thought to be the result of glue-bonding that reacts unevenly to

applied pressure resulting in offset fiber positions. Finally and most importantly, this method was shown to exhibit an additional source of background noise; namely silica Raman generated mostly in the solid glass collection fiber.

Figure 14 shows the spectrum recorded in the forward-scattering configuration with only standard atmospheric pressure air-gasses inside the fiber:

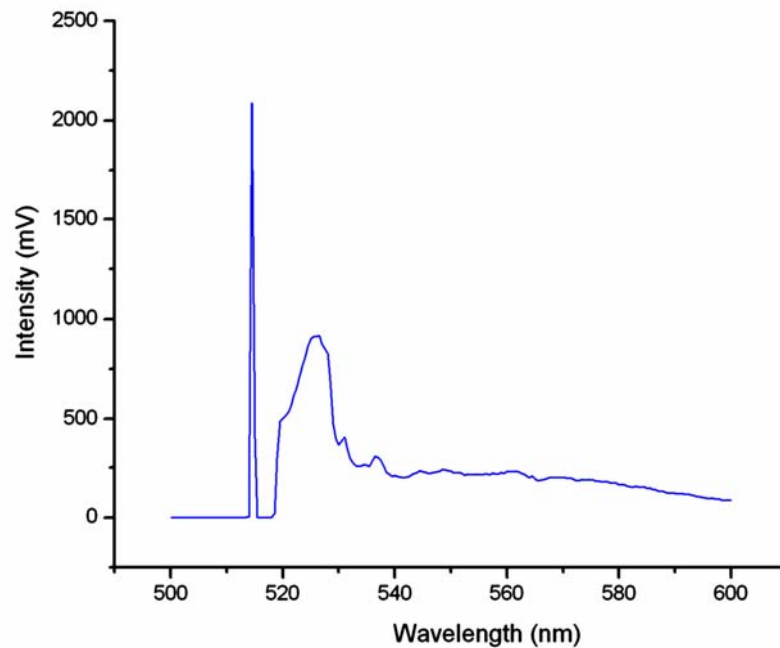


**Figure 14 – PBF forward scattering spectrum in air**

The most intense feature in the Figure is a large residual pump line at 514.5nm. Moving right of the pump line, we note a small region of dark-noise level (no illumination) spectrum which ends at about 520nm. This is due to light being attenuated in this region by the pump-rejection filter. At wavelengths longer than about 520nm, we note a large peak followed by a mostly monotonically decreasing tail continuing through the end of the fiber transmission band. In this system, barring a number of anti-reflective coatings, most of the light interactions take place in

either air or glass. The large background signal from 520nm to more than 600nm in Figure 14 was determined to be the Raman spectrum from solid silica glass.

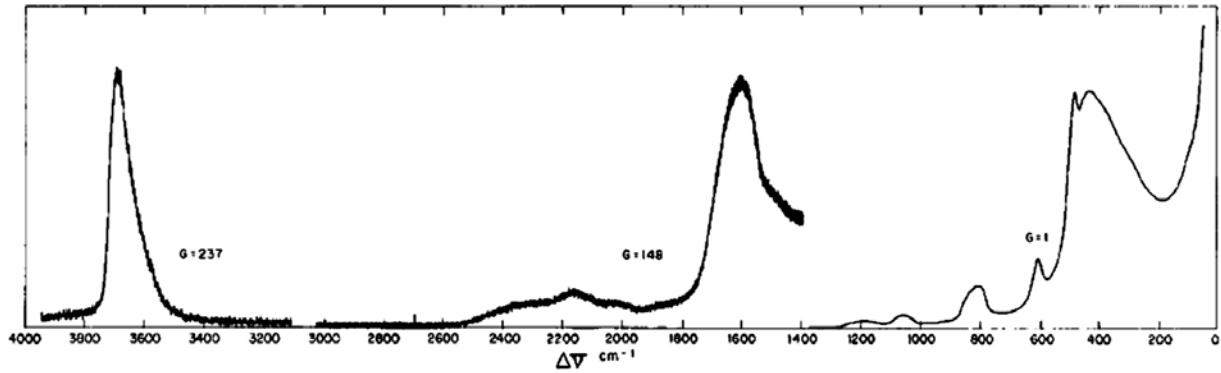


Figure 15 is a reference Raman spectrum of synthetic fused silica. Although the x-axis in Figure 14 is reversed and scaled differently as compared to

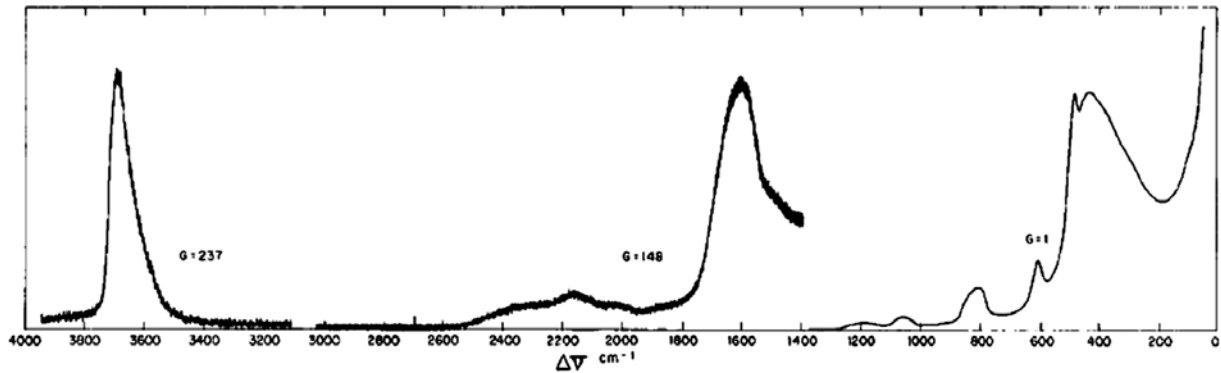
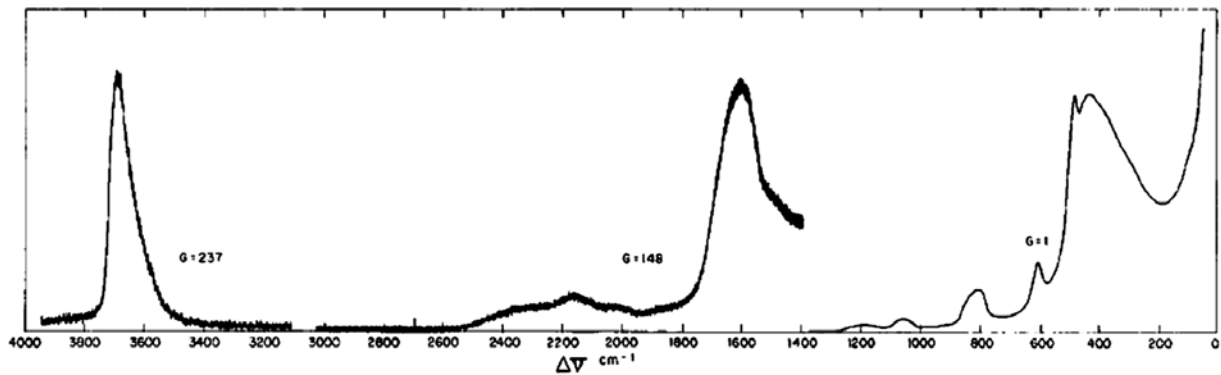
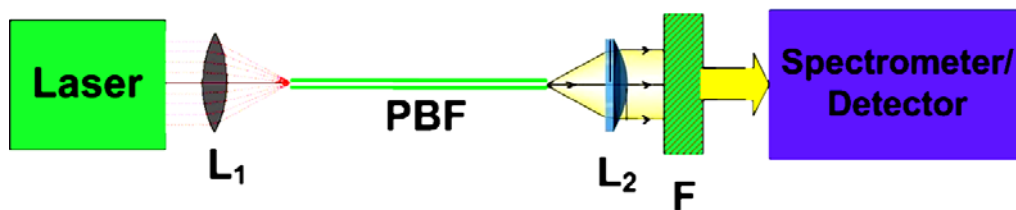


Figure 15; quite a few similarities exist between the known silica spectrum and that obtained in our forward scattering experiment.



**Figure 15 – Silica Raman spectrum from fused silica fiber. The x-axis is reversed and scaled in terms of wave-numbers instead of wavelength [51]**

No gas-Raman signals could be viewed in the forward-scattering experiment with butt-coupling. That is because the magnitude of the silica-Raman signal was much larger than the expected magnitudes of gas-Raman signals. Indeed, the integrated Raman cross-section of the silica is much greater than any of the gas Raman cross-sections. The silica spectrum is also continuous over wavelength due to the amorphous nature of the glass providing a myriad of different bond-lengths to resonate at all wavelengths close enough to the pump frequency. We note that this configuration exhibits a fatal flaw with respect to silica Raman generation. The large portion of the pump beam emerging un-attenuated by the PBF is allowed to couple into the solid core of the multimode fiber. Most of the observed silica Raman is generated in the solid core, and is effectively collected and transferred to the measurement spectrometer. Although gas Raman signals were observable in this configuration using high-pressures, this data will be presented later in Chapter 4. Citing numerous inadequacies, it was necessary to abandon the butt-coupling configuration and remove the butt-coupling and solid fiber in order to make a valid comparison between PBF and the free-space configuration. Figure 16 shows the forward-scattering experimental setup for quantitative comparison purposes only. No gasses can be introduced into the fiber in this configuration.



**Figure 16 – Modified forward scattering configuration**

This experimental setup eliminates the butt-coupling and multimode fiber from the optical train. Although gas-introduction was impossible, atmospheric gas-Raman signals were

observable in this configuration, which could be used to compare with free-space results. Figure 17 shows the spectrum produced in this configuration:

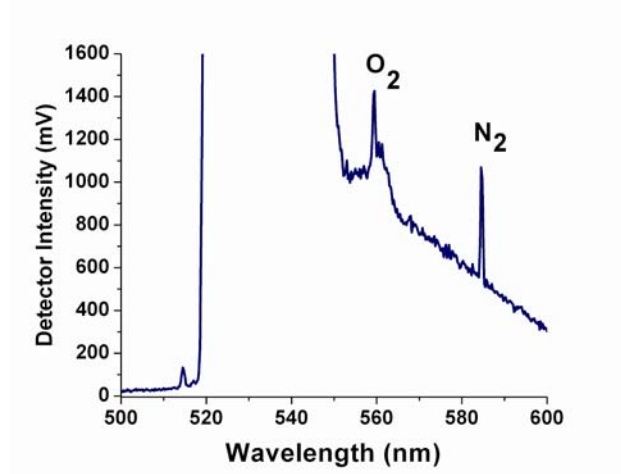


Figure 17 – Modified forward scattering spectrum in air

Two gas-Raman peaks are clearly visible from Nitrogen and Oxygen as they were in the free-space configuration. A much smaller band of amorphous silica Raman is still present starting near the edge filter’s cutoff wavelength and continuing throughout the fiber transmission band.

The Figure shows that the N<sub>2</sub> Raman line at 2331 cm<sup>-1</sup> (584.5 nm) collected from a 1.5-m piece of air-filled HC-PBF is more than 130 times greater than that obtained in free space. This enhancement is consistent with that predicted from Eqs. (3) and (9) which show that the ratio  $R$

of powers detected is  $R = \frac{L_f \Omega_f P_{lf}}{H\pi(1/(2f\#)^2 P_{lo})}$  where  $L_f$  and  $\Omega_f$  are the fiber length and the solid

angle of the Stokes signal collected by the fiber.  $P_{lo} = 160$ -mW and  $P_{lf} = 45$  mW are the laser powers used in the free-space and fiber experiments respectively. For our fiber, ( $L_f = 1.5$ -m,  $\Omega_f \approx 0.045$  sr) the predicted enhancement ratio  $R \approx 100$ . The measured enhancement is  $152$ -mV/ $1.15$ -mV = 132. Raman Stokes signals are proportional to pump power, and this measured enhancement implies an expected enhancement of  $132 \cdot (160/45) = 470$  for equal pump powers.

(We note that all Raman signal levels reported in this section are *corrected for background*

signals i.e., the background primarily due to silica Raman scattering is subtracted from signal levels shown in the figures.) These careful measurements prove that our theory of collection efficiency is correct and accurate. We have also shown that PBF can be used to provide roughly 2-3 orders of magnitude in signal enhancement over free-space collection. Limiting noise in the PBF experiment is shown to be silica Raman; which is not surprising, given that the HC-580 is purported by the manufacturer to have approximately 5% of the pump light propagating in glass due to the mode profile and air-filling fraction of the fiber.

### 3.3 BACKWARD SCATTERING IN HC-PBF

The advent of computer-designed wavelength-selective holographic multilayer dielectric filters has enabled a number of interesting dichroic (2-color or multi-wavelength) experimental configurations. Today, the availability of dichroic beamsplitters for Raman spectroscopy has enabled the implementation of a backscattering Raman configuration using PBF [43]. This experimental setup is shown in Figure 18:

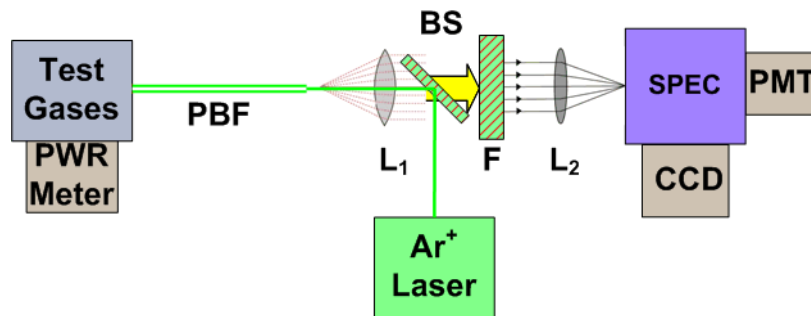
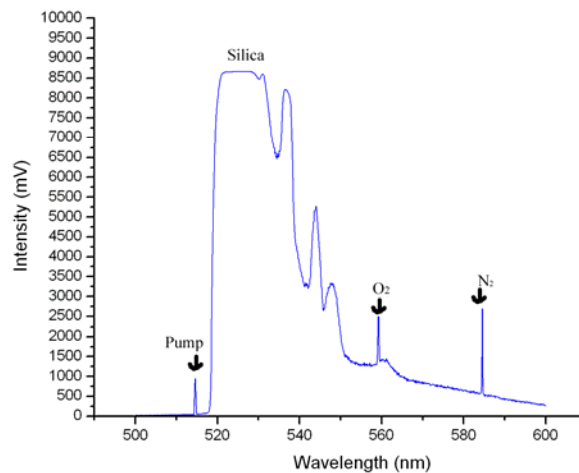


Figure 18 – Backward scattering Raman collection system

In this experiment, the pump beam is first reflected off of a dichroic beamsplitter (BS) [43] before passing through the same 1cm efl aspheric focusing singlet ( $L_1$ ). The pump beam suffers

less than 1% loss in this reflection. Raman generated in the PBF emerges from both ends of the fiber. Raman emerging from the pump input end of the fiber is re-collimated by the input coupling lens and passes with little attenuation through the dichroic beamsplitter. The Raman beam is then filtered by the pump-rejection long-pass edge filter (F) and is focused through a 6cm efl singlet ( $L_2$ ) into the spectrometer. The problem of enabling pump coupling, Raman collection, and gas inlet is solved by essentially combining the pump coupling and Raman collection in a single lens ( $L_1$ ). If the lens is corrected for chromatic aberration, alignment at the pump wavelength accompanies alignment and collimation of the Stokes beam. The other end of the fiber is left free to be fed by a gas source. At no point is the pump-laser beam required to interact with glass over a long distance. Also, very little attenuation of the Raman beam is presented by the beamsplitter. Finally, the relation previously derived for signal improvement (Equation 15) applies to this setup, indicating superiority of the forward-scattering method.

Figure 19 shows the spectrum obtained from the HC-PBF backscattering configuration in atmospheric pressure air.



**Figure 19 – PBF backward scattering spectrum in air. Raman lines are visible from nitrogen and oxygen in ambient air. A background of silica Raman is present along with some residual pump-light**

The notable features in Figure 19 are similar to those in Figure 17. Firstly, there is some residual pump light present at 514.5nm. A similarly shaped silica Raman band also exists. Stokes lines from Nitrogen and Oxygen appear in similar ratios. The most significant aspect of this spectrum is that the signals are significantly larger than in the forward scattering configuration. Although some degree of enhancement is predicted by Equation 15, the published value for loss in the fiber does not directly seem to correlate to the gain achieved in the backward versus forward configurations. The factor of improvement is actually larger than expected. This could be because either the loss in the fiber was significantly larger than the published value, or some additional effects are at work causing unexpected power gains in the backward direction. In any case; the gains realized in power, coupled with the ease of alignment and gas input, leads us to conclude that the backward configuration is vastly superior to all others attempted.

### **3.4 DETECTORS AND THEIR CHARACTERISTICS**

Several different types of optical detectors are available for the detection of low-light level signals commonly encountered in Raman experiments. Each of these has its own advantages and disadvantages. Furthermore, factors like quantum efficiency, dark noise, size, and cost vary widely for different types of detectors, with some degree of overlap existing in available features amongst different detector architectures and technologies. It will be our goal to review the operation and features of several different types of detectors with respect to Raman spectroscopy and gas-Raman experiments. We will focus mainly on photomultiplier tubes, photodiodes, and CCD devices.

Photomultiplier tubes are the oldest and most widely used detectors for low-light level work. A basic photomultiplier consists of a charged photosensitive cathode plate which emits electrons when struck with incident photons. The photon quantum-efficiency of any known photocathode is less than 1, with less electron emission than photon excitation. Electrons produced at the photocathode are accelerated by a large electric potential onto a series of dynodes at increasing electric potentials. As an electron strikes a dynode, it frees a number of secondary electrons; which are in turn accelerated to the next dynode. Electrons are collected at the anode after being emitted from the penultimate dynode. This system of electron-multiplying dynodes enables a few single photons to produce a large electric current pulse. Figure 20 shows the various components in a PMT:

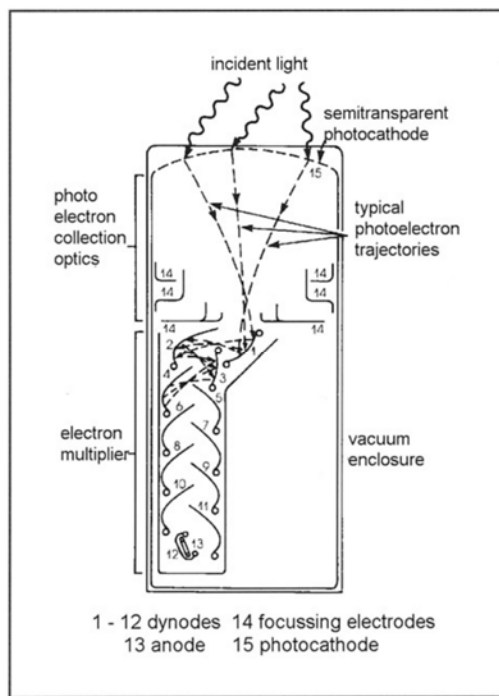


**Figure 20 – Typical PMT components [53]**

PMTs are often very good choices for Raman measurements. Firstly, the electron multiplication scheme allows extremely low-power optical signals to be recorded with inexpensive electrical measurement techniques. Common values for photoelectron current

responsivities are on the order of 100mA/W. In addition, some PMTs can exhibit extremely low dark noise. Most of the dark noise produced by a PMT is from thermionic emission [53]. Dark current is then mostly governed by temperature according to Richardson's Law:

$$\text{Equation 24: } I_d = 120 * T^2 * e^{(-11,600 * \Phi_t / T)} \text{ amps/cm}^2$$

where T is the temperature (Kelvin), and  $\Phi_t$  is the thermal work function for the cathode material. To find the dark-current for a particular photo-cathode, we can multiply Equation 24 by the cathode area. Because thermionic noise is the primary source of noise in most PMTs, we note that cooling most common cathode materials to  $\sim -40^\circ\text{C}$  results in as large as a 10 or 20X improvement in dark counts; making cooled PMTs very quiet and ideal for low-light measurement.

PMTs also present some difficulties. Firstly, a high voltage is required to accelerate electrons in the tube. Applied voltages usually range from 1000-5000 volts D.C. In addition, low level light sensing requires low dark-noise, and therefore extensive cooling. Common cooling methods include thermo-electric coolers (Peltier devices) and liquid nitrogen cooling. Finally, the operation of PMTs designed for low-light applications (photon-counting) require separate pulse discrimination and counting systems. Current pulses emerging from the anode of a PMT exhibit an amplitude variation shown in Figure 21. The vertical axis represents the number of pulses per unit time each having some particular pulse amplitude plotted on the horizontal axis. Those PMT output pulses that have smaller amplitudes are generated by tube and amplifier noise, and need to be discriminated before the counting stage. Likewise, those pulses having extraordinarily high amplitudes are most likely not the result of incident photons, and should also not be counted. The remaining pulses with amplitudes within the specified range are then counted. Dividing the output counts-rate by the quantum efficiency of the tube yields the approximate number of photons incident on the PMT cathode. Although this method is an

accurate technique for photon counting, the additional requirements of high-voltage supplies, coolers, and discriminator/counter units usually make such a system rather large and expensive [54].

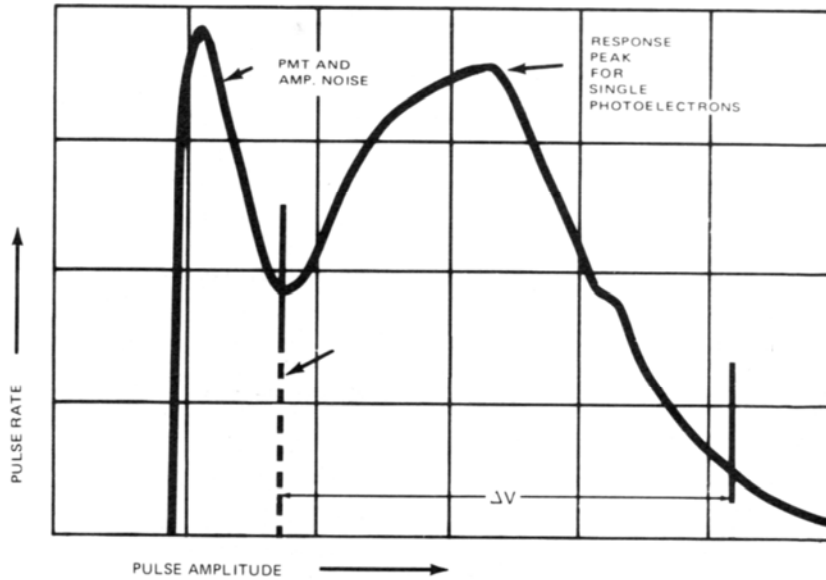


Figure 21 – PMT pulse distribution [55]

The least expensive alternative detector for low-light applications is the photodiode. Therein, a P/N junction is formed in any of a number of semiconductor materials, with optical sensitivities being determined primarily by the bandgap of the semiconductors. Most commonly, silicon is exploited for visible wavelength operation, and germanium or indium-gallium-arsenide are used for near-ir applications. Figure 22 shows the relative responsivities of three different photodiode detectors. Although less useful for Raman experiments, we should note that photoconductive Indium-arsenide and indium-antimonide detectors are usually used for applications requiring mid-ir detection [51].

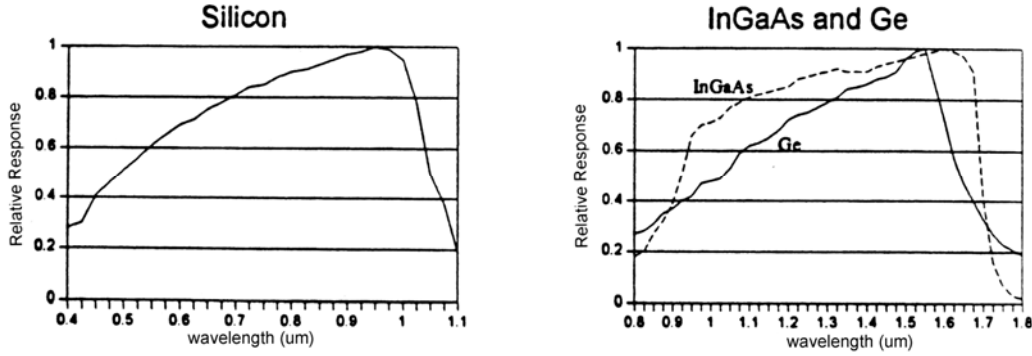


Figure 22 – Common photodiode responsivities [52]

Although the responsivity of some photodiodes can approach that of some PMTs, the primary drawback of photodiode operation is a high level of intrinsic noise, which prevents measurement of extremely low light-power levels. Noise in a photodiode is primarily a result of three sources; namely electron current fluctuations (shot noise), the thermal motion of conducting electrons (Johnson-Nyquist noise), and the flux of incident photons (quantum noise). The first two components may be used to estimate the dark noise voltage, and therefore the lowest possible value of detectable photocurrent. The cathode current due to shot-noise can be written as [54]:

$$\text{Equation 25: } i_s = \sqrt{2e \cdot i \cdot \Delta f}$$

where  $e$  is the electron charge,  $i_s$  is the cathode current (amps), and  $\Delta f$  is the bandwidth of the measurement. The thermal noise can be written as:

$$\text{Equation 26: } i_t = \sqrt{\frac{4kT \cdot \Delta f}{R}}$$

where  $k$  is Boltzman's constant,  $T$  is the temperature (Kelvin), and  $R$  is the load resistance observed by the photodiode. If we combine Equation 25 and Equation 26 and rewrite in terms of rms voltage, we arrive at the noise voltage for the photodiode:

$$\text{Equation 27: } V_n = \sqrt{2R^2ei \cdot \Delta f + 4kTR \cdot \Delta f}$$

$$\text{or } V_n = \sqrt{eR \cdot \Delta f \cdot \left[ 2Ri + \frac{4kT}{e} \right]}$$

In an uncooled photodiode,  $4kT/e \approx 0.1$ . Shot noise will dominate if  $2Ri > 0.1$ . Assuming a maximum load impedance of  $10^9$  ohms, we determine that the maximum photocurrent in which thermal noise will not dominate is about  $5 \cdot 10^{-11}$  amps. This is an approximation of the lower limit of current measurable using a photodiode. Of course, the thermal noise may be reduced by lowering the junction temperature. Common methods for accomplishing diode cooling are most often thermo-electric, as cooling down lower than  $\sim -40\text{C}$  is usually not beneficial. Despite being much noisier than PMTs, photodiodes do still offer a much less expensive and much more portable detection solution.

Since their invention at Bell Labs in 1969 (Boyle and Smith), charge-coupled devices (CCDs) have proven to be extremely useful for photometric applications ranging from consumer photography to orbital telescopes [55]. Consequently, they are also formidable detectors for use with Raman spectroscopy in low light detection. CCDs are comprised of hundreds or even thousands of photodiode-like structures imprinted on semiconductor substrates. Although in terms of their operational theory being governed by the photoelectric effect, they are exactly the same as a single bulk photodiode. The thermal noise per unit area in such a device is similar to large photodiodes. In practice, each single detection element or pixel contains a much smaller detection area, and therefore exhibits much lower total noise. The realization that the tiny electrical charge stored in a CCD pixel could be shifted across the surface of the semiconductor (in a manner similar to that in which a shift-register moves logical bits) allowed CCD arrays to be designed to exploit the low noise levels associated with small photosensitive elements [56].

Because of their utility and low cost/pixel, a number of interesting variations on the CCD have emerged. The intensified CCD array employs a photocathode (similar to a PMT) along

with an array of electron-multiplication channels to allow even lower-light detection than in an un-intensified array. The advent of back-thinning; or etching away the CCD substrate from the back (and illuminating the device from the back), helps to improve quantum efficiency and short-wavelength response. Such arrays exhibit peak quantum efficiencies in the 90% range, and are thus great choices for Raman experiments. Furthermore, the ability to illuminate hundreds of pixels simultaneously allows for imaging of a Raman source (as we shall see in Chapter 4).

Although the PMT, the photodiode, and the CCD do not by any means comprise an exhaustive list of optical detectors; they are the most useful three used for Raman gas detection experiments in current incarnations. Tradeoffs in cost, dark noise, and responsivity ultimately dictate which detector should be used. In the following experimental sections, we will review testing done with all three types of detectors, and we will point out the reasoning behind each usage as it presents itself.

#### **4.0 HYDROCARBON SENSING AND NOISE REDUCTION**

After determining the essential utility of HC-PBF based Raman gas sensors, it was necessary to perform sensing experiments in a number of pure and mixed gases of interest; each being introduced under pressure into various fibers. The goals of these experiments included determining signal-to-noise ratios and thus inferring minimum detection limits in particular gases. The actual implementation of a number of different sensing configurations allowed for the evaluation of the practicality and physical stability of each particular geometry.

Initial sensing experiments were performed using visible (514.5nm) light and forward scattering. These experiments will be examined first, with emphasis placed on the limitations of the mechanical coupling stability first noted in Section 3.2. Despite these difficulties, Raman spectra for various hydrocarbon and other gases were produced. The next section will detail similar backward-scattering experiments using the same pump-source. This system was shown to be much more stable and reliable due to the lack of fiber butt-couplings. Next, an IR pumped (~780nm) system was examined in the backscattering configuration. With each of these systems, techniques for noise mitigation were explored. A final section on silica Raman noise reduction deals with the factors governing system noise, and the resultant sensitivities after our attempts at noise reduction.

#### 4.1 VISIBLE WAVELENGTH FORWARD SCATTERING

The first successful spontaneous Raman scattering pressurized gas-sensing experiment in HC-PBF was performed by us using a 514.5nm single-line argon-ion pump beam and a length of Crystal Fiber HC-580 [41]. This experiment was intended to provide key details surrounding the difficulties that would undoubtedly arise in the exploitation of this novel sensing geometry.

Figure 23 shows the components necessary for testing:

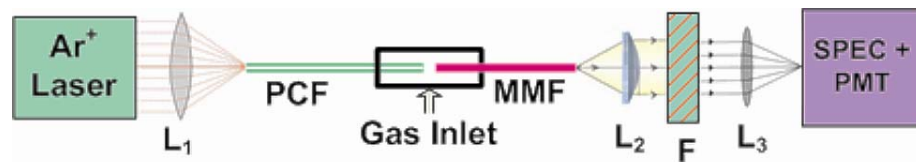
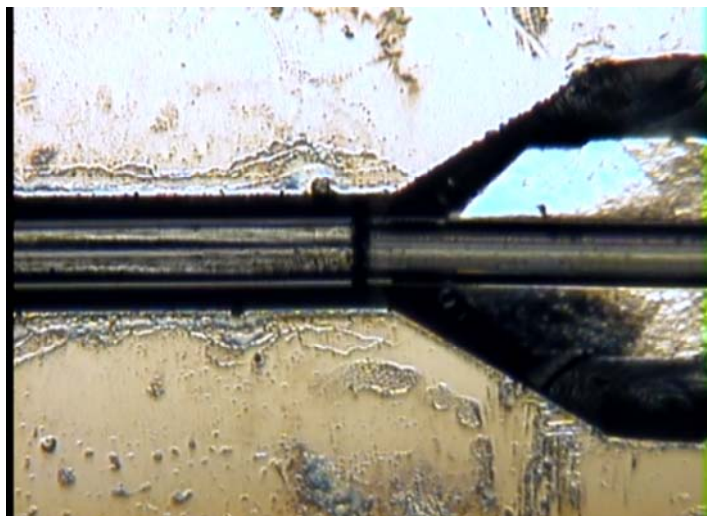


Figure 23 – Experimental setup, forward scattering

Therein, a ~200mW 514.5nm TEM<sub>00</sub> pump beam was focused through a 10mm anti-reflection coated aspheric singlet into a 1.5m length of HC-580. Pump power throughput was measured at the output of the bare fiber at between 40% and 60%. It should be noted that the coupling of a 1.4mm laser beam into this fiber's ~5um core is rather difficult, and required the purchase of a differential-micrometer driven nano-positioning stage in order to achieve better than 50% coupling efficiency. After pump-coupling efficiency was established, the other end of the fiber was aligned to a number of different solid-glass waveguides on a fiber alignment station with two-axis microscope viewing. Figure 24 shows a micrograph of one of these couplings. The entire coupling assembly was placed inside a chamber designed to contain gases at high pressure. Both the PBF and large waveguide exited the high-pressure chamber through two 1/16" graphite ferrules in Swageloc fittings. The remainder of the experimental setup included a collimator at the output-end of the coupled waveguide for collimating Raman signals, a long-pass edge filter to eliminate forward-traveling pump light, and a 6cm efl singlet to focus light into the acceptance

cone of the spectrometer. The spectrometer was a JY 55cm-focal-length holographic grating spectrometer with a PMT (EMI 9789), a discriminator for photon counting, and a cooled silicon photodiode for additional measurements.



**Figure 24 – Microscope image, fiber-to-fiber butt-coupling**

Although we will only briefly summarize the results of output-waveguide-coupling experiments here, extensive tests were performed to determine the best method for coupling the output of a PBF to a larger waveguide while maintaining a small gap between the two. The gap would eventually allow introduction of test gases into the PBF. In general, one end of an HC-PBF was placed on top of an etched silicon V-groove and was held in place with a drop of UV curing epoxy. Extreme care was taken to cure the epoxy before surface tension caused the wicking of the epoxy into the core or cladding holes at the end-face of the fiber close to the glue-site. After curing of this glue, an output waveguide was positioned a few microns away from the PBF, and was also glued in place. This alignment usually needed to be accurate within less than 1 micron, or high coupling losses would result. A number of different output waveguides were employed including a small core ( $4.2\mu\text{m}$ ) single mode fiber (Corning EDFT6), standard single-mode SMF-28, telecommunications multimode fiber ( $62.5\mu\text{m}$ ), and large core multimode fiber

(110 $\mu\text{m}$ ). In each case, coupling efficiencies and stabilities were evaluated. The ideal coupling waveguide would provide extremely stable performance, low light loss, and high-coupling efficiency when placed a few microns from the output of the PBF. The most reliable coupling was determined to be the 110 $\mu\text{m}$  core-diameter multimode fiber. Because its outer diameter is similar to that of the PBF, it was easy to position on the V-groove. Also, because its core is more than 20 times larger than that of the PBF, it was much easier to align to the expanding PBF output-mode without much loss.

After sufficient coupling was established, gases were introduced into the PBF under pressure. During initial pressurization, the residual pump power measured at the output of the large waveguide was noted to fluctuate severely. This was an indication that the coupling assembly was not maintaining fiber alignment under changing pressure. It is estimated that because the coupling assembly is not radially symmetric (i.e., it is comprised of a substrate on which fibers are glued), it is susceptible to uneven compression forces resulting in misalignment. Despite being unstable under changing pressure, as soon as analyte pressure stabilized, output power stabilized as well.

Since our coupling technique enabled the introduction of gases into PBF, despite being inherently unstable, it was possible to view the Raman spectra of various pressurized hydrocarbon gases. Figure 25 is a collection of single-gas hydrocarbon spectra including methane, ethane, propane, and nitrogen. Therein, principal vibrational peaks from each gas are noted above a strong silica-Raman background. The pressure of each gas is 100psig at the input to the fiber, with the output of the fiber remaining at 0psig atmospheric pressure. The relative Raman signal magnitudes were not stable enough to compare with known Raman cross sections.

Raman signals were recorded using the PMT with photon counting and A/D sampling at 100,000counts/V/second.

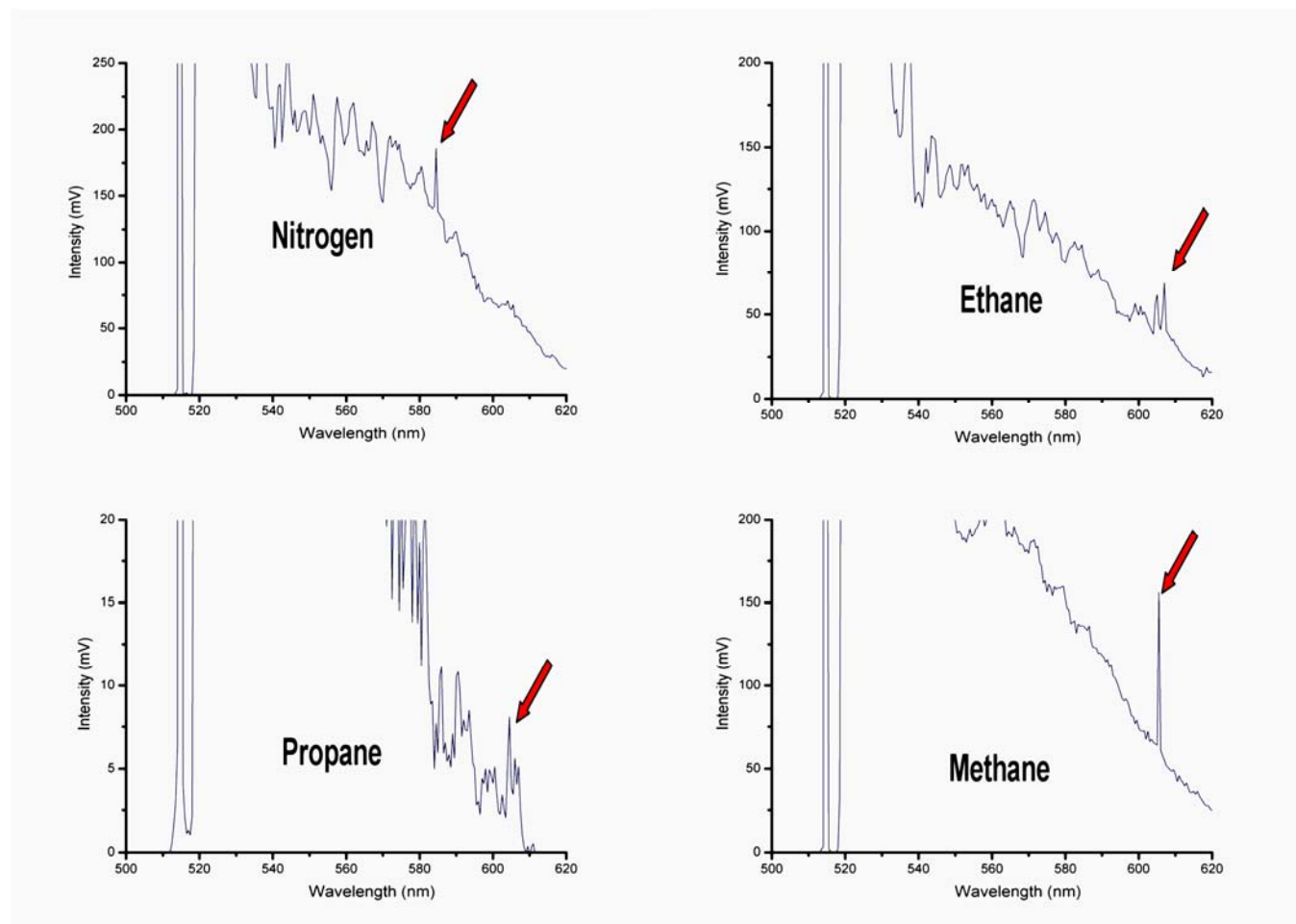


**Figure 25 – Forward scattering single gas spectra**

After determining that single gases were readily measurable using our PBF system, a number of hydrocarbon gas mixtures were introduced into the fiber. This demonstrated firstly, the absence of significant molecular capillary separation under the relatively low pressure and low flow induced during testing; and secondly, the absence of extraneous optical or mechanical features preventing such measurement. Figure 26 shows a spectrum resulting from multiple gases in the PBF sensor. The mixture is comprised of a partial gauge pressure of 100psi propane, 50psi methane, and 50psi ethane. Although this mixture is not representative of any

standard natural gas mixture, it was designed to allow similar measurable signal-to-noise ratios in each gas; and thus facilitate measurements pertaining to each gas. Also, the instrument-limited line widths shown in the Figure seem to blur together in this low-resolution spectrum, despite these lines being clearly separated in frequency space given the line width of the pump and Raman vibration.

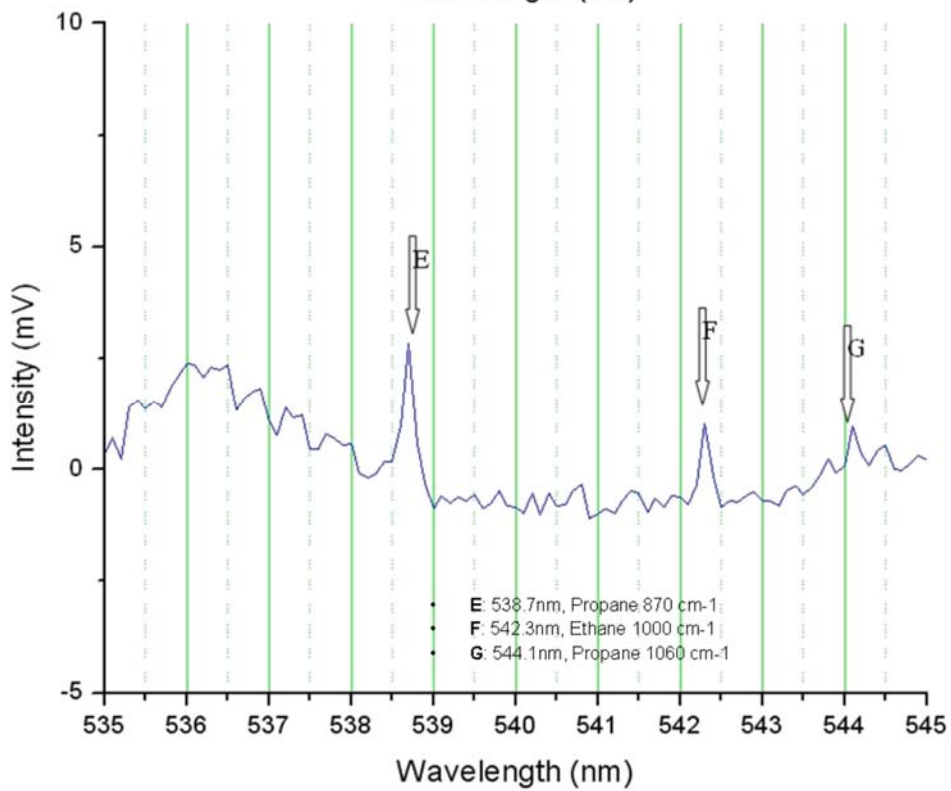
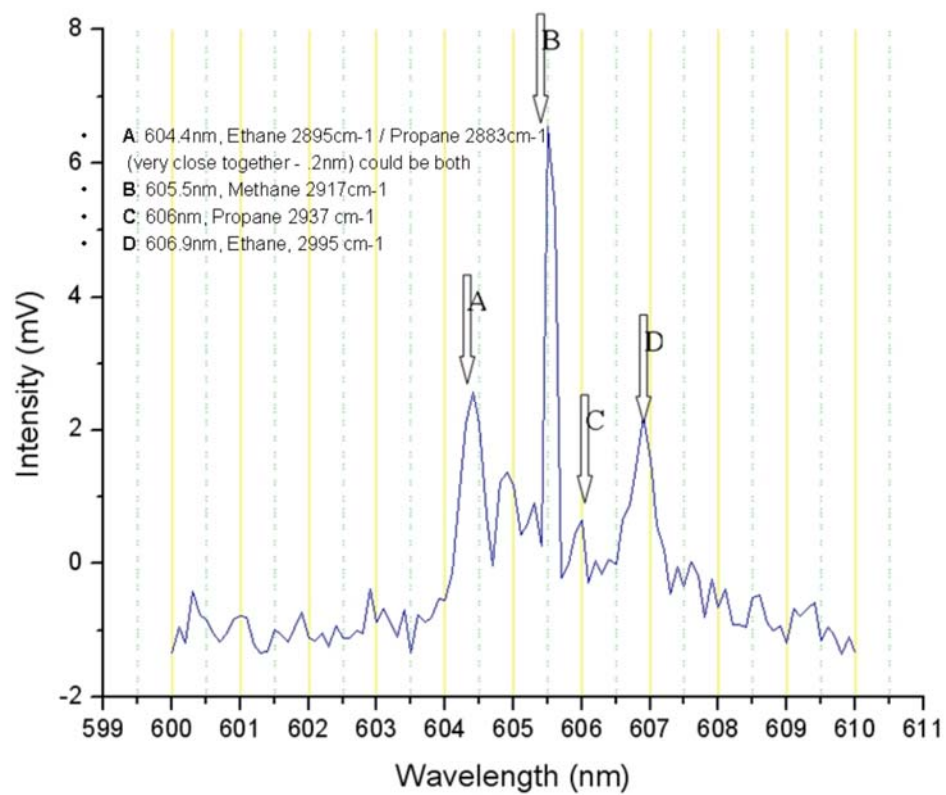


Figure 26 – Forward scattering, multi-hydrocarbon spectra

Some marginal success was indeed realized using a forward scattering system. This success is purported in the large signal magnitudes observed in the preceding Figures. Unfortunately, measurement of the SNRs in these experiments highlighted the drawbacks of the system. The background level in these experiments was again determined to be silica Raman. Herein, the silica Raman background was noted to be extremely high per unit pump power. When compared to spectra obtained in free-air without any butt-coupling arrangement, a large portion of the silica Raman background was determined to be emanating from the large output waveguide. This was true for all waveguides utilized. It is noted that after some coupling loss, a large residual pump beam remains to excite Raman in the collection-waveguide. Although this could be improved upon through the use of a pump-rejection filter placed between the PBF and collection waveguide, this arrangement would require placing an additional optical element in the high-pressure chamber, which may further complicate coupling. It is far more logical to attempt to eliminate these problems with a backward scattering configuration.

The final difficulty noted in operating the forward scattering system was the susceptibility of the PBF to transmission loss under pressure. While introducing analyte gases into the PBF, we noted that occasionally transmission would fall dramatically and would occasionally never recover. This loss in transmission was accompanied by changes in the single-mode far-field diffraction pattern observable in the residual (green) pump beam at the uncoupled fiber's output. Occasionally, a tiny bright-spot was observed from the side of the fiber; behind which the usual amount of pump-scattering was eliminated. (note: the HC-580 radiates a visible green glow due to pump loss along its length) We noted that some recent work has been done in particle guidance inside a PBF. We deduced that these losses in transmission were undoubtedly the result of particulate matter entering either the core or cladding holes in the fiber

under pressure; resulting in larger than expected light losses. In an attempt to prevent particulates from entering the fiber and ruining its transmission, the high-pressure chamber was fitted with a 0.5 $\mu$ m ceramic particulate filter capable of enduring high gas pressures safely, while delivering more than adequate gas flow. Although this procedure seemed to increase the number of gas-tests which could be performed using a single PBF, it did not entirely prevent the transmission loss problem from reoccurring. Further solutions to the fiber degradation problem are given in the following section.

## 4.2 VISIBLE WAVELENGTH BACKWARD SCATTERING

After gathering initial results in pressurized forward scattering experiments, as well as gaining a visceral understanding of the alignment and construction procedures necessary to produce a PBF sensor, it was possible to conduct careful backscattering collection and further improve our sensing technology. This included completing the gas delivery system to inject gases under high pressure into the backscattering sensor. Then, gas pressure and concentration analysis was performed using this system.

Figure 27 shows the experimental setup utilized for backscattering analysis of various gasses. It is again similar to the experimental setup used for atmospheric analysis. The ~100mW 514.5nm pump beam was coupled through the same dichroic beamsplitter and 11mm aspheric singlet into an additional length of HC-580 (1.5m). The backward-emerging Raman beam was again additionally filtered using a holographic edge filter [43], and was subsequently focused into the spectrometer for measurement. This time, an intensified silicon array detector was utilized for measurement (EG&G 1420IR). This detector is comprised of a photocathode

with a fiber-coupled multi-channel intensifier plate and 1024 element Peltier cooled silicon CCD detector.

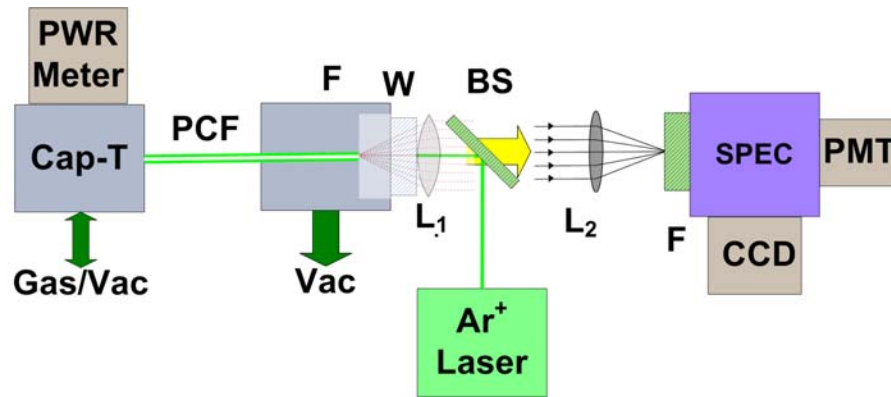


Figure 27 – Backscattering system with gas handling

The use of an array detector provides an additional opportunity for multi-gas sensing. The array detector is comprised of 25 $\mu$ m wide by 1mm high pixels. Given a spectrometer-dispersion of 1.37nm/mm, 0.0343nm worth of spectral content falls on a single pixel; indicating the best possible spectral resolution. Over the entire 1024 element array, a  $\sim$ 35nm portion of a Raman spectrum can be recorded in one integration period. In many cases, that allows the measurement of multiple gases in a spectral window without taking the time to move the grating and re-sample the spectrum. If we review Figure 26, we note that the simultaneous measurement of methane, ethane, and propane gases could be performed using one of two portions of the spectrum for quick natural gas analysis.

Several important gas-handling features were added to the gas-transfer system shown in Figure 27. It is helpful to continuously measure the pump power exiting the PBF in order to maintain optical alignment in this experimental system. In addition to measuring the power throughput at the pump-exit end of the fiber, it is also necessary to introduce gases at the same point. To accomplish these rough power measurements, a low-volume capillary T-fitting was connected to the pump-output end of the PBF. The opposing branch of the T-fitting was fitted

with a short length of large-core (110 $\mu\text{m}$ ) multimode fiber (which was also used in forward butt-coupling experiments). This multimode fiber was positioned such that a large portion of the residual pump (and inconsequently forward scattered Raman) would couple into it. This light was then allowed to propagate onto a silicon photodiode-based power meter. Although the coupling between the PBF and multimode fibers was not very good, and was inherently unstable inside the T-fitting, it facilitated rough power measurements for alignment purposes. The third branch of the T-fitting was fed by analyte gases. In order to further protect the fiber from particulate contamination, the T-fitting was protected by a micro-capillary guard column and .5 $\mu\text{m}$  filter frit; commonly used in gas chromatography for filtration.

Visible Raman measurements in the backscattering configuration proved extremely successful. Figure 28 displays the spectra of methane and CO<sub>2</sub> gases recorded using the 1D intensified array detector. For informative purposes, the X-axis units in this Figure are reported in “Pixels” rather than wavelength. In the first spectrum, the center pixel represents 605.4nm (the center of the methane resonance), and the second spectrum is centered at 551nm (between the two largest CO<sub>2</sub> Raman vibration lines – 4 such lines are displayed in the figure). It should be noted that some silica-Raman reduction was performed, which will be discussed in the next Chapter. Overall, signals were easily detected due to the increased signal magnitudes in the backscattering direction. In fact, while using long-enough integration times (gas cross-section dependant) it was possible to view the rotational substructure of gases surrounding the principle vibrational lines. Figure 29 shows more clearly the rotational substructure about the 2917 $\text{cm}^{-1}$  line in methane (one-second integration). We note that these rotational lines can often be utilized for more careful identification of complicated gas mixtures, or even for improving signal to noise ratios by increasing measurement bandwidth for correlated measurement.

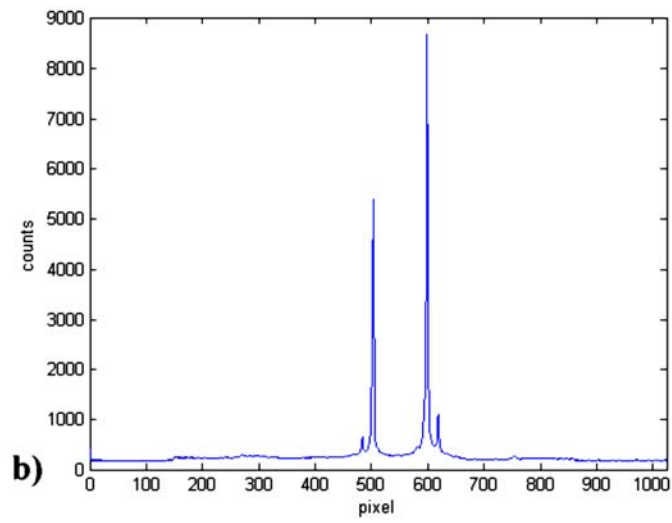
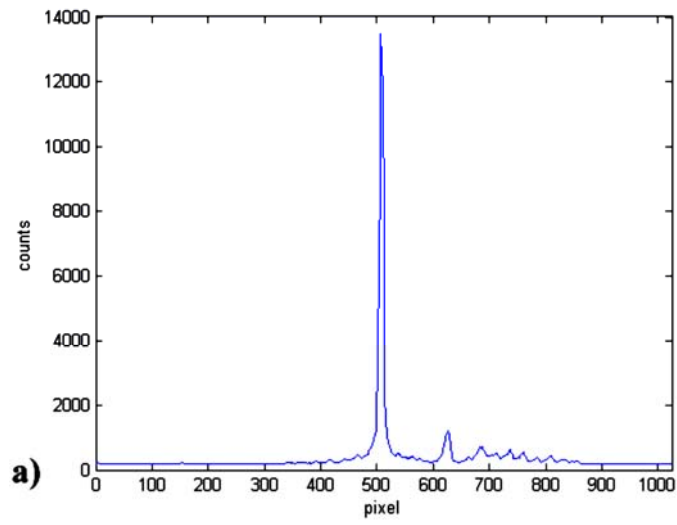
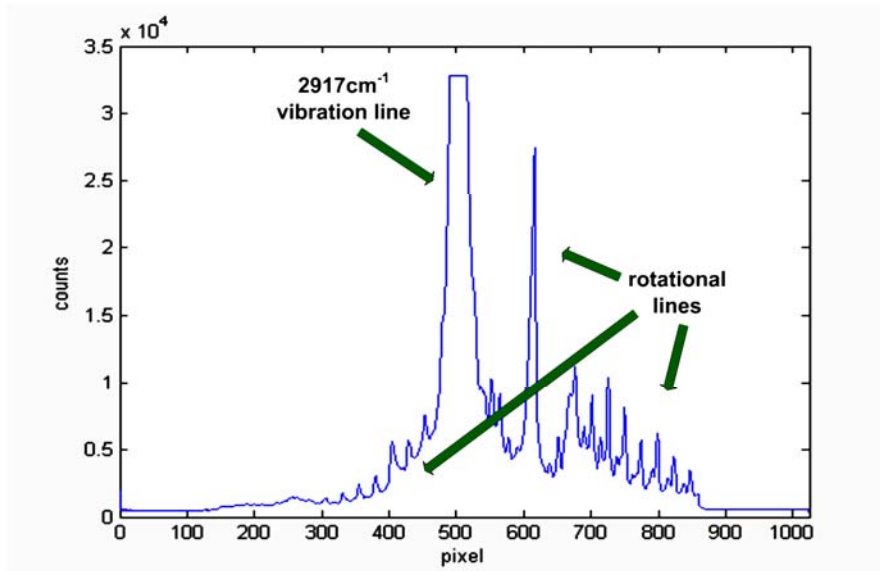


Figure 28 – 1D CCD array pixel data (spectra). a) CH<sub>4</sub> spectrum centered at 605.4nm and b) CO<sub>2</sub> spectrum centered at 551nm



**Figure 29 – Methane rotational substructure about the 2917cm<sup>-1</sup> line**

Since the backward Raman system allowed stable continuous measurement of Raman peaks with signal magnitudes being affected primarily by pump-power variation, it was theoretically possible to conduct concentration measurements of gases within the fiber. To accomplish this, varying mixtures of CO<sub>2</sub> and nitrogen (0-100%) were added to the fiber at 100psig. Recall that the fiber's output remains at 1-atm room pressure (0 psig). Both nitrogen (2231cm<sup>-1</sup>) and CO<sub>2</sub> (1388cm<sup>-1</sup>) peaks were monitored and plotted versus CO<sub>2</sub> concentration (Figure 30). In the figure, linear curve-fits (solid lines) are also shown for the two datasets along with their determination coefficients (R<sup>2</sup>). Ideally, these plots should both consist of straight lines crossing the zero-axis at opposite ends of the plot, with slopes representative of gas cross-sections. Unfortunately, some deviations were noted from these ideal conditions. Firstly, the lines did not cross the zero-axis. In nitrogen gas, the existence of atmospheric pressure at the output end of the fiber added a small signal contribution separate from that provided by the mixed-gas analyte. More importantly, the CO<sub>2</sub> signal presented a large non-zero component after its component concentration was reduced to 0.

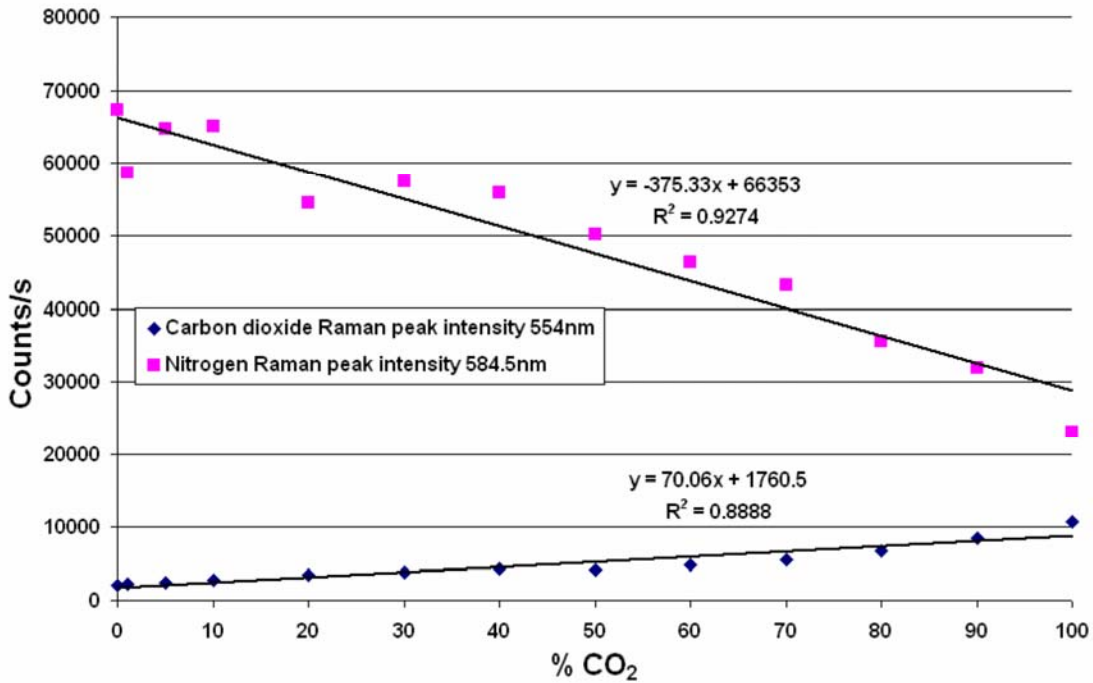
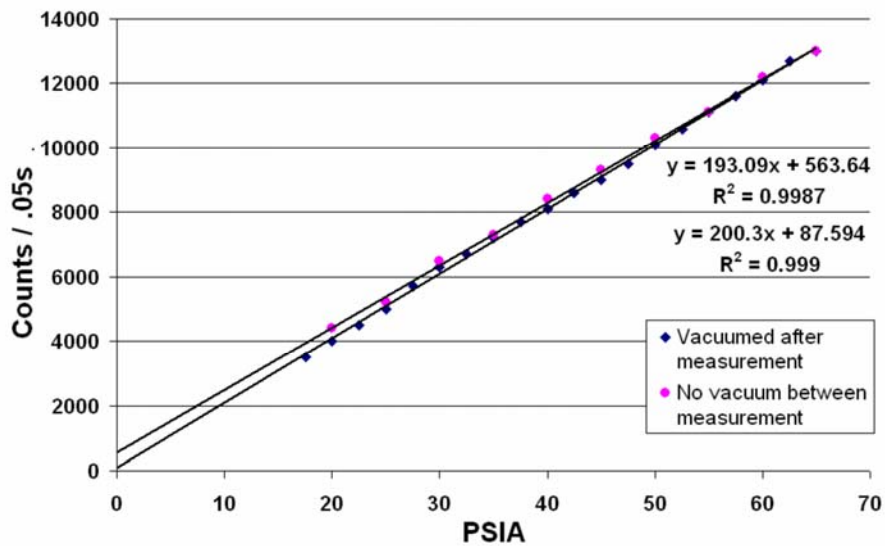
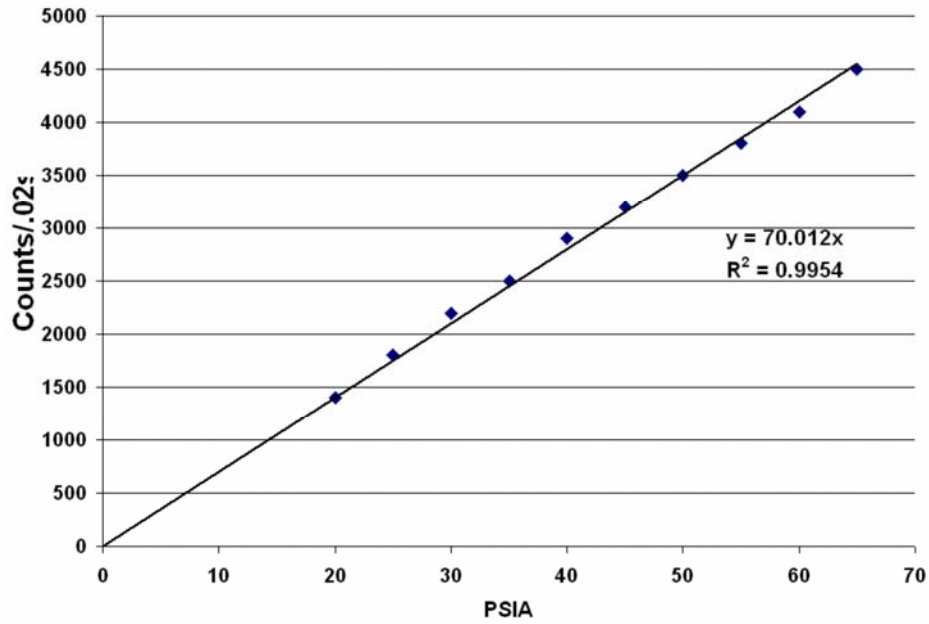


Figure 30 – CO<sub>2</sub> Raman peak magnitude versus gas concentration

It was determined that a large Raman peak from CO<sub>2</sub> gas was present well after the CO<sub>2</sub> pressure had been turned off. Furthermore, re-pressurization and subsequent flow of a completely different gas did not fully eliminate the presence of a CO<sub>2</sub> Raman peak. We believe that this was due to tiny amounts of analyte gas remaining trapped inside the cladding structure in the fiber. In fact, if we calculate the diffusion rate of gases into and out of a <1μm diameter cladding channel, we find that it could take weeks of room-pressure diffusion to entirely remove a trace gas. To immediately eliminate this problem, a vacuum pump (BOC Edwards 8 Series rotary vane pump) was added to the gas delivery system as shown in Figure 27, such that the entire gas-mixing manifold, as well as the pre-fiber filter and the fiber itself could be vacuumed to a pressure of <1mtorr. Recall that the atmospheric pressure fiber inlet will still maintain a pressure of 1atm of atmospheric-composition gases.

In addition to noting the divergence of y-intercepts in Figure 30 from 0, we observe some minor discrepancy in the relative cross-sections (line-slopes) of measured gases. It was further determined that in order to correctly measure a gaseous cross section, the linewidth must be carefully considered. Because Raman cross-sections are often given as spectrally integrated values, it is necessary to provide spectral resolution corresponding to the gas-Raman linewidth of the species in question. This means that in order to use a single-pixel as a concentration detector, we must ensure that all of the collected Raman emissions from a single Raman line are focused onto that single pixel, and that other Raman lines do not fall on that pixel. After adjusting spectrometer slit width (.024mm) and adding a vacuum pumping system to remove trapped gases from the previous measurement, it was possible to produce concentration measurements which were repeatable and linear with no additional zero-offset. One such measurement is shown in Figure 31. Therein, part A shows the peak intensity of a methane line versus gas concentration. Part B shows a CO<sub>2</sub> Raman peak, both with and without vacuum being applied between measurements. Note that the offset in the non-vacuumed plot represents gasses trapped in the fiber.



**Figure 31 – A) top: methane 2917cm<sup>-1</sup> Raman line intensity (counts/.02s) and B) bottom: CO<sub>2</sub> 1388cm<sup>-1</sup> Raman line intensity (counts/.05s) under varying gas pressure. B) includes a plot recorded under descending pressure without vacuum at the output to illustrate residual gases in the fiber**

In general, experiments performed in the backscattering configuration proved the viability of a Raman gas sensor. Gas Raman signals were easily measurable, and gas handling

was easily performed using the single-ended optical coupling system described above. Furthermore, numerous details were revealed regarding the nature of gas-transfer inside a PBF. Although gas flow-rates and transfer times were previously estimated, the rather long out-diffusion times were significantly longer than expected, undoubtedly due to cladding containment phenomena. Shortening gas transfer times and enumerating system gas dynamics will be the topic of Chapter 5.

### 4.3 NEAR-IR BACKSCATTERING

The success of visible wavelength Raman measurements prompted the study of different wavelength systems. Because the delimiting factor in our sensor designs was the availability of commercially distributed PBFs, the next-longest wavelength available fiber (Crystal Fibre HC-800) was used as the basis for a measurement system. By designing and testing this system, we intended to explore the differences in gas transfer associated with the slightly larger core and cladding holes, along with the signal to noise ratios available given the smaller Raman cross sections (by  $1/\lambda^4$  at the longer wavelength).

Figure 32 shows the sensing system based on HC-800 fiber. The transmission band for this fiber was given in Figure 7. Note that the left-hand side of the transmission band for this fiber lies near  $\sim 780\text{nm}$ . Numerous inexpensive semiconductor lasers are available with pumping wavelengths near  $780\text{nm}$  due to easily generable solid-state bandgaps corresponding to emission at this wavelength. In addition, an argon-ion laser pumped, tunable output wavelength, narrow line, Ti:Sapphire laser (Spectra Physics 3900) was available for pumping from  $\sim 700\text{-}850\text{nm}$ . An additional miniaturized semiconductor  $\sim 785\text{nm}$  laser was also obtained. The remainder of the

system was similar to the visible system. Of course, a new holographic edge filter, dichroic beamsplitter, and laser-line filters were purchased for use at the longer wavelength.

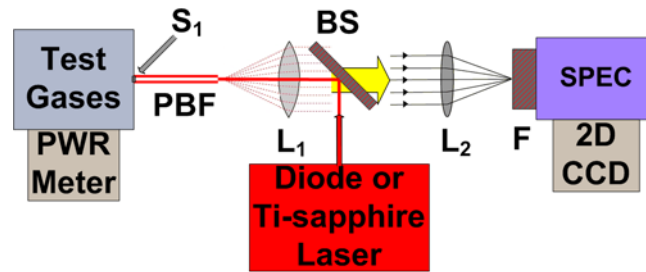


Figure 32 – Near IR backscattering system based on HC-800 fiber

Before embarking on Raman sensing, a number of characterization efforts were undertaken to evaluate the available pump-sources, as well as the new filters. Figure 33 is a spectrum of the chosen semiconductor laser (Mircolaser L4785s-95-TE). In comparison, the Ti:Sapphire laser exhibited far better beam quality and a narrower output line. Spontaneous emission from either laser source was blocked rather well with the addition of a holographic bandpass line filter (>OD 6 in the blocking region).

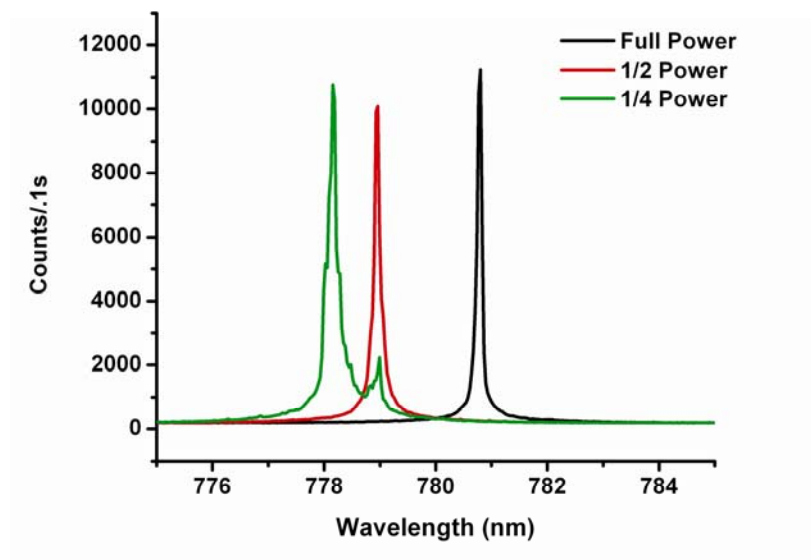
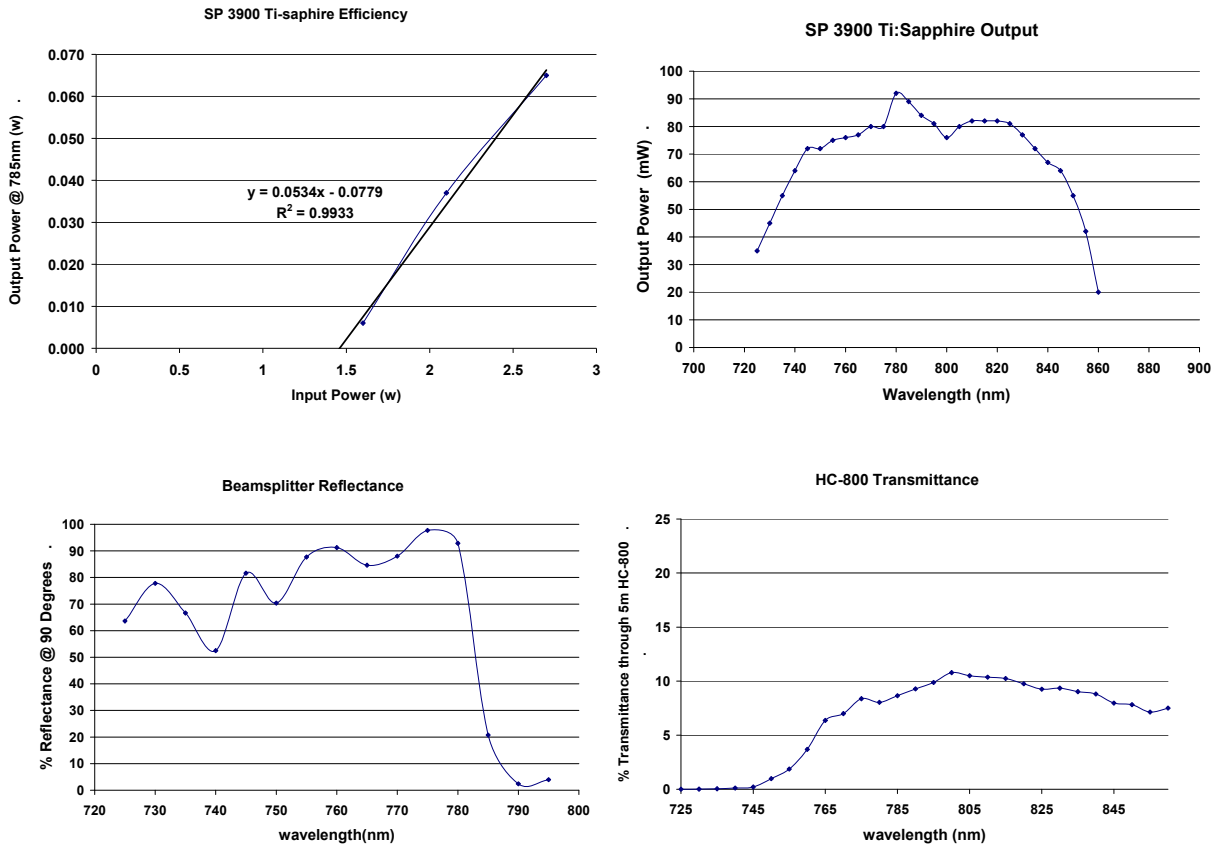


Figure 33 – 785nm Microlaser L4785-95-TE output spectrum

Although both sources provide similar output powers ( $<100\text{mW}$ ), the narrow line features of the Ti:Sapphire laser make it suited for high-resolution work. The diode laser, in contrast, is  $<1/20^{\text{th}}$  of the cost of the tunable Ti:Sapphire laser, and is highly portable. We note that it is possible to “clean-up” the diode laser line using a holographic laser line filter tilted to some small angle such that the longer-wave portion of its output spectrum is attenuated, leaving a narrower transmission region for exciting Raman. This technique also has the adverse effect of reducing output power. In order to avoid these difficulties, experiments in this section utilized Ti:Sapphire pumping. Figure 34 shows the measured output power of the Ti:Sapphire laser, along with the reflected-transmission range of the dichroic beamsplitter and the transmission range of the 1.2m HC-800 fiber used in the experiment. This graph indicates that pumping at about  $\sim 780\text{nm}$  is the ideal wavelength for maximum power throughput.



**Figure 34 – Ti:sapphire efficiency and output power, beamsplitter transmission (90 degree), and HC-800 fiber transmission**

Although the optical collection train was similar to that used in visible experiments ( $L_1$ , and  $L_2$  are the same in Figure 27), an array detector was required with better response in the near-IR range. A 2D, back-thinned silicon, Peltier-cooled array detector was acquired which allowed for imaging of Raman output. The detector consisted of a grid of 1024X252 pixel-elements, each being  $24\mu\text{m} \times 24\mu\text{m}$  square. The longer dimension (1024 elements) was oriented in the horizontal (wavelength dispersed) direction, with the shorter dimension (252 elements) lying in the vertical (imaging) plane. Care was taken to image the output of the fiber onto the array surface. This required ensuring that  $L_1$  (in Figure 32) was one-focal length away from the fiber. Positioning accuracy was first determined by the maximization of pump-power

throughput.  $L_2$  was then positioned approximately one focal length away from the spectrometer's entrance slits, which ensured that a magnified image of the fiber output ( $M = L_2/L_1$ ) appeared at the entrance slits, and subsequently at the detector plane. Finally, in order to gain a clear picture of the noise generated by the array, noise spectra were recorded with the spectrometer's entrance slits closed. Average detector noise per-row is shown in Figure 35. The corresponding average pixel noise per unit time is given in part B of the same Figure. Note that the array exhibits about 1.5 counts/s of integration-time dependent noise, plus about 110 fixed "readout noise" counts over the entire array. Such fixed noise can be subtracted from output spectra, with the remainder containing only the 1.5 counts/s fluctuation.

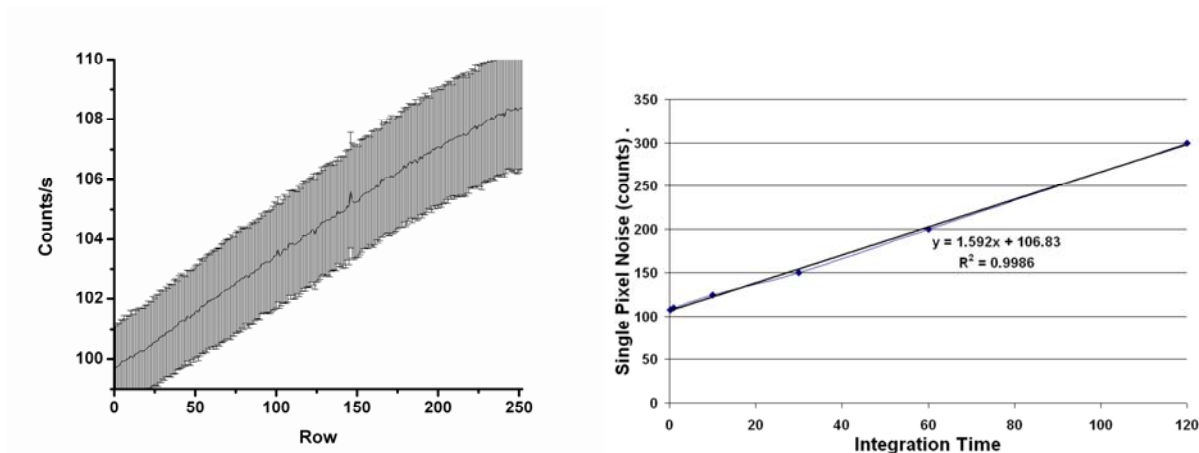


**Figure 35 – 2D cooled silicon CCD array detector noise**

One additional change was made in the gas-delivery setup for these experiments. A sealed vacuum-flange was designed and machined to accept a fused-silica window at the light-input end of the fiber. A vacuum line was connected behind the sealed window, which allowed one side or the entire fiber to be vacuumed to  $\sim 1$  mbar. The purpose of adding this vacuum line was to allow the recording of "vacuum spectra", or Raman spectra without any atmospheric gas signals. Then, this spectrum could be considered as a pure background to subtract from gas-Raman spectra. The background vacuum spectrum is shown in Figure 36.

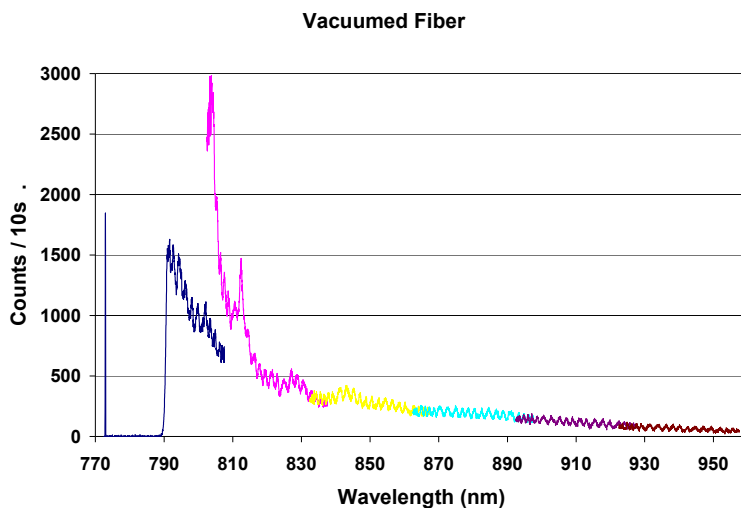


**Figure 36 – Vacuum spectrum**

Examination of the vacuum spectrum shown above reveals a silica-Raman signature which is similar in shape to previously obtained visible-wavelength silica spectra. Minor discontinuities in the spectrum are caused by varied responsivity over the detector area. These errors could be corrected by using known calibration lines and acquiring a “flat field” spectrum for responsivity equalization. Neglecting these corrections, spectra for pure gasses of interest were obtained. The vacuum spectrum in Figure 36 was subtracted from each gas spectrum as background noise. Figure 37 contains single gas spectra for methane, ethane, propane, nitrogen, and carbon dioxide. Peaks in the background noise level displayed are indicative of peaks in the silica Raman spectrum. Major vibrational Raman peaks are observable in each gas. Even nitrogen, whose  $2231\text{cm}^{-1}$  peak lies well outside the transmission band of the near-IR fiber, displayed a clearly observable peak. We noted that because the backscattering configuration was employed, the out-of-band nitrogen Raman peak appears reduced in size or cross section, rather than disappearing entirely. In fact, the loss in transmission at this wavelength results in what appears to be an interaction length that is shorter than the physical length of the fiber.

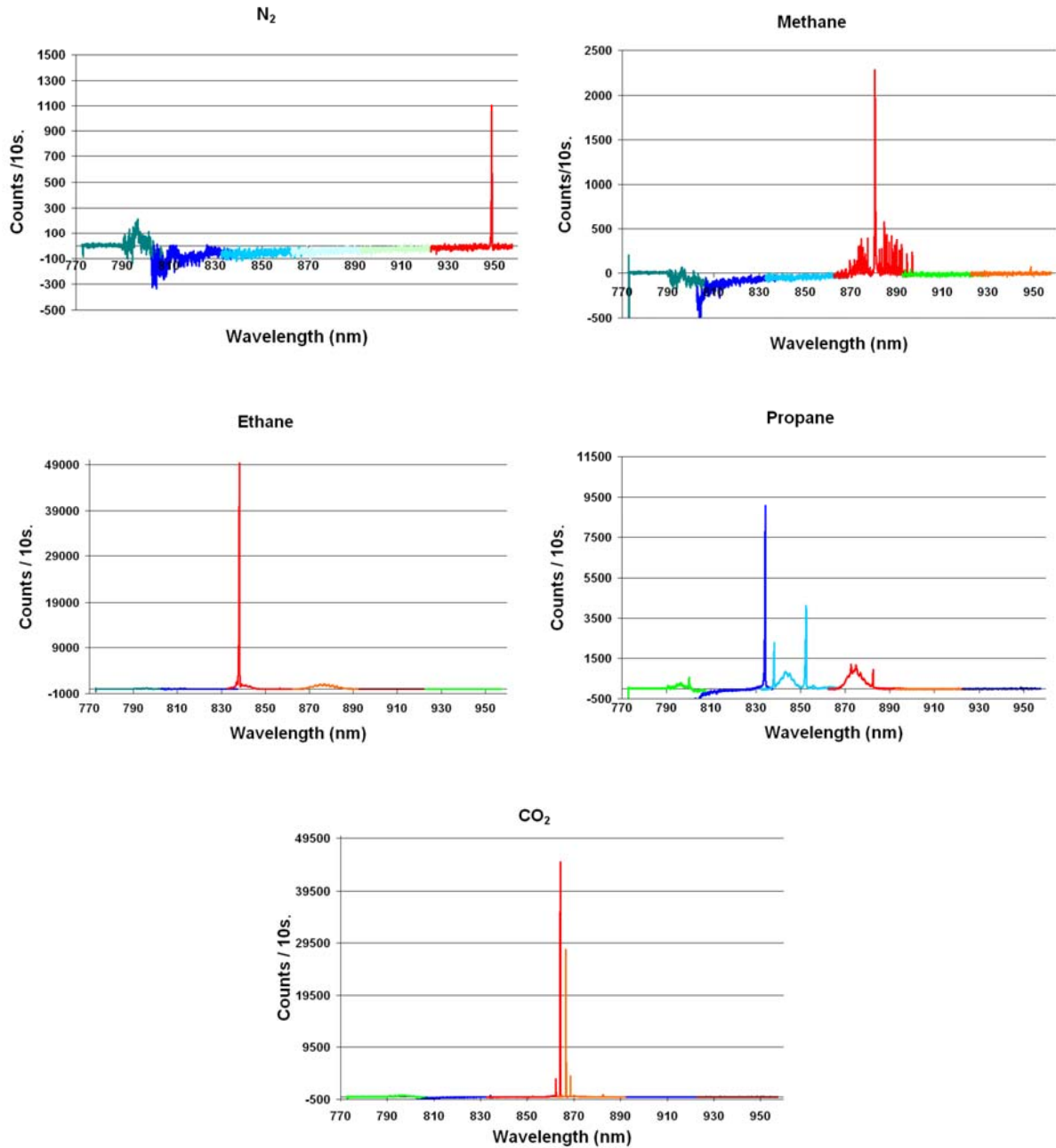


**Figure 37 – Single gas spectra (top left to bottom right): nitrogen, methane, ethane, propane, carbon dioxide**

Several important conclusions were drawn from these experiments in the near-IR. Firstly, it was qualitatively observed that gases transfer more quickly into and out of the HC-800 fiber than the HC-580 fiber. This is reasonable, given the larger core size in the longer-

wavelength fiber. Secondly, it was determined that images obtained using the 2D array detector could be analyzed to separate gas-Raman signals from silica Raman signals. Because these gas flow and signal-to-noise ratios are important sensor characteristics, silica Raman reduction and gas transfer characteristics will be presented separately in section 4.4 and chapter 5 respectively.

#### 4.4 SILICA RAMAN NOISE REDUCTION

Since the very first fiber-sensing experiments, we realized that silica-Raman would most likely provide the background level in PBF gas-Raman measurements [32, 35]. This is evident when we view a far-field diffraction pattern for any given HC-PBF. Figure 38 is a far field diffraction pattern for the HC-580 used in visible experiments. Note that this mode is not a perfect Gaussian spot, as is the case for other truly single mode systems. Although a core  $TEM_{00}$  Gaussian component exists and occupies most of the propagating power, there is a small non-Gaussian component also propagating in the cladding region. These additional higher-order modes are often called “surface modes” [39]. Crystal Fibre claims that more than 95% of the propagating light travels in air inside their fibers, and not in glass [41, 42]. The remaining 5% is actually propagating in solid silica. Even though only a small portion of our pump beam will travel in glass, the solid silica-Raman cross section is many times larger than most gas-Raman lines, so the silica Raman will dominate.

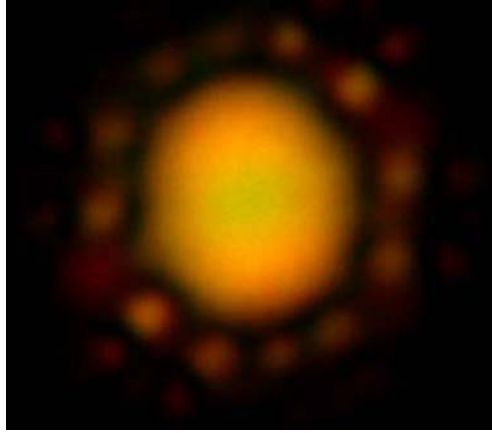


**Figure 38 - HC-580 mode field pattern [41]**

While conducting visible experiments, we noted that the majority of the signal generated by gases in the fiber core should be primarily  $TEM_{00}$ , and that light propagating outside the core should be of a higher-order nature. That implies that some degree of spatial-filtering could be used to eliminate out-of-core signal content. A spatial filtering apparatus was constructed to filter the visible-backscattered Raman beam using the experimental apparatus originally shown in Figure 27. The new setup is shown in Figure 39. The spatial filter was inserted in between the beamsplitter and the spectrometer's input lens. The filter consisted of an  $L_2 = 14$ -mm efl aspheric singlet and a pinhole. The combination of the 11-mm focal length lens ( $L_1$ ) and  $L_2$  formed a magnified image (magnification,  $M = 14/11 = 1.27$ ) of the fiber's output face located at an image plane approximately 14-mm from  $L_2$ . The pinhole allowed transmission of the near-Gaussian profile gas-Raman mode propagating in the fiber's core, while eliminating modal content from the silica Raman propagating outside the hollow core. The diameters of pinholes investigated experimentally ranged from 5- $\mu\text{m}$  to 20- $\mu\text{m}$ .

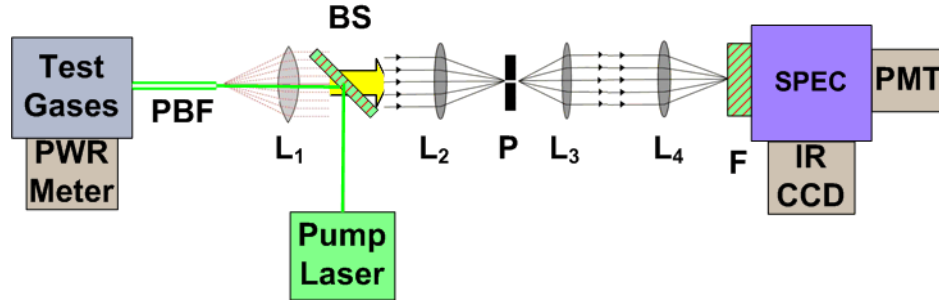


Figure 39 PBF spatial filtering experimental setup

Figure 40 shows spectra measured in the visible Raman system with and without a 10- $\mu\text{m}$  diameter pinhole. The spectrometer slits were 0.5-mm wide, yielding about 0.7-nm resolution. The nitrogen gas Raman signal was reduced by about only 6% with the addition of the 10- $\mu\text{m}$  pinhole. The silica Raman output, however, was reduced by at least two orders of magnitude over the entire band. It was also observed that pinholes smaller than 10- $\mu\text{m}$  reduce both the silica and gas-Raman signals. Pinholes larger than 10- $\mu\text{m}$  diameter resulted in a lesser reduction of silica Raman, with no effects on gas-Raman signals. These results are consistent with those expected from a magnified ( $M=1.27$ ) image of the Gaussian-like mode emerging from a fiber with a 4.9- $\mu\text{m}$  diameter core.

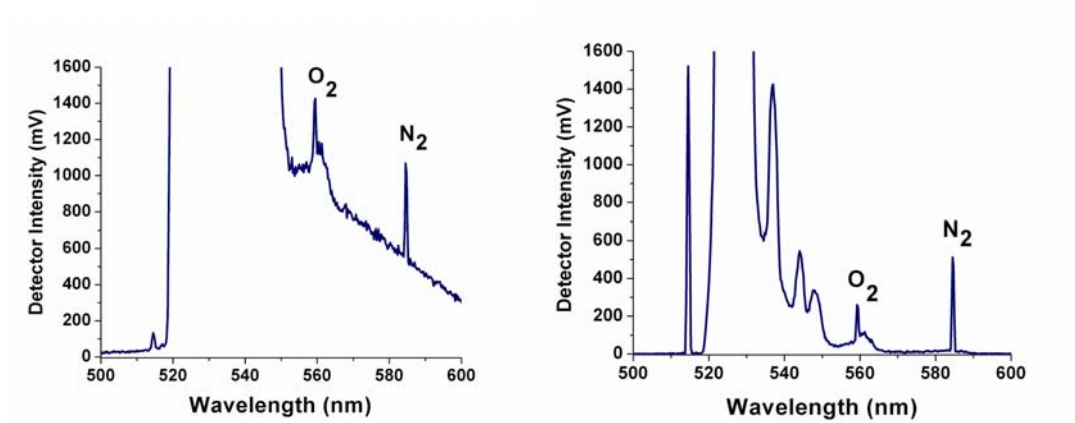


Figure 40 – Atmospheric Raman spectra; a) no spatial filtering b) 10 $\mu\text{m}$  spatial filter in the image plane

After determining the optimal size of the filtering pinhole, the signals and noise were measured with and without the spatial filter. The prominent Stokes nitrogen signal at  $2331\text{cm}^{-1}$  was used to establish detection limits. We will define a ratio (R) which is indicative of the minimum detectable concentrations of a species, and reminiscent of the signal-to-noise ratio (SNR). The ratio R was determined by dividing the height of the  $\text{N}_2$  Raman peak above background by the square root of the average magnitude of the silica Raman signal in the spectral region within 2-nm on either side of the peak. The ratio R (1 sec integration time) is then given by Equation 28, where  $C_{\text{N}_2}$  is the number photoelectrons/second at the 584.5nm nitrogen Raman wavelength above the background, and  $C_{\text{Si}}$  is the average number of background counts/ s detected in a 2-nm wavelength range on either side of the  $\text{N}_2$  peak.

**Equation 28:**  $R = C_{\text{N}_2} / \sqrt{C_{\text{Si}}}$

Equation 28 assumes that the background is Poisson distributed and can be subtracted out, but the fluctuation of the background signal remains as noise. R is then the same as the signal to noise ratio when the signal is small compared to the noise. Because the spontaneous gas-Raman scattering is also Poisson distributed, it will also exhibit variations (noise) proportional to the square root of the absolute signal magnitude. Therefore, as the signal gets larger, R is no longer a signal-to-noise ratio. The ratio R without the spatial filter is approximately 230. The use of a 10- $\mu\text{m}$  diameter pinhole increased R to more than 1380. To calculate the minimum detectable concentration of a species, we can measure R at a known concentration; in this case, the known concentration of nitrogen in the air. Then, the minimum detectable concentration is simply the known concentration divided by R. We calculate that our spatial filtering improvements should permit  $\text{N}_2$  detection ( $R = 1$ ) in a gas mixture at less than 565-ppm. The actual measurement time in each of these cases was less than 1 second. Because detector noise is about 2 orders of magnitude lower than the silica Raman signal, we estimate

that less than 0.1 second sampling time can be used without much reduction in SNR. Furthermore, we can also show that the time taken to introduce gasses into the fiber core is at least several times the sampling time at reasonable (<1000psi) input gas pressures.

The rudimentary spatial filtering technique described here serves as an enabling technology for gas-Raman sensors when applied to a PBF output mode-pattern as we have done. As we have shown, the simplest method for accomplishing such filtering is through the use of precision optical pinholes with diameters near the size of the fiber-core image. While undertaking near-IR sensor measurements, we discovered a new method of mode-filtration we describe as “digital spatial filtering”. In section 4.3, we denoted the importance of imaging the fiber’s output mode onto a 2D array detector. This is because we can actually use the digital output from the array’s vertical elements to filter a mode pattern. In our system, the horizontal dimension of the array detector is exposed to a wavelength-dispersed image of the fiber end-facet. In the vertical direction, the fiber core, cladding, and solid silica regions are clearly imaged and separated in space. The magnified images of the fiber’s core, cladding, and solid silica regions have diameters of approximately 51  $\mu\text{m}$ , 220  $\mu\text{m}$  and 743  $\mu\text{m}$ ; i.e., they extend over three, 10 and 31 array elements respectively. By simply adding the outputs of rows consisting of the “core image”, and discarding data from non-core pixels, we can filter the fiber’s output mode without actually using a pinhole. Although this technique only provides filtering in the vertical (non-dispersed) direction, the spectrometer’s input slits can be sized for spatial filtering in the other direction. This effectively provides a “square” spatial filter, which is slightly less effective than a true round pinhole. Fortunately, the technique lends itself well to miniaturization, given the reduction in number of optical elements, as well as ease of alignment.

The photo in Figure 41 shows a contrast-enhanced output from the 2-D array imaging an atmospheric pressure fiber. The center bright spot is due to Raman scattering from oxygen. The nearly evenly spaced vertical spectral lines (spacing  $\sim 1.0$ -nm) are the rotational structure of the Stokes' scattering [44]. The locations of the fiber core and cladding images are indicated. The broad spectral scattering observed in the photo is caused by Raman scattering in the silica located outside the core. The inset shows two spectral displays of the scattered light (ten second integration times) as functions of wavelength. The lower trace is a sum of the counts in the three central rows of pixels; i.e., the lower trace represents the total signal propagating in the fiber's core. The upper trace is a sum of the counts in the center 31 rows of pixels (the figure displays about 50 rows of pixels in the vertical direction); i.e., the total signal transmitted in the PBF core and cladding. For both displays, dark current has been subtracted. The ratio  $R$  (which is again similar to the SNR) indicated by the core signal and determined by Eq. 29 is approximately 500. The ratio  $R$  for the entire PBF signal (top trace in the inset) is significantly worse ( $\approx 275$ ) due to the summing of silica noise, as would occur in a single element detector system with no spatial filtering. The spectral resolution in Figure 41 is limited by the  $200\text{-}\mu\text{m}$  wide input slit width. The wide slit width was used for ease of alignment and to ensure imaging of most of the larger silica Raman content. The silica-Raman noise collected is expected to vary linearly with small changes in slit width owing to its continuous bandwidth.

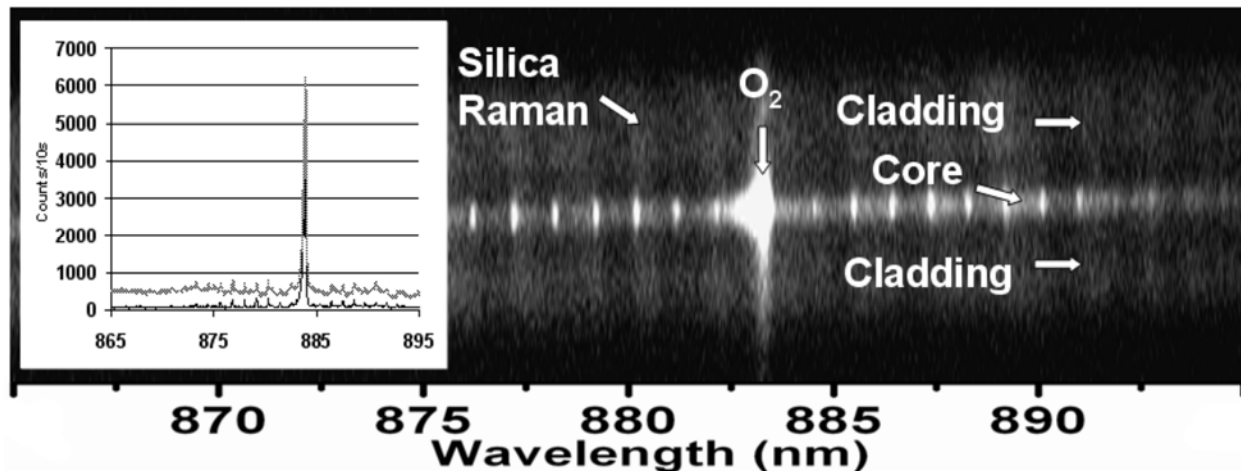
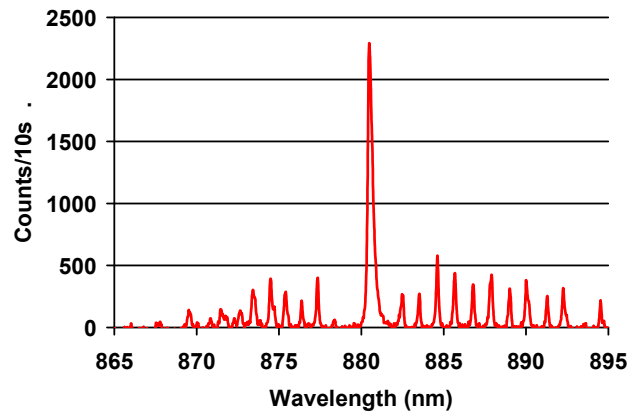


Figure 41 – 2D Raman scattering image in air

Both the traditional “pinhole” spatial filtering method and our suggested “digital” filtering method were evaluated using a number of different gases. Ultimately, the signal to noise ratios and consequent minimum detection limits are functions of the gas cross section and silica Raman background at the Stokes wavelength. Values for any gas exhibiting a Stokes shift in the transmission band of one of the fibers examined can be easily calculated using a known cross section and the data provided here. In general, all gases of interest were found to have detection limits in the low-ppm range using a <2m fiber, with higher cross-section gases and longer Stokes shifts falling on lower Silica backgrounds having the best detection limits. For instance, methane was effectively detected using our IR system to less than 165ppm. Figure 42 shows a representative spectrum about the Methane  $1532\text{cm}^{-1}$  line, in which rotational substructure is also clearly visible. We are confident that continuing advances in PBF design and manufacturing technologies will allow for lower attenuation and larger air-filling fractions, both of which will help improve SNR for gas detection.



**Figure 42 – Methane rotational Raman spectrum**

## **5.0 GAS FLOW AND DYNAMICS IN PBF**

In detailing the various sensing configurations explored for enhanced gas-Raman interactions, the difficulty in transferring gases for sensing was indicated. Currently, a great deal is known about gas flow in small capillary tubes. Existing knowledge on the matter of gas flow dynamics will be applied to our PBF sensing systems in order to estimate sensing times and to suggest methods for shortening the time required to produce subsequent concentration measurements.

In this chapter, we begin with a fundamental mathematical analysis of capillary gas flow, with respect to flow regimes encountered in our sensor systems. Then, we move on to experiments performed in determining sensing times. We will see that a number of improvements have been made and can continue being made to the analyte delivery and removal system in order to shorten sensing times and consequently allow near real-time sensing of various molecular gases. We will then use available data to suggest a probable path to real-time gas sensing.

### **5.1 PRINCIPLES OF CAPILLARY GAS FLOW**

The principles of gas or liquid flow in various conditional situations have been studied extensively. Determining flow characteristics inside a capillary tube or PBF core-hole is a simple exercise in fluid mechanics based on kinetic molecular principles. In general, our gas

sensing system will accept a fairly homogeneous gas mixture (at any instant in time), driven by a pressure gradient to flow from one end of the fiber to the other. The pressures, molecular diameters of contained gases, and their dynamic viscosities may all be obtained from relevant literature for precise calculation of flow rates [33-34].

In general, the flow of gas mixtures is governed by the Knudsen number:

**Equation 30:** 
$$K_n = \frac{\lambda_m}{d}$$

where  $\lambda_m$  is the mean free path between intermolecular collisions, and  $d$  is the capillary diameter. The Knudsen number is merely a dimensionless factor used to characterize the different statistical properties of flow governed by the collective effects of molecular collisions under a given set of conditions. A high Knudsen number ( $K_n \gg 1$ ) indicates a region of free molecular flow in which molecules mostly collide with the walls of the tube, and not each other. As  $K_n$  approaches 1.0, both intermolecular collisions and wall collisions play important roles in determining flow characteristics. This roughly defined region of operation is known as “slip” or “transitional” flow. Finally, small Knudsen numbers ( $K_n \ll 1$ ) describe the “hydrodynamic” or “Poiseuille” flow region. Therein, flux varies parabolically across the capillary, with flow approaching zero near the walls of the tube. The pressure or density remains constant over any tube cross section. Figure 43 pictorializes the different flow regimes.

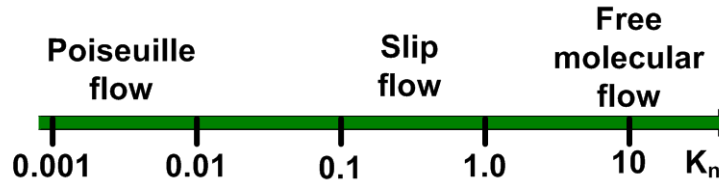


Figure 43 – Flow regimes and Knudsen Number [34]

Before enumerating the flow rate inside a capillary fiber, we will need to determine a Knudsen number for each particular case. The mean-free-path of a molecule can be estimated as:

$$\text{Equation 31: } \lambda_m = \frac{k_b T}{\sqrt{2} \cdot \pi \cdot d_{mol}^2 \cdot p}$$

where  $k_b$  is Boltzman's constant,  $T$  is the temperature (Kelvin),  $d_{mol}$  is the molecular diameter, and  $p$  is the pressure (Pascals). The Knudsen number is defined as:

$$\text{Equation 32: } K_n = \frac{\lambda_m}{d}$$

where  $d$  is the diameter of the capillary core hole. Combining Equation 31 and Equation 32 yields:

$$\text{Equation 33: } K_n = \frac{k_b T}{\sqrt{2} \cdot \pi \cdot d_{mol}^2 \cdot p \cdot d}$$

A more clear understanding of flow characteristics is gained by observing the various possible molecular diameters, tubing diameters, and pressure commonly utilized for our Raman experiments in PBF. Table 2 shows the mean diameters of various relevant molecules.

Table 2. Molecular Diameters [2]

<b>Molecule</b>	<b>Diameter (Å)</b>
He	2.28
H <sub>2</sub>	2.72
Ne	2.97
Ar	3.8
Kr	4.0
N <sub>2</sub>	4.1
O <sub>2</sub>	4.2
CH <sub>4</sub>	4.36
Xe	4.58
H <sub>2</sub> S	4.58
CO <sub>2</sub>	5.12
C <sub>2</sub> H <sub>6</sub>	5.5
c-C <sub>3</sub> H <sub>6</sub>	5.8
Trimethylene oxide, (CH <sub>2</sub> ) <sub>3</sub> O	6.1
C <sub>3</sub> H <sub>8</sub>	6.28
i-C <sub>4</sub> H <sub>10</sub>	6.5
n-C <sub>4</sub> H <sub>10</sub>	7.1

If we observe the various core diameters of HC-PBFs listed in Figure 7, we see that core sizes from ~4-15µm are common for fibers transmitting in the visible to near-IR ranges. These values indicate that pressures less than atmospheric generally produce free molecular or slip flow, while larger pressures tend towards Poiseuille flow. We will therefore concern our calculations primarily with Poiseuille flow characteristics as the most likely conditions occurring in our experimentation.

Poiseuille (or hydrodynamic) flow assumes a dynamic viscosity ( $\eta$ ) for the flowing gas, which is independent of pressure. The volume flow rate of the gas is then given by:

$$\text{Equation 34: } Q = \pi d^4 \cdot \frac{\Delta p}{128\eta L}$$

where  $d$  is again the tubing diameter, and  $\Delta p$  is the differential pressure across the tube of length  $L$ . Note that these equations assume a steady-state flow in the capillary; which has been allowed to establish non-changing pressures at all points in the system. In a steady state flowing system, we can make a general comparison of the capillary's inner volume ( $V$ ) and the time required to re-fill that inner volume with analyte gas. This “fill time” is then estimated as:

$$\text{Equation 35: } t_{fill} = \frac{V}{Q} = \frac{\pi d^2 L / 4}{\pi d^4 \Delta p / (128 \eta L)} = \frac{32 \eta L^2}{d^2 \Delta p}$$

Note that this “filling time” is proportional to the square of the capillary length, and inversely proportional to the square of the capillary diameter. Sensing times are therefore rather sensitive to both length and diameter of the PBF core in contrary fashions. Figure 44 shows estimated filling times for a number of different size capillaries with varying pressures. This graph indicates that filling times can be reduced to less than 1 second with a large enough, short enough capillary and a reasonably high input pressure. Obviously, shortening a fiber leads to a lower Raman interaction length, and utilizing a larger core diameter usually infers a longer wavelength transmission band, and therefore lower Raman conversion efficiency. This is the basis for trade-off between sensing speed and detection sensitivity.

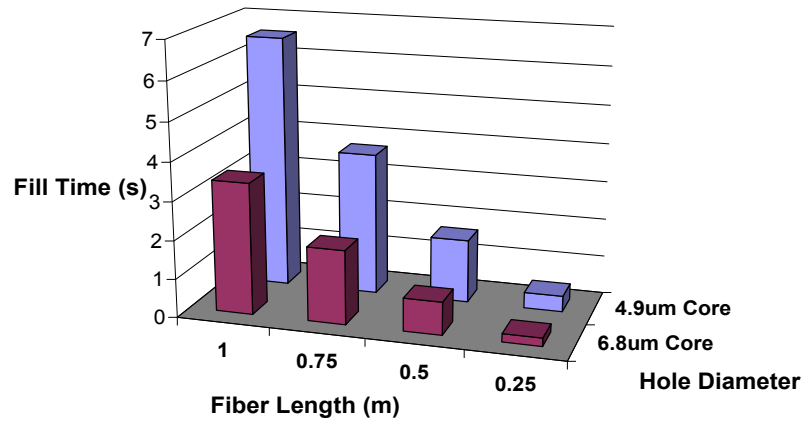


**Figure 44 – HC-PBF predicted filling times**

A somewhat more rigorous time-dependant derivation is often performed, resulting in pressures changing exponentially from a fixed-pressure starting point. In any case, we observe that exponential approach or decay to a final pressure is evident in time for either filling or venting situations. A normalized pressure and time relation is shown in Figure 45. The pressure is normalized with respect to the initial (venting) and steady-state (filling) pressures. The time is normalized by dividing real-time by  $\frac{32\eta L^2}{d^2 p_0}$  for plotting simplicity. In accordance with this

Figure, gas pressures will flow in our out of a capillary with the same properties being affected only by applied differential pressure.

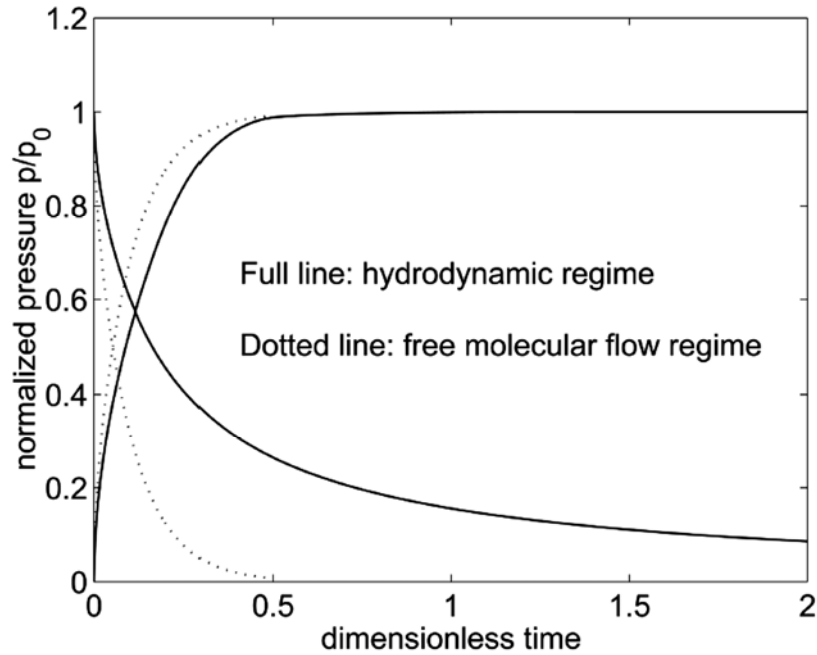
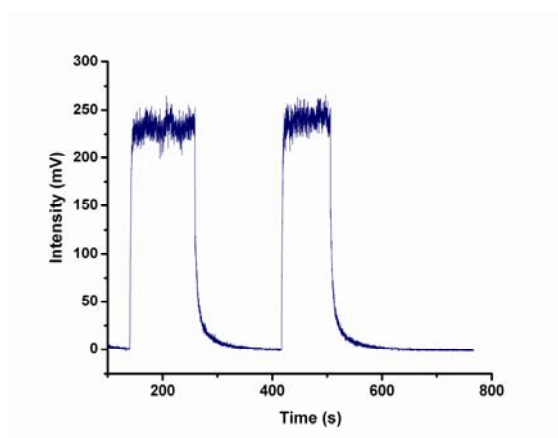


Figure 45 – Predicted time evolution of PBF pressure [34]

## 5.2 HC-PBF SENSOR RESPONSE TIME

In order to verify the gas-flow predictions made in 5.1, it was necessary to conduct evaluations of the Raman signal evolution in the various sensing configurations assembled. Initially, the visible wavelength backscattering system was used to observe gas-flux. The same experimental optical components were assembled as those shown in Figure 27. Therein, a 1-meter length of HC-580 was used as the gas cell. First, the fiber was vacuumed to remove any residual methane and draw in atmosphere from the open end of the fiber. Then a large manifold volume of pure methane gas was prepared to a 50psig overpressure. The Raman line at 2917cm<sup>-1</sup> was observed using the PMT (EMI 9789) for data recording. As a valve was opened and the 50psig methane sample was allowed to enter the PBF, signals were integrated for .1s and recorded sequentially. It was noted that due to readout time in the measurement system, every .1s sample actually took

.25s in real time. Subsequent sampled times were therefore multiplied by 2.5 in order to reflect actual time passed. After the Raman peak had reached more than 99% of its maximum value, the high-pressure methane supply was closed, and the vacuum line was opened, initiating evacuation of the fiber. Response of the Raman peak is recorded in Figure 46. Given the applied pressures at input and output, signal evolution appeared similar to previous predictions. It is interesting to observe that fill times are much shorter than evacuation times due to the limitation on differential pressure set by zero-vacuum pressure, or more realistically, the ultimate pressure of the vacuum pump used in the experiment. The maximum filling pressure is only governed by the mechanical burst pressure of the fiber. This is noted to be more than several thousand psi. Maximum differential *evacuation* pressure is initially the difference between the pressure in the filled fiber, and  $\sim$  zero. Furthermore, the decreasing differential pressure induced under vacuum pumping ensures that near the end of an evacuation cycle, the exiting gas-flow transitions from hydrodynamic to free molecular flow.



**Figure 46 – Raman peak response to gas flow**

In seeking ways to improve upon filling and evacuation times, a series of tests were devised intended to exploit increasing temperatures to reduce the dynamic viscosity of analyte gases. The length of HC-580 used in the previous experiment was placed into a bath of 50%

ethylene glycol and water. The temperature of the bath was controlled using a hotplate. Filling and evacuation times were observed with the same 50psig methane overpressure. They are plotted in Figure 47.

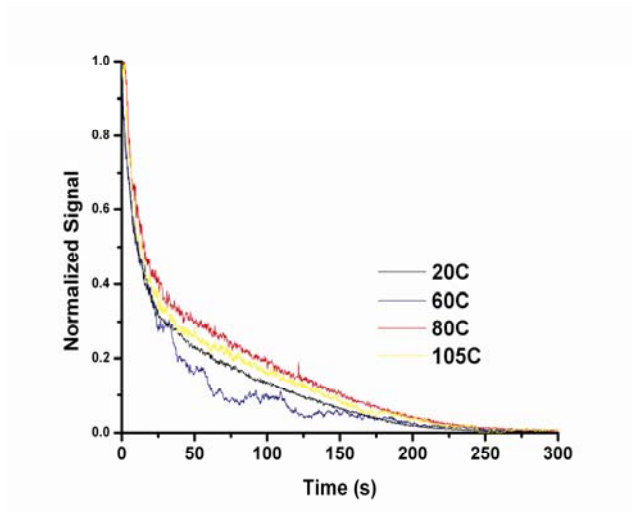
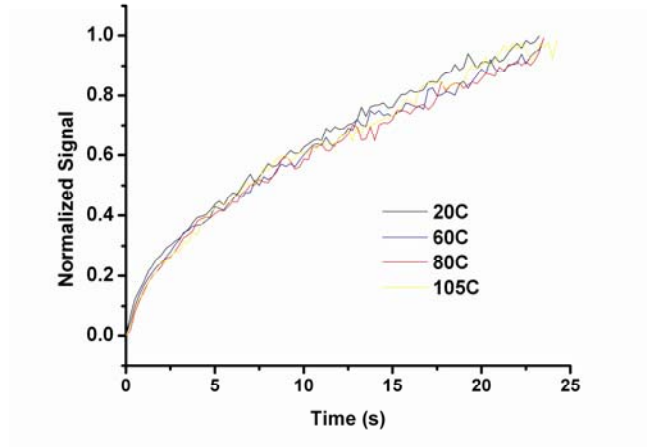


**Figure 47 – Methane Raman filling (top) /evacuation (bottom) times with changing temperature, HC-580**

It is important to note that the evacuation curves in Figure 47 do not completely follow one of the ideal curves shown in Figure 45. That is because the flow regime changes as the pressure in the fiber is decreased. As gases are removed from the pressurized fiber and the signal decreases, the curve starts to exhibit free-molecular flow characteristics.

Unfortunately, the maximum temperature increase for this experiment was 105°C. That is because degradation of the plastic fiber jacket can occur at as little as 120°C. In the interest of preserving sample fibers, higher temperatures were avoided. Although some minor changes in fill and evacuation times were noted, owing most likely to small changes in dynamic viscosity; time changes were too insignificant to draw any quantifiable conclusions. Presently, fiber jacketing systems are available for harsh environments which can be safely used under much higher temperatures (400°C or greater). The marginal changes noted here may warrant additional experimentation at much higher temperatures to shorten response times. In addition, the sampling of high-temperature gas streams may be possible simply by manufacturing PBFs with better jacket-coatings.

To verify gas-transfer speed improvements suspected when using larger core fiber, the near-IR backscattering experiment shown in Figure 32 was employed for time trials. While being pumped by a Ti:Sapphire laser at 780nm, the nitrogen line at 2231cm<sup>-1</sup> was observed with the application of 150psig input gas pressure. Filling and evacuation times are shown in Figure 48.

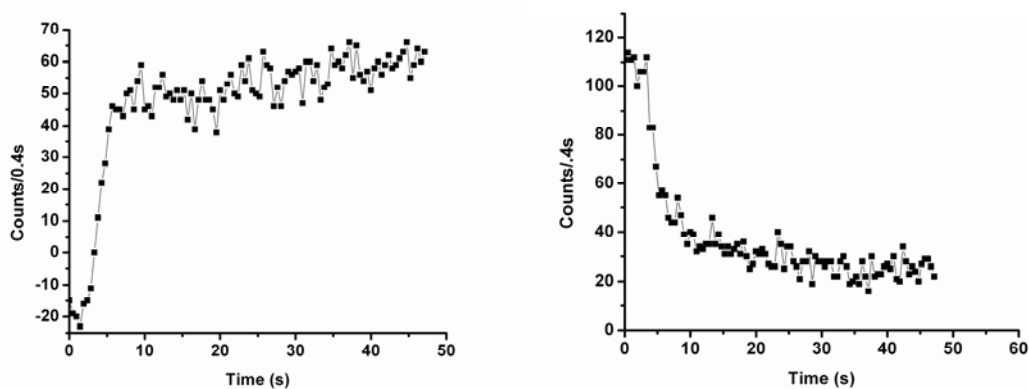


Figure 48 – Nitrogen filling/evacuation times, HC-800

As expected (given the difference in pressure), both signal rise and fall times are shortened due to the increased PBF core diameter in the near-IR experiment. The conclusion of this experiment highlighted the need for larger-diameter fibers, or possibly increased head-pressures in the quest for shortened sensing times.

## 6.0 MICRO-VOLUME GAS RAMAN

Thus far, we have gained a general understanding of the utility of photonic-bandgap fibers for use as scattered light collection devices. We have shown that gas-Raman spectra which traditionally would have taken extremely long to collect in free-space configurations are *optically* recordable in less than a second using our PBF system. While we have displayed both high signal-to-noise ratios and quick sampling integration times using PBFs, the true utility of such a system is realized when we consider real-world applications for a PBF gas sensor.

In characterizing the Raman response of our PBF sensor designs, we were mainly concerned with static spectra or the time-response of a single Raman line. None of these experiments directly measured the kinds of situations where a PBF gas sensor might operate in a continuously changing analyte stream. In this chapter we will suggest a real-world sensor application using a variant of our PBF sensor design. Herein, we will discuss the use of a PBF Raman gas sensor in a gas chromatography system. Such an application is well suited to the extremely small core-volumes of available PBFs, and provides an interesting alternative to traditional detection in chromatography.

Although we believe that using PBF Raman sensors in chromatography applications is quite a natural fit for this technology, there are several challenges to be overcome in the realization of a useful system. We will therefore begin by describing the proposed system with respect to common chromatography instrumentation, and later we will describe the necessary

developments to enable efficient operation and gas-flow in PBF, including the implementation of sample-injectors and PBF cladding fusion-seals.

## 6.1 GAS CHROMATOGRAPHY BACKGROUND

In researching other techniques for determining gas composition, we began to study gas-chromatography (GC) as a competing alternative to Raman spectroscopy. The principles of gas-chromatography are actually quite simple. Figure 49 shows the basic components of a chromatographic system. In such a system, an analyte gas is introduced into an injection port at the upstream-end of a long “column”, or capillary tube. The column is a length of small inner-diameter tubing of some sort which is usually lined with materials designed to adsorb sample gasses. The source-end of the column is supplied with a high-pressure “carrier-gas”, which flows down the length of the column towards the detector(s). When a sample gas mixture is injected into the column, it is forced by the high-pressure carrier to travel down the column towards the output as well. As the sample travels down the column, various molecular constituents in the sample begin to separate along the column length. Usually, the lighter and smaller molecules will travel the most quickly down the column length. At the end of the column, emerging analyte molecules are passed through a detector of some sort. Common types of detectors in gas chromatography include flame-ionization (FID) detectors and thermal conductivity detectors.

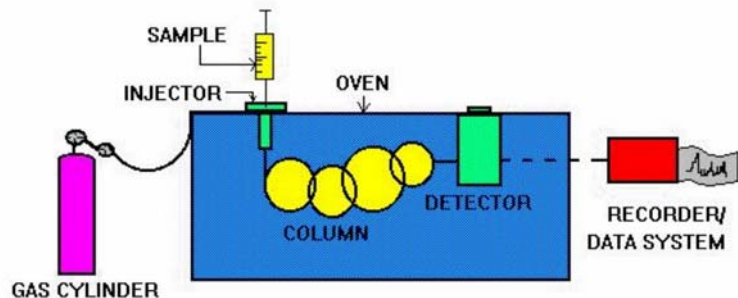


**Figure 49 - Common gas chromatography system components**

Chromatographic column designers can tailor the column packing materials and column geometry in order to ensure that different analyte gases of interest emerge with temporal separations that are large and easily measurable. In essence, the gas chromatography column separates components in both time and space. In most cases, a significant amount of a-priori knowledge is required to successfully operate a GC system. Researchers commonly use chromatography columns designed for a very specific gas mixture. By knowing the temporal response of a column to specific compounds, one can infer the presence of a particular analyte component simply because it elutes at a particular pre-determined time. Chromatography systems of this type often employ non-discriminatory detection. This means that the detectors used are often incapable of discrimination amongst different substances. For instance, a flame-ionization detector responds to the presence of flammable, ionizable molecules. It reports a signal proportional to the number of free valence electrons in an ionic flame. Obviously, this type of detector does not discriminate well between similar compounds, and does not respond at all to non-ionizable constituents. Figure 50 shows a typical sample GC response to natural gas detected using an FID. Note that the presence of C1-C6 hydrocarbons is indicated; although nitrogen, oxygen, or other inert constituents are not depicted. This is because these components are simply not measurable using this detection scheme. Furthermore, if details of the exact

column operating characteristics or elution times were not known, various resultant peaks could be easily mis-characterized.

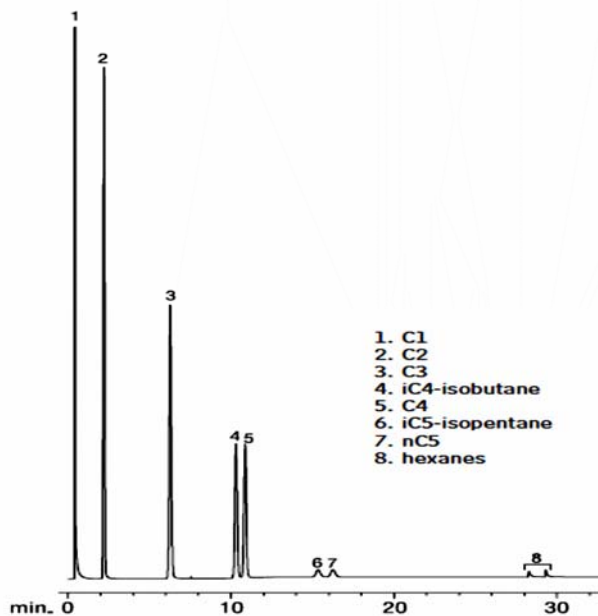


Figure 50 - Example GC trace from a natural gas mixture

In very broadly over-viewing GC principles, we begin to note some distinct problems with use of such a system, as well as some areas of overlapping utility with our Raman sensors. Firstly, we note that GC analysis commonly takes several minutes or even several hours to accomplish a complete separation of a complex mixture. Definitive characterization also requires some knowledge of the mixture's components and the elution times of those components in a particular chromatographic column. If our primary goal is to produce sensors capable of real-time burner or turbine control, we realize that GC systems are several orders of magnitude too slow for such operation. We have shown that PBF sensors are much faster than GC, but are still restrictive for real-time operation. This is why we have proposed the use of PBF Raman sensors as ideal *additions* to chromatography systems. In such an application, the Raman sensor could serve as a replacement-for or addition-to FID or conductivity detectors. Then, the

Raman sensor would add definitive characterization to the efficient GC temporal component separation.

## 6.2 THE HYBRID GC-RAMAN SYSTEM

Figure 51 is a diagram of our proposed hybrid GC-Raman system. The purpose of this system is to ‘marry’ the benefits of a gas chromatograph to the precise analysis provided by Raman spectroscopy. We should reiterate that the purpose of such a system is not ancillary to the goal of producing real-time natural gas sensors. This technique is intended to provide an alternative method for the accurate analysis of gas mixtures in other scientific applications. We will detail the proposed design carefully, along with the specific details of its operation.

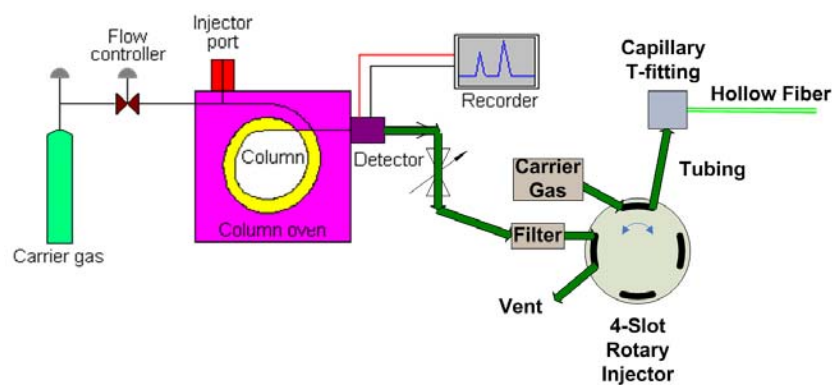


**Figure 51 - Diagram of proposed GC Raman hybrid system**

In the proposed GC system, the traditional GC carrier gas stream and column are retained. In some cases, it may be advantageous to retain the usual GC detectors, provided that they are not destructive to all of the analyte; given that the analyte will be needed in the downstream Raman detector. The hollow fiber and optical components detailed in previous Chapters (such as in Figure 39) are employed here as an additional detection setup, although only

the hollow-waveguide portion of the Raman detector is shown in the layout diagram in Figure 51. An additional gas-injector is shown therein which provides the Raman sensor with analyte.

During operation of the proposed GC Raman system, a sample is injected upstream of the column as would occur in a regular chromatography system. The sample travels through the column at the application of high-pressure inert carrier gas. The analyte can then be passed through a non-discriminatory detector as it would be in a system without Raman capabilities. Finally, the output analyte stream is passed through a micro-volume sample injector. This is a device commonly used in the upstream of the GC system for injecting samples into a column. Essentially, the sample injector is comprised of a small rotor onto which are scribed precisely sized slots; which are designed to be filled with a tiny measured volume of sample. When the rotor is rotated from the “sampling” position to the “injection” position, the contents of a single measured rotor-slot are inserted into the measurement loop and forced through the system by the carrier gas.

In our hybrid GC/Raman system, the waste output from the GC column is fed through the sampling loop of a downstream sample injection rotor. Each time the upstream GC-detector peaks, the presence of an eluting compound is recognized, and the sample injector is triggered to send a micro-volume sample of the eluting analyte into the Raman detector. Because the volumes of available PBF waveguides are extremely small, it is relatively easy to fill the waveguide with a plug of eluting gas. In this manner, the chromatography column performs the work of separating and concentrating sample components for delivery to the Raman sensor. This has the effect of increasing the SNR for a particular compound, and eliminating any significant overlap between Raman spectra of different compounds. The addition of Raman sensing capabilities to the system allows the identification and discrimination of otherwise difficult-to-

distinguish components and un-reactive elements. Together, they form a much more robust and utilitarian instrument.

### 6.3 GC RAMAN SENSOR EXPERIMENTS

An experimental Raman sensor for use with GC systems was constructed to test the various response characteristics related to use of a PBF in this particular situation. Figure 52 details the components in the system. It is important to note that an actual GC column was not used for these initial tests. That is because we wish to review the characteristics of the carrier-gas driven Raman sensor without the added effects of any number of different upstream GC columns. In future experiments, it will be necessary to characterize the operation of an entire GC/Raman system including various columns; albeit somewhat beyond the scope of this dissertation.

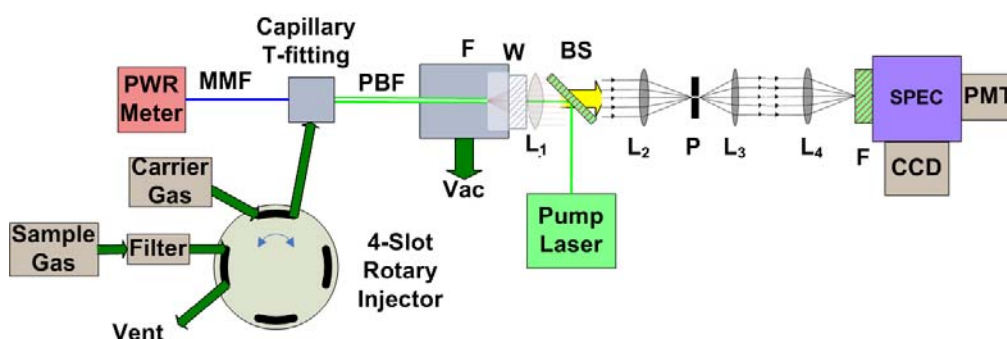


Figure 52 - Experimental Raman GC sensor components

The sensor conceptualized in Figure 52 includes several of the necessary Raman components described in previous Chapters. Specifically, the backscattering configuration is utilized with pinhole spatial filtering for silica-Raman noise reduction. The windowed flange (W) shown provides a means of holding the fiber output at low-pressure while maintaining high

coupling efficiency. Again, pump throughput is measured via a multimode fiber-coupled power meter, and scattered output light is filtered with both a dichroic beamsplitter (BS), and a long-wave pass Raman filter (F). The sample injection rotor used here contains slot volumes of .06, .1, .2, and .5  $\mu\text{L}$ . While it should be noted that only one sample slot volume is used at a time for injection, the multi-slot rotor provides for different experimental injection volumes. The particulate filter in the sample stream is a 0.5 $\mu\text{m}$  frit filter capable of withstanding high sample pressures. Obviously, because of the extremely small sample volumes present, it is necessary to maintain high-sample purity in eliminating particulates and contaminants from the sample stream. Ultra-high purity helium, nitrogen, and argon were provided as possible carrier gases for testing. Finally, the PBFs incorporated in these experiments were treated with an additional step designed to maintain cladding integrity during repeated repressurization. Therein, the cladding holes at the gas-injection end of the fiber were sealed to prevent gases and contaminants from contaminating the cladding. This technique in and of itself is unique, and will be discussed in detail in Section 6.4.

The experimental Raman/GC detector was operated using a number of different carrier gasses, sample gasses, and rotor volumes. A 2-meter length of HC-800 fiber was used as the Raman waveguide. Pumping was performed using  $\sim 30\text{mW}$  of Ti:sapphire laser power at 780nm. As an initial system test, .06 $\mu\text{L}$  of  $\text{CO}_2$  at 150psi was injected through the sample stream while Helium carrier gas was supplied at 500psi and  $\sim 1\text{mtorr}$  vacuum was applied at the output. Several pixel rows from the CCD array output were summed and recorded as a single-element spectrum with no spatial data. This method was employed because of the quick readout time realized when only reading out a 1024X1 pixel matrix instead of a 1024X256 element pixel matrix from the array. Spectra were recorded in this manner every 0.5 seconds.  $\text{CO}_2$  Raman

lines at  $1388\text{cm}^{-1}$  and  $1409\text{cm}^{-1}$  were recorded simultaneously in each spectrum. While recording subsequent spectra each half-second, the injection rotor was actuated sending sample  $\text{CO}_2$  into the Raman sensor. Figure 53 shows the resultant time-spectra.

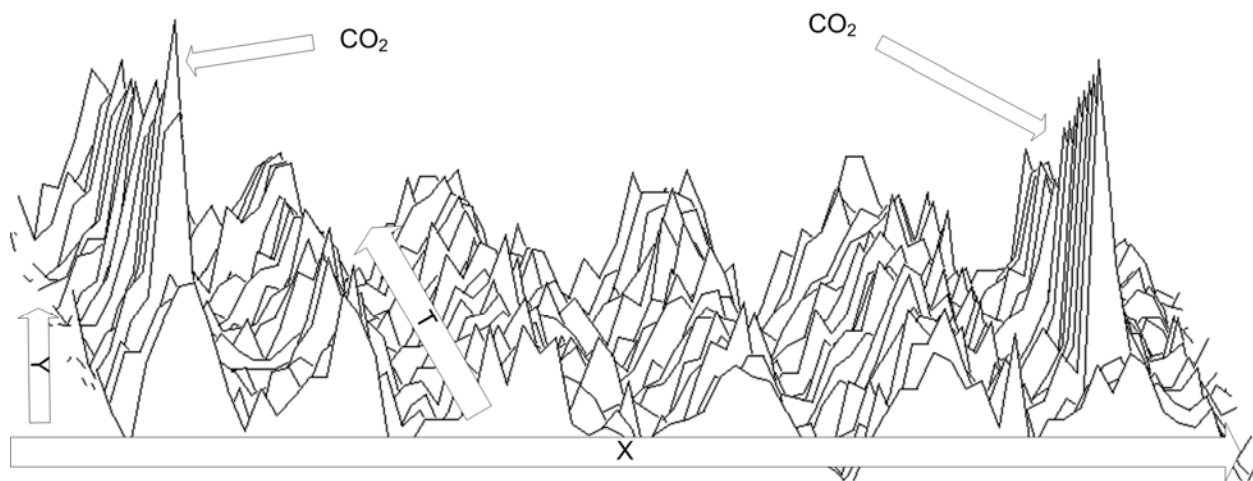


**Figure 53 -GC Raman spectral/time response to applied  $\text{CO}_2$**

Figure 53 displays several important characteristics indicating the functionality of the GC Raman sensor. The X-axis in this figure represents wavelength. A  $\sim 12\text{nm}$  wide spectrum is shown in this pictorial figure which is centered around  $870\text{nm}$ . The Y-axis indicates the intensity or number of signal counts per pixel detected by the array. The T-axis (time) in this case shows a total time passage of about 5 minutes. The central peaks in the image are the two prominent  $\text{CO}_2$  lines. They are noted to appear abruptly several seconds after the  $0.06\mu\text{L}$  injector is actuated. In a few minutes, the Raman lines decay to baseline values. Non-changing background peaks in the Figure are again due to silica Raman noise. From a systems perspective, we can see that the recording of such a time series of spectra allows exact determination of which compound is eluding from the GC column, and at what time it is emerging. After this initial functionality was verified, detailed operational analysis was performed.

Figure 54 shows the effect that different injected volumes have on the time-dependant Raman signal. Here again, CO<sub>2</sub> is injected into the Raman sensor at 150psi with a 500psi helium carrier. The 1388cm<sup>-1</sup> CO<sub>2</sub> Raman line was observed and recorded with a 0.5 second integration time. Overall, results proved quite interesting. The Raman line is observable several seconds after injection. Note that the larger the rotor volume employed, the larger the absolute magnitude of the Raman signal. The time response of the sensor in this case is a result of the pressures employed and the geometry of the fiber, and not of the rotor volume.

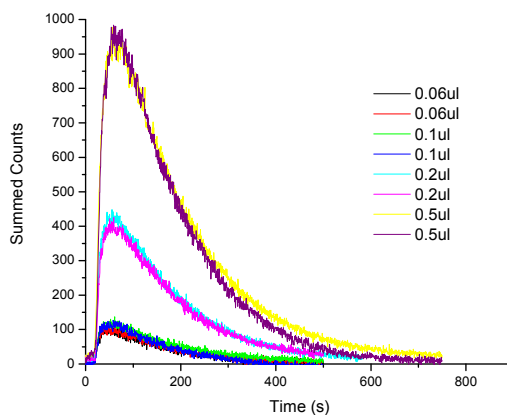


**Figure 54 - CO<sub>2</sub> Raman line time-response for various injector volumes**

A more thorough analysis of the fluid dynamics of the GC Raman system reveals the nature of the varying magnitude responses with varying injection rotor volumes. Figure 55 is a normalized version of Figure 54 in which each plot is multiplied by a constant to normalize the peak absolute magnitude to 1.0. We can easily see that there are two time constants which characterize the Raman response. A very fast time constant (seconds) governs the hydrodynamic input flow where analyte is forced through the waveguide following Poiseuille relations, as described in Chapter 5. After the analyte has passed down the length of the fiber and has occupied the largest available optical interaction length, it begins to diffuse into the helium carrier, and exits the fiber as a diluted mixture. The time constant governing the fall-time of the

Raman signal is therefore on the order of hundreds of seconds. This fall-time increases slightly if the fiber output is maintained at ambient pressure, although retention times can be far longer if the unsealed fiber-output end is pressurized with sample gasses.

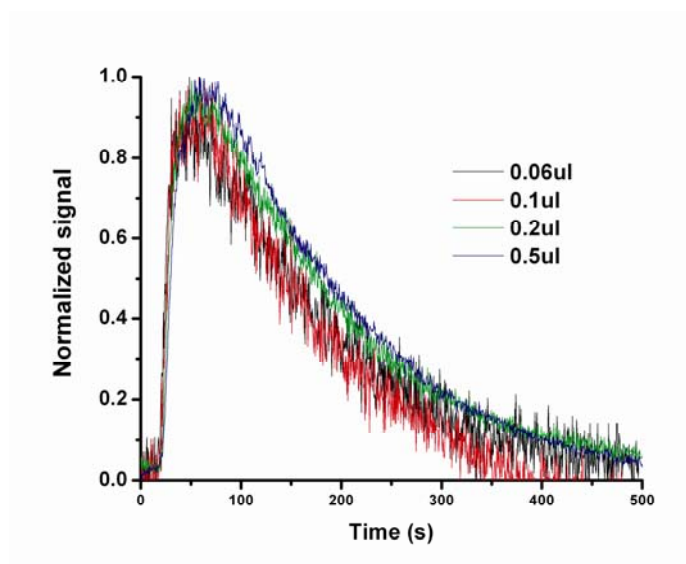


**Figure 55 - Normalized Raman GC sensor response**

Figure 56 provides a better picture of the reason for variation in magnitude response in the GC Raman sensor by enumerating the various volumes associated with system components. Firstly, we note that there is a significant “dead-volume” upstream of the PBF waveguide in both the gas-delivery tubing and the capillary t-fitting used to couple the fiber to the gas supply. Secondly, we note that the volume of the hollow PBF waveguide itself is slightly larger than the smallest injector rotor utilized. This gives us clues about the nature of the resultant Raman time-spectra. We can easily characterize the delay time between injection and the rising edge of the Raman signal as being due to this upstream dead-volume. We further note that reduction of this dead volume is possible if custom gas-transfer components were designed and fabricated. Given this dead-volume and the small waveguide volume, we also note that significant upstream mixing of the analyte and carrier gasses will result in long-tailed decays as observed in the time-spectra. Increases in rotor volume in the presence of such dead-volume will increase the

concentration of analyte in the downstream mixture, rather than increasing the amount of time over which a Raman peak will appear. These effects should be minimizable if the upstream volume can be reduced.

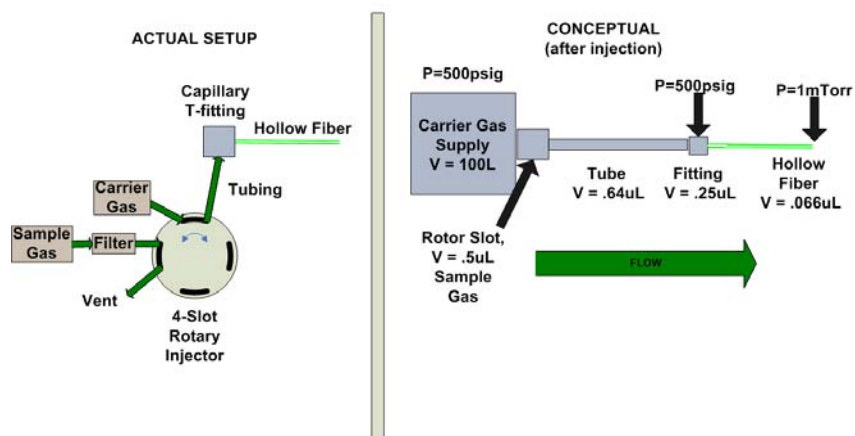


**Figure 56 - Raman GC sensor system flow diagram with component volumes**

A variety of different analytes and carrier gases were next injected into the Raman sampling system to determine system responses to various species. Figure 57 shows the time response of a 0.5uL injection of either CO<sub>2</sub> or Ethane gas with a 500psi Nitrogen carrier. In this experiment, we note that the peak magnitudes correspond roughly to the Raman cross sections of the two lines, with the CO<sub>2</sub> 1388cm<sup>-1</sup> line exhibiting the larger signal peak. The time constants for both gases are almost exactly alike, indicating the relative time-indifference to various species passing through the comparatively short sensing-waveguide.

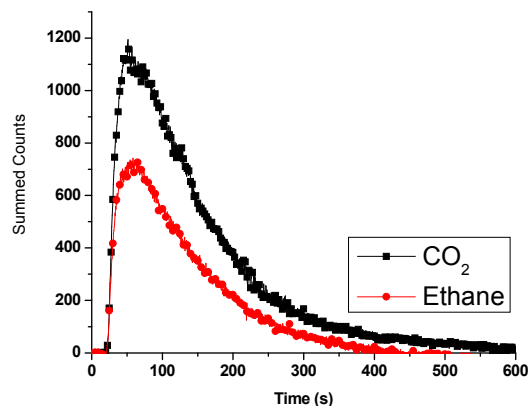


**Figure 57 - CO<sub>2</sub> and Ethane time response in the GC/Raman sensor**

To get an idea of the effects that different carrier gases have upon system timing, both high-purity nitrogen and helium were tested as carriers. Figure 58 shows the peak-normalized time response of the CO<sub>2</sub> 1388cm<sup>-1</sup> line while driven with either helium or nitrogen carrier gasses at 500psi. In GC systems, lighter carrier gasses are generally preferred because of the faster response times associated with the lighter gasses, which travel faster than heavier analytes. Similar results are noted in our Raman GC sensor setup. The helium carrier ultimately provided faster rise and fall times, undoubtedly owing to the effects of the lighter carrier gas enabling faster transfer. Although this effect was observable, it is purported to exhibit time effects which are minimal compared to total overall transfer time.

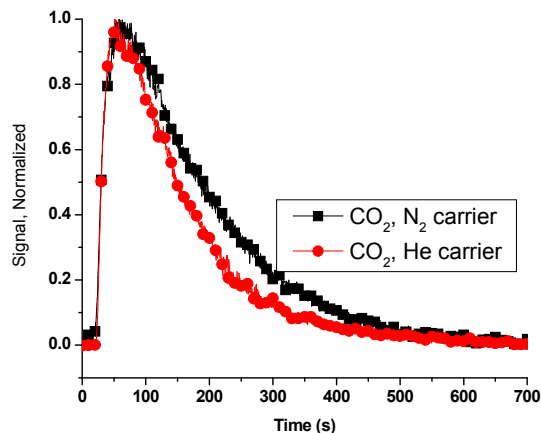


**Figure 58 - GC/Raman sensor response with He and N<sub>2</sub> carrier gasses**

In previous experiments, significantly shorter falling-edge time constants were reported in the case where both ends of the PBF waveguide were vacuumed instead of applying single-ended vacuum and pressurized injection as shown in Figure 56. Figure 59 is a direct comparison of those two situations. In the Figure 59 (a), the Raman signal rise time for CO<sub>2</sub> gas at 150psi is shown to be approximately the same regardless of whether bulk gas is supplied to the fiber input or a metered micro-volume sample is injected at similar pressure. This is true whenever the injected volume is smaller than the fiber inner volume. As shown in Figure 59 (b), the overall evacuation time is significantly shorter when ubiquitously vacuuming both ends of the fiber instead of waiting for carrier gas flow to clear the injected sample. This information could lead to the implementation of alternative methods of gas removal after sampling including vacuuming of injected samples after a signal peak has emerged.

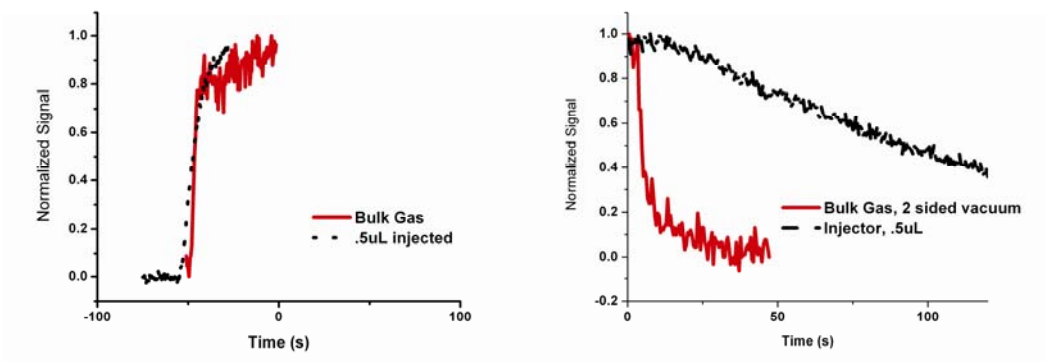


Figure 59 - Micro-injection and bulk gas transfer speed comparison

## 6.4 CLADDING SEALS AND CONTAMINATION

Previously, some discussion was presented on the propensity of PBFs to become clogged or else exhibit degraded optical transmission properties after being pressurized with particle-laden sample gases. Since our first experiments with forward scattered butt-coupled fiber gas cells, we have recognized the importance of ensuring that small solid particles do not become trapped inside a PBF cell. Such contamination is indeed capable of reducing optical transmission; or given the high power densities in a PBF core, even destroying a length of fiber entirely. This is why we have pioneered some interesting techniques designed to preserve a PBF gas cell under continuous pressurization and gas flow. These techniques, which include the use of common high-efficiency filters along with a novel fusion-splicing technique, have allowed the continuous use of a PBF gas cell without observable degradation for several weeks or months.

Our initial attempts at fiber contamination protection consisted of incorporating standard gas-stream particulate filters upstream of the PBF gas cell. It was qualitatively noted that 0.5 $\mu$ m pore-size scintered stainless steel filters do a relatively adequate job of protecting PBFs in most

cases. These filters are extremely robust, and can withstand several thousands of psi overpressure while eliminating all particles with diameters larger than  $0.5\mu\text{m}$ . If we once again review Figure 3, we note that the core holes in each of the hollow-core PBFs used in these experiments are all larger than  $\sim 5\mu\text{m}$  or so. Ensuring that particles up to an order of magnitude smaller than the core diameter are excluded should theoretically provide a significant level of contamination protection. Unfortunately, we also note that the sizes of cladding holes in the surrounding bandgap structure are usually smaller than  $1\mu\text{m}$  in diameter. This means that although commonly available particulate filters can be used to effectively prevent contaminants from entering PBF cores, little can be done to protect the cladding structure from contamination. This is why we pursued a new technique for sealing off a PBF cladding structure without damaging the optical properties of the fiber.

Researchers intent on using PBF in integrated optical equipment have developed techniques for splicing or joining lengths of PBF to standard solid-core fibers, or of sealing the ends of PBFs after pressurization with gases to form fixed-pressure gas cells [77]. We have adapted the previously demonstrated fusion-splicing technique to allow the selective sealing of PBF cladding holes without sealing the core. Figure 60 (a) is an SEM micrograph taken of a length of HC-580 fiber. Note that the core hole is about  $\sim 5\mu\text{m}$  in diameter while the cladding holes are much smaller than  $1\mu\text{m}$  in diameter. Our experimental technique for PBF gas cell preparation was accomplished as follows. First, the fiber was stripped, cleaned sparingly with ethanol, and cleaved flat. Then, the cleaved fiber-end is loaded into a fusion splicer (Ericsson FSU995FA) with an adjustable fusing duration and current. The fusion-arc is then applied for a fixed duration spanning several milli-seconds with minimal arc-current. The fiber end-facet was then viewed under an SEM to determine the degree of fiber melting that had occurred. The

fusing was then repeated with increasing arc-currents until visual confirmation could be made that the cladding was sealed by surface tension, while the larger core hole remained unsealed. This sort of trial and error process was initially extremely tedious, but once a set of fusing parameters had been obtained, PBFs of the same type could be repeatedly and similarly fused. Figure 60 (a) is an SEM micrograph of the cleaved end facet of a length of HC-580 PBF. Part (b) of the figure is a close-up of the same fiber end after the application of fusing current insufficient to seal the cladding holes. Therein, the cladding appears to have sagged slightly and become distorted due to the fusing heat, but without complete melting and re-solidification. Part (c) of the figure is another full-scale micrograph of the same fiber after sufficient fusion splicing heat had been applied. Note the complete absence of cladding holes, and the clear central remaining core hole.

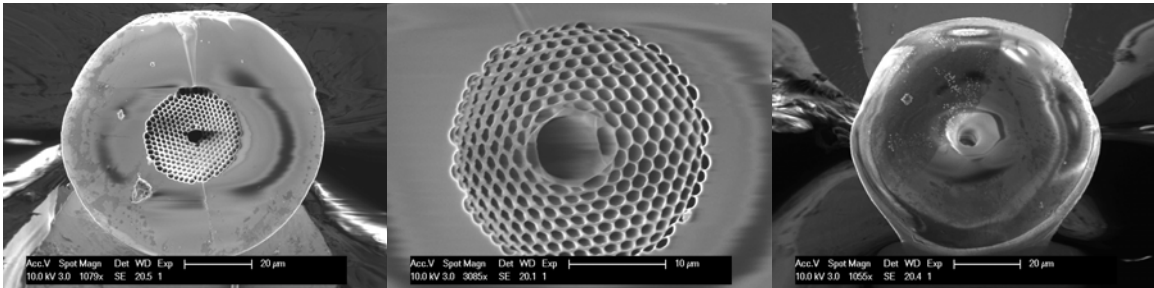


**Figure 60 - SEM micrograph of fusion-sealed PBF**

After successfully sealing lengths of HC-580 and HC-800 PBF, the general characteristics of the sealed fibers were reviewed. Firstly, it was noted that while pump coupling efficiencies were still relatively high (greater than 30%) when coupling to the unsealed fiber end, they were generally not as high as when coupling to the sealed fiber end. The reasoning behind this concept is obvious given the nature of the fiber's bandgap structure. By melting closed the end of the cladding, the radial bandgap that induces transmission in the fiber is removed altogether, resulting in high losses at the fiber end-facet, and significant pump coupling into the

solid glass surrounding the cladding structure by total internal reflection. In our proposed backscattering collection arrangement, this poses no difficulty because gases can be introduced into the fiber at the fused end while pump coupling and Raman collection can occur at the other cleaved (un-fused) end of the PBF; which can be held under vacuum. We have observed a single length of cladding-sealed HC-800 fiber over a period of several weeks during which several hundred bulk-gas pressurizations and depressurizations occurred. No noticeable reduction in transmission occurred over this time, indicating the general viability of the technique. More importantly, while testing the GC-Raman sensor described in this Chapter, (which included a cladding fusion-seal) no degradation in transmission was noted after several hundred sequential injections. Although such tests were not carried out to date, it would still be beneficial to carry out significantly longer and more rigorous lifetime tests to ensure the long-term viability of PBF sensors.

One additional benefit of the PBF cladding-fusion splicing process was discovered. It had been previously noted in Section 4.2 that gases introduced into a length of PBF would exhibit Raman signals long after the gas source had been removed. This was assumed to be due to gas molecules trapped inside the cladding structure or diffused into the silica glass itself. We have determined that such gas-trapping is not evident after fusion splicing. Although ambient pressure diffusion rates remain low even in the large PBF cores, sealing the cladding structure to prevent the infusion of gasses drastically shortens the retention time inside the PBF waveguide. Given the relative internal dimensions of the cladding holes being sealed, it is only logical that their particle retention characteristics play the dominant role in the persistence of Raman signals. Although we will not present quantified results of these effects because of the long-duration of necessary retention testing, we believe that our cladding-fusion technique ensures that flow or

diffusion characteristics of gasses in a fused fiber will closely follow the characteristics of gasses in a single-hole capillary with diameter equal to that of the PBF core-hole. Therefore, cladding fusion can be used to mitigate the tendency of micro-structured PBF to retain gasses.

## 7.0 METAL LINED CAPILLARY WAVEGUIDE THEORY

Thus far, we have been primarily concerned with the collection of Raman scattering from inside single-mode waveguides like hollow core photonic bandgap fibers. As was previously noted, there are a myriad of different types of waveguides that could be used in a similar manner to collect Stokes emissions from an increased interaction volume. Such a waveguide should ideally meet a number of criteria in order to provide such utility. We will briefly re-summarize those characteristics here with respect to common waveguide parameters.

An effective gas-Raman collection waveguide must first be capable of operating with very small propagation losses for the Stokes photons of interest. While the pump wavelength must also propagate with relatively low loss, it is more important that the scattered Stokes photons be collected and propagated with low loss in the forward-scattering configuration. (In the backward scattering case, loss at either wavelength is equally important.) This dependence is readily apparent when we re-examine Equation 12 and Equation 14. Ideally, low losses should exist for both pump and Stokes beams, resulting in overall efficient collection. As we have observed, the spectral separation (between  $\sim 200\text{cm}^{-1}$  and  $4000\text{cm}^{-1}$  for various species) between pump and Stokes photons necessitates a collection waveguide with an extremely large spectral transmission range.

Waveguides with large spectral transmission windows are indeed difficult to manufacture. Figure 7 detailed the transmission windows of several commercially-available HC-

PBFs. Generally speaking, transmission windows for HC-PBFs designed for the UV to IR range can possess clear transmission bandgaps as wide as two or three hundred nanometers. Production of wider bandgaps while maintaining low transmission losses has not been achieved to date. Fortunately, other types of hollow waveguides do exist which meet spectral and propagation loss specifications for our proposed Raman system. Reflective metal waveguides have emerged as robust and inexpensive alternatives to TIR fiber waveguides and PBFs. Although these sorts of guides have been studied for a long time, only recently have reflective waveguides of suitable quality become available for this application [68-71]. Furthermore, these metal-lined reflective capillary waveguides have large inner diameters which can support higher flow rates than any of the PBFs discussed here.

## 7.1 MULTIMODE WAVEGUIDE COLLECTION

Previously, spectroscopists attempted to increase the amount of scattered light collected from fluorescing or Raman-emitting samples by using bare-glass capillary tubing [17]. It was noted that a bare hollow glass tube could serve as a low-loss waveguide for a few low order modes. Figure 61 shows the transverse mode profile of the  $EH_{11}$  mode. This mode has been studied extensively in the past, and it has been determined that by launching a pump beam into a hollow glass capillary tube at a very shallow angle, the pump will couple into this waveguide mode efficiently, and propagate with low loss. Consequently, if the hollow bare capillary tube also contains Raman-active media, omni-directional Raman scattering will occur. Raman photons that are emitted at similar shallow incident angles will also propagate as a low-loss hybrid  $EH_{11}$  mode down the length of the capillary tube. Because this relatively low-loss mode exists and

propagates efficiently in a bare capillary tube, it is possible to collect a larger Raman signal using a bare capillary tube than by simply using free-space optics. Raman signal enhancements are generally noted to be in the range of 30-50 times larger than free-space collected signals [17].

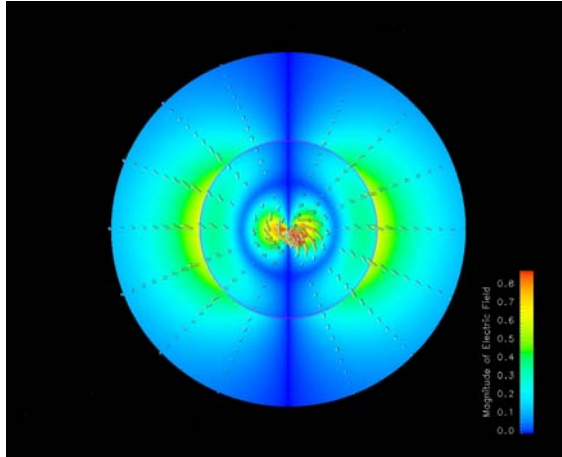


**Figure 61 - Magnitude of the transverse electric field of the  $EH_{11}$  mode in a dielectric waveguide**

The realization that hollow capillary tubing can efficiently collect scattered light spurred further collection waveguide developments. Although researchers have long theorized Bragg reflector and other multilayer types of waveguides, the most easily producible waveguide has been shown to be the single-metal lined variety. By simply coating the inside bore of a length of glass capillary tubing with a reflective metal, it is possible to create a waveguide of extremely high quality with a very large spectral transmission range. The reflectivity of metals is well known and easily calculable given the complex index of refraction of the metal and the surrounding medium (usually air). Figure 62 plots the reflectivity at normal incidence of silver, aluminum, and gold in the visible range. Because these reflectivities all exceed  $\sim 90\%$  at some wavelength, each is a good choice for mirror-coatings near the reflectivity peak. Because of the location of these peaks, each is used for a slightly different wavelength region of interest in standard mirror coatings. Ultimately, effective mirrors can be produced from each metal if considerations are given to surface smoothness, oxidation properties, and incident wavelength.

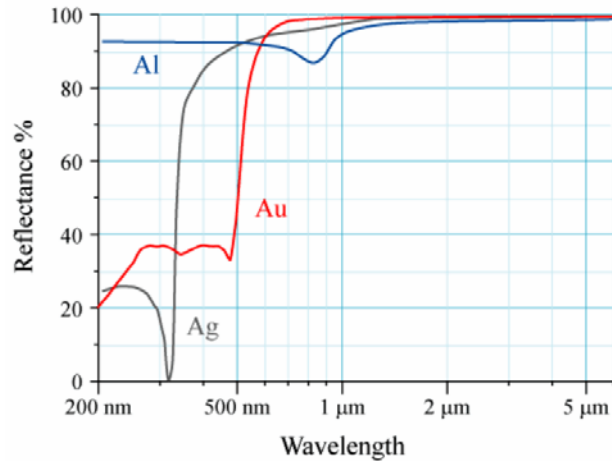


**Figure 62 - Silver, gold, and aluminum reflectivity at normal incidence**

Although flat, front-surface, metallic mirrors have been produced for centuries, only recently have the technologies become available to produce internally reflective-metal coated capillary tubing. Some of the precise details of such endeavors remain trade secrets of their respective manufacturers, but we can still describe basic manufacturing examples herein. In the case of the reflective silver capillary, researchers found that by flowing a solution of silver nitrate inside a smooth-walled capillary tube along with a reducer, a  $\ll 1\mu\text{m}$  thick silver film of high quality could be deposited inside the tube. Figure 63 details one such system. Therein, delivery systems are included for the silver solution, the reducer, and various cleaning agents. A separate iodine delivery system allows the formation of a silver iodide film on top of the silver, which serves to protect the silver film from oxidation for the longevity of reflectivity. A moveable zone-heater is sometimes included which induces silver precipitation and film formation in the heated capillary area during fabrication. Although not shown here, various other MOCVD (metal organic chemical vapor deposition) systems exist for the deposition of the other primary reflective metals. [58-65].

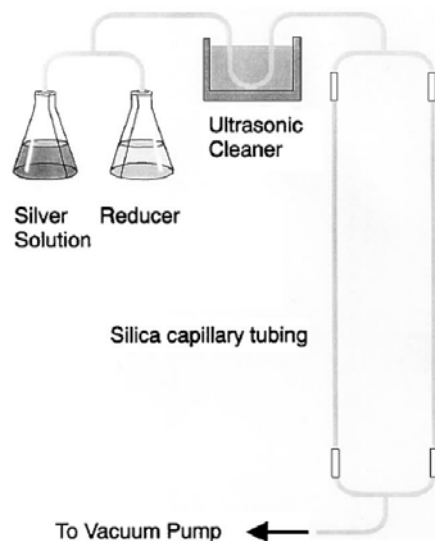


**Figure 63 - Method of silver tubing plating in small diameter capillaries [61]**

Although metal-lined capillary waveguides have been produced by researchers for more than a decade, their commercial production and uses have been limited. Firstly, the minimum size for such a waveguide is about 250 $\mu\text{m}$  inner-diameter. This restriction is simply a manufacturing constraint imposed because of difficulties maintaining solvent flow inside smaller capillary bores. High-quality reflective surfaces have not been reported in smaller tubing diameters.

If the smallest possible metal-lined capillary that can be obtained is  $\sim 250\mu\text{m}$  in diameter, we may intuitively recognize this as a multimode waveguide in the visible or near-IR range. We must therefore conduct a multiple-mode-propagation analysis in order to determine which modes can propagate in the metal capillary, and exactly what the loss in each mode might be.

## 7.2 REFLECTIVE WAVEGUIDE MODES

Figure 64 is a diagram of a metal-lined internally reflective capillary. A pump beam is focused into one end of the waveguide, and is assumed to propagate a short distance through the

waveguide with negligible loss. Again, this assumption is reasonable if the pump beam is launched at a shallow angle and propagates as a low-loss, low-order waveguide mode (like the  $EH_{11}$  mode in Figure 61). We will show later why this assumption is valid for capillaries, although a simple geometric “ray-bounce” picture will suffice for now. As the pump beam propagates down the capillary it can be thought to “bounce” off of the capillary walls, losing power with each “bounce” off of an imperfect reflector. The more shallow the launch-angle of the pump beam, the fewer “bounces” it will incur per unit length, causing the lowest amount of total loss. This picture is not adequate when we begin to look at Raman scattering inside such a waveguide where all angles must be considered. For this, we will invoke a full electromagnetic analysis in our waveguide.

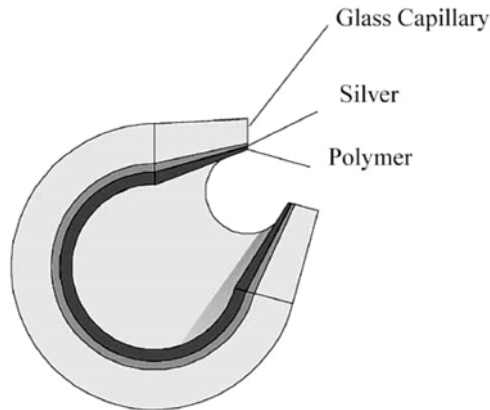


**Figure 64 - Reflective capillary waveguide diagram**

When applying a linearly polarized pump beam to a reflective capillary, we experimentally observe a linearly polarized output beam with a large polarization ratio, indicating the propagation of circularly symmetric linearly polarized modes. This experimental information allows us to infer the types of modes that will propagate in a capillary waveguide and will guide our theoretical approach. A list of all of the circularly symmetric modes has been provided by Stratton (TE, TM, EH, HE, etc.) [77]. The only mode-set therein which exhibits

linear polarization is the hybrid  $\text{EH}_{1m}$  set. We can then infer that the modes propagating in the capillary must be  $\text{EH}_{1m}$  modes from the observation of linear pump-output polarization. We also note that in the absence of a large Raman depolarization ratio (as is the case with most gases), Raman modes should follow a similar pattern of propagation solely as  $\text{EH}_{1m}$  modes. In fluorescence spectroscopy or other scattering techniques, complete analysis may require the inclusion of a number of other mode types which we will ignore here while discussing Raman collection.

Marcatelli and Schmeltzer first derived the loss of a transverse higher-order mode inside a reflective waveguide following the work of J.A. Stratton [67]. The approach involves finding the Eigen-solutions to the characteristic wave equation given boundary conditions available at the walls of the waveguide. For this analysis, we will ignore the effects of the polymer lining on the interior of the waveguide. The purpose of this lining is to protect the reflective metal, and it has been studied somewhat in [58]. Because its thickness is usually much less than the wavelength of the incident light, its effect will be ignored as minimal.

To solve for propagating modes, Maxwell's equations (for electric and magnetic field) are written for modes inside the hollow guide and inside the guide's metal lining. For a generalized cylindrical waveguide structure, we can write that characteristic equation as [78]:

**Equation 36:**

$$\left[ \frac{1}{k_{im}a} \cdot \frac{J_n'(k_{im}a)}{J_n(k_{im}a)} - \frac{1}{k_{em}a} \cdot \frac{H_n^{(1)'}(k_{em}a)}{H_n^{(1)}(k_{em}a)} \right] \cdot \left[ \frac{k^2}{k_{im}a} \frac{J_n'(k_{im}a)}{J_n(k_{im}a)} - \frac{k^2 v^2}{k_{em}a} \cdot \frac{H_n^{(1)'}(k_{em}a)}{H_n^{(1)}(k_{em}a)} \right] = n^2 \gamma^2 \left[ \frac{1}{(k_{em}a)^2} - \frac{1}{(k_{im}a)^2} \right]^2$$

Therein, the  $J_n$ 's are Bessel functions, the  $H_n$ 's are Hankel functions,  $a$  is the radius of the waveguide,  $k$  is the free-space propagation constant,  $v = \sqrt{\epsilon/\epsilon_0}$  is the complex index of refraction of the metal,  $\lambda$  is the free-space wavelength,  $k_{im}$  is a radial constant inside the waveguide for a

particular mode  $m$ ,  $k_{em}$  is similarly a constant in the metal, and  $\gamma_m$  is the axial propagation constant of a particular mode. The integers  $n$  and  $m$  characterize the propagating mode and are defined where  $u_{nm}$  is the  $m^{\text{th}}$  root of the equation  $J_{n-1}(u_{nm}) = 0$ . For now, the equation is applicable to any type of mode within a cylindrical structure. Later, we will concern ourselves only with the polarized modes, which will simplify the equation by setting  $n=1$  for the  $\text{EH}_{1m}$  modes. For the metals aluminum and silver, the complex index of refraction is  $v_{\text{Al}} = 1.08 + 7.01i$ , and  $v_{\text{Ag}} = 0.121 + 3.61i$  at 585nm, respectively. The wave equation is next simplified by applying some reasonable assumptions. First if  $k_e a \gg 1$ , then the asymptotic values of the Hankel functions are used:

$$\text{Equation 37: } \frac{H_n^{(1)'}(k_e a)}{H_n^{(1)}(k_e a)} \approx i$$

It can also be easily shown that:

$$\text{Equation 38: } \frac{v^2}{k_e a} \approx \frac{v^2}{\sqrt{v^2 - 1}} \frac{\lambda}{2\pi a} \ll 1$$

This permits us to disregard powers of  $v^2/(k_e a)$  greater than 1. The characteristic equation then simplifies to:

$$\text{Equation 39 } J_{n-1}(k_{im} a) = i v_{EH} (k_{im} / k) J_n(k_{im} a)$$

where  $v_{EH} = \frac{1}{2} \frac{(v^2 + 1)}{\sqrt{v^2 - 1}}$  for the  $\text{EH}_{nm}$  modes. Because we are only interested in the linearly

polarized modes, we will set  $n=1$  in the following equations. The propagating polarized electric fields can then be written approximately as:

$$\text{Equation 40 } E_{1m} \propto J_0(k_{im} r) e^{i(\gamma z - \omega t)}$$

where  $J_0$  is a first-order Bessel function,  $k_{im}$  is the propagation constant for a particular mode in the guide,  $z$  is the propagation direction, and  $r$  is the transverse direction. If we assume that the metal walls of the waveguide are perfectly conducting, then the electric field must vanish at the walls. This is a reasonable assumption for the determination of the number of propagating modes, but does not take into account the propagation loss of each mode. In the case where we wish to derive losses, we must assume that the electric field is non-zero at the boundary, and the field inside the metal lining is evanescent. For the perfect metal case,  $k_i$  is real and  $\gamma$  is real. At the air/metal boundary:

$$\text{Equation 41} \quad J_0(k_{im}a) = 0$$

The quantity  $k_{im}a$  is therefore a zero of the zero order Bessel function  $J_0$ , or

$$\text{Equation 42} \quad k_{im}a = u_{0m} \text{ or } k_{im} = \frac{u_{0m}}{a}$$

The first five Bessel function zeros are  $u_{(1...5)} = \{2.4048, 5.5201, 8.6537, 11.7915, 14.9309\}$ , and the higher-order zeros of the function can be well-approximated as  $u_{0m} \approx (m-1/4)\pi$ . We can now solve the wave equation in terms of the transverse and longitudinal wave vectors:

$$\text{Equation 43} \quad \gamma_m = \sqrt{k^2 - k_{im}^2}$$

Recall that  $\gamma_m$  is real, so  $k^2 > k_{im}^2$  for each mode, or  $2\pi/\lambda > u_{0m}/a$  for a mode of order  $m$  to propagate. We can now calculate the approximate number of allowable propagating modes as:

$$\text{Equation 44} \quad \frac{2\pi}{\lambda} = (m - \frac{1}{4})\frac{\pi}{a} \text{ or } m = \frac{2a}{\lambda} + \frac{1}{4}$$

Thus, the number of allowable transverse modes relates linearly to the ratio of waveguide size and operating wavelength. Although this simple analysis does not account for the loss of each mode, it does allow us to count the number of modes in a particular guide, or determine the size at which a particular waveguide will operate in single-mode fashion ( $m < 2$ ).

By accounting for evanescent fields in the metal guide and equating the fields inside the metal to those in the air-core (i.e., by allowing  $\gamma$  to be complex), we implicitly calculate the loss for each mode following the same analysis.

In order to solve the characteristic mode equation in this fashion, we invoke the method of perturbation. A first reasonable guess for the value of  $k_{im}$  for a particular mode is

$$\text{Equation 45} \quad k_{im} = \frac{u_{0m}}{a}$$

where  $a$  is the radius of the waveguide and  $u_{0m}$  is a zero of the Bessel function of zero order. Replacing  $k_{im}$  numerically in the characteristic equation and perturbing it with small deviations from its initial value allows us to find a solution which differs only slightly from the perfect metal case. Recall that:

$$\text{Equation 46} \quad k = \frac{2\pi}{\lambda}$$

Once a numerical perturbation of  $k_{im}$  is complete, we can solve for  $\gamma$  as per Equation 43:

$$\gamma_m = \sqrt{k^2 - k_{im}^2}$$

Finally,  $\gamma_m$  provides us with both the power-loss and angle of propagation of a particular order ( $m$ ) mode:

$$\text{Equation 47} \quad \alpha_m = 2 \text{Im}(\gamma_m)$$

$$\text{Equation 48} \quad \theta_m = \cos^{-1}\left(\text{Re}(\gamma_m) \frac{\lambda}{2\pi}\right)$$

We can now produce a plot of mode loss versus propagation angle for reflective waveguides of any size. Figure 65 is a plot of mode loss over all angles from 0-90 degrees for a particular metal-lined guide. (In this case, the propagating wavelength is 632nm, and the waveguide is 530 $\mu$ m in diameter, 2-m long, and lined with silver.) Scattered light emitted beyond 90 degrees

will travel to the opposite end of the guide and follow the same loss distribution as rays exiting the other end.

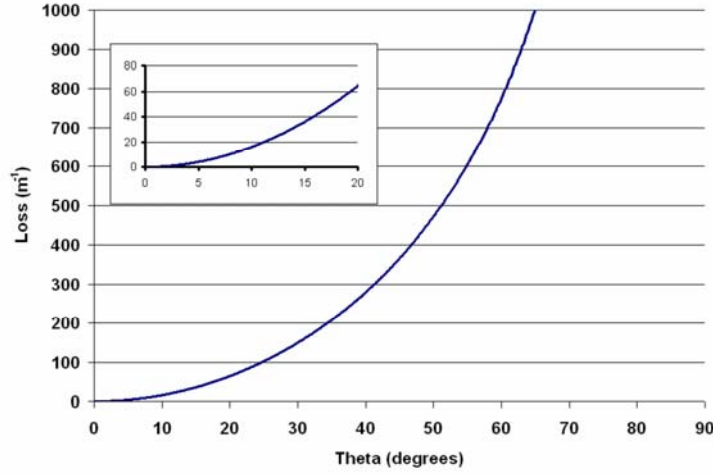


**Figure 65 - Example mode loss vs. angle in a hollow guide. Inset: blowup of data from 0-20°. About 726 modes propagate below 60°.**

Now that we have derived the loss for a particular mode that propagates at a particular angle in a reflective capillary waveguide, we can derive the total collectable scattered light power. Again, we will consider a waveguide filled with a Raman active sample being pumped with a lossless pump beam. Because Raman emissions are omni-directional, we can assume that all propagating modes are equally excited in angular space. Again, there are two popular equivalent methods for determining the total optical power to varying degrees of accuracy. In the first method, we can simply take the loss (which is a function of angle) derived using numerical perturbation analysis and integrate the result.

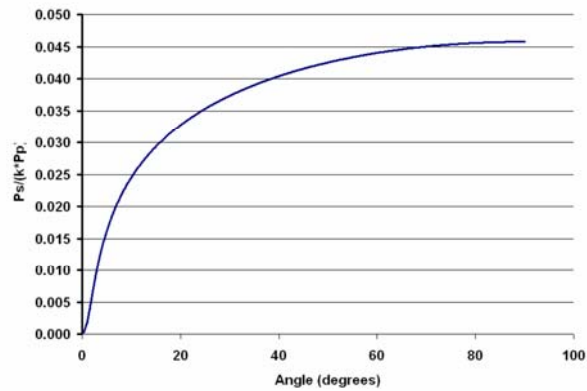
**Equation 49** 
$$dP_s = KP_p \exp[-\alpha(\theta)z] dz d\Omega$$

$d\Omega$  is an increment of solid angle and  $d\Omega = \sin \theta d\theta d\Phi$ , therefore:

**Equation 50** 
$$dP_s = KP_p \exp[-\alpha(\theta)z] \sin \theta d\theta d\Phi dz$$

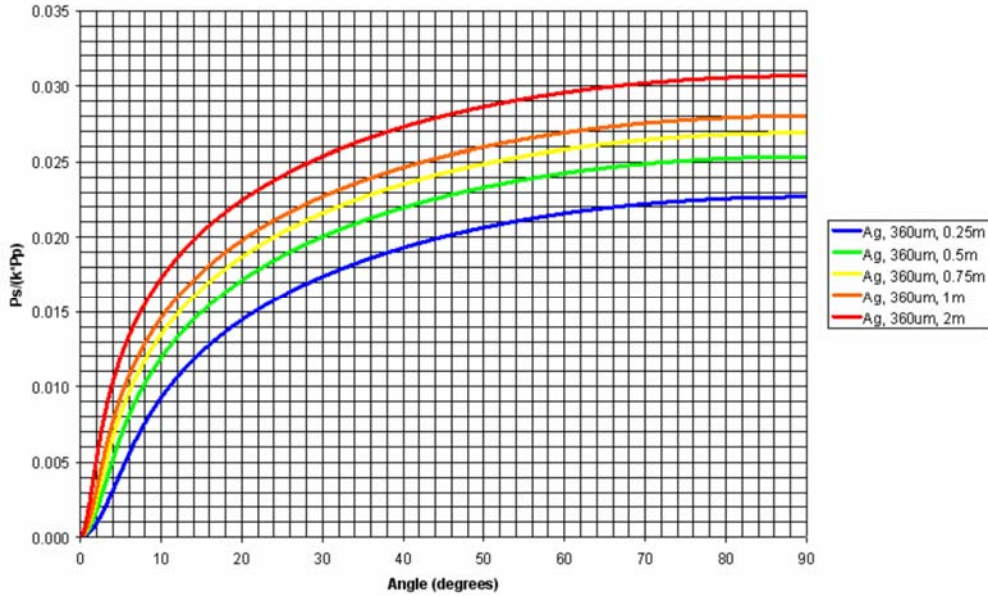
$$P_s = 2\pi KP_p \int_0^\pi \frac{1}{\alpha(\theta)} (-e^{-\alpha(\theta)L} + 1) \sin \theta d\theta$$

Figure 66 is a plot of collectable Stokes power versus angle for a 1-m long silver-lined waveguide with a 320 $\mu\text{m}$  inner diameter. Note that the waveguide is capable of supporting Raman modes at angles up to 90 degrees, although most of the power is contained towards much smaller angles. Therefore, a metal waveguide limits the angular output with increasing loss towards larger angles, without eliminating them entirely as would occur in a single-mode waveguide or step-index fiber.



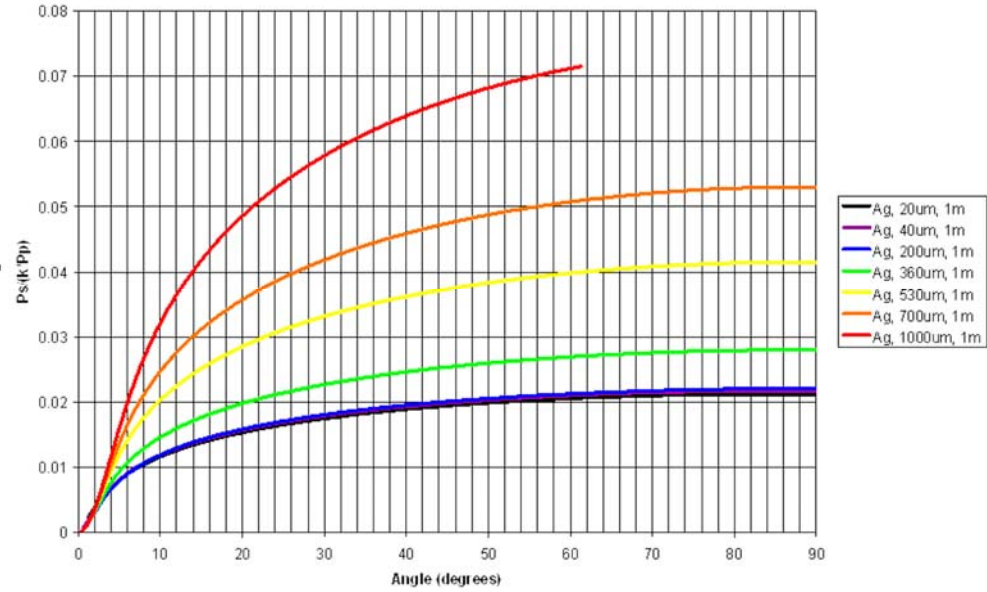
**Figure 66 - Collectable Stokes Raman power from a 320 $\mu\text{m}$  I.D. 1-m long silver-lined capillary**

Figure 67 shows the distribution of  $P_s$  for a range of waveguide lengths. As length increases, total power also increases; but with diminishing marginal returns - i.e., an infinite waveguide is only marginally better than a kilometer-long waveguide. In practice, waveguides approach their reasonable maximum utility at a few meters long.



**Figure 67 - Collectable Stokes power normalized with respect to species and laser power vs. angle for different hollow-waveguide lengths**

For illustrative purposes, we have also included a plot of various diameter waveguides of the same length. Figure 68 is a plot of Stokes power for 20, 100, 200, 400, and 1000 $\mu$ m inner diameter waveguides, each 1-m in length. Again, a non-linear relationship exists between the diameter and total collectable power. Waveguides between 20 and 100 $\mu$ m inner diameter exhibit very little difference in power collection, while larger diameter tubes increase total power non-linearly for the same increment in diametral variation.



**Figure 68 - Collectable Stokes power normalized with respect to species and laser power vs. angle for different hollow-waveguide diameters**

A second method may be used to provide a closed-form solution to the Stokes power equation. We can implement the simplifications utilized by J.P. Crenn for modes at small angles [66]. Consequently, this approximation was also first suggested by Marcatilli et al. The field loss coefficient ( $\alpha$ ) depends on  $\theta$ . Crenn shows that the following expressions are correct for the  $\text{EH}_{11}$  mode and his expressions can be extended to the  $\text{EH}_{1,m}$  modes so that:

$$\text{Equation 51} \quad \alpha_m = \frac{u_{1,m}^2}{k^2 a^3} \frac{\nu_R}{2} \quad \text{and} \quad \theta = \frac{u_{1,m}}{ka}$$

where  $k = 2\pi/\lambda$ ;  $a$  is the radius of the capillary,  $\nu_R$  is the refractive index of the metal, and  $u_{1,m}$  is the  $m^{\text{th}}$  root of the Bessel function  $J_0(x)$ . The multiplier  $\nu_R$  is an approximation of  $2 \cdot \text{Re}(\nu_{EH})$ . This is valid both for aluminum and silver at visible wavelengths. Equation 51 above can be manipulated to write:

$$\alpha_m = \frac{\nu_R}{2a} \theta^2 = C_3 \theta^2 \quad \text{where } C_3 \text{ is a short hand for } \nu_R / (2a).$$

We can integrate over  $\varphi$  easily (nothing depends on  $\varphi$ ) and then write:

$$\text{Equation 52} \quad P_s = 2\pi K P_p \int_0^\pi \int_0^l \exp(-2C_3 \theta^2 z) dz \sin \theta d\theta$$

The integrand (for the z integration) is in standard form and

$$P_s = \frac{2\pi K P_p}{-2C_3} \int_0^\pi \frac{\exp(-2C_3 \theta^2 z) \Big|_0^l}{\theta^2} \sin \theta d\theta = \frac{2\pi K P_p}{-2C_3} \int_0^\pi \frac{\exp(-2C_3 \theta^2 l) - 1}{\theta^2} \sin \theta d\theta$$

we can write this as

$$\text{Equation 53} \quad P_s = \frac{\pi K P_p}{C_3} \int_0^\pi f(\theta) d\theta$$

where the angular distribution function  $f(\theta)$  is:

$$\text{Equation 54} \quad f(\theta) = \frac{1 - \exp\left(-\frac{v_R l \theta^2}{a}\right)}{\theta^2} \sin \theta$$

In the only cases of interest,  $\sin(\theta) \approx \theta$ . The analysis above derives the square law relationship between  $\theta$  and  $\alpha$  ( $\alpha = C_3 \theta^2$ ). This is an approximation for the solution of the equation:

$$\cos \theta = 1 - \frac{u_{1m}^2}{2(ka)^2} \quad \text{and} \quad \alpha = \frac{u_{1m}^2}{k^2 a^3} \cdot \frac{v_R}{2}$$

A more precise expression for  $\alpha$  is thus found from:

$$2(1 - \cos \theta)(ka)^2 = u_{1m}^2 \quad \text{which implies:}$$

$$\alpha = \frac{v_R}{a} (1 - \cos \theta) = 2C_3 (1 - \cos \theta)$$

This expression for  $\alpha$  is identical to the previous one for small  $\theta$ . Following through the analysis given above for  $P_s$  and  $f(\theta)$  we find:

$$\text{Equation 55} \quad P_s = 2\pi k P_p \frac{a}{v_R} \int_0^\pi \frac{1 - \exp[-\frac{2v_R}{a}(1 - \cos\theta)l]}{1 - \cos\theta} \sin\theta d\theta \quad \text{and}$$

$$\text{Equation 56} \quad f(\theta) = \frac{1}{2} \frac{1 - \exp[-\frac{2v_R}{a}(1 - \cos\theta)l]}{1 - \cos\theta} \sin\theta$$

Two other important features of this simplified collectable Stokes power distribution should be observed. Firstly, the power expression (Equation 55) contains only the ratio of  $v_R/a$  (or  $a/v_R$ ). The real part of the index of refraction ( $v_R$ ) and the radius ( $a$ ) do not appear outside of this ratio in the equation. We can therefore equate the collection capabilities of waveguides fashioned from different materials and different diameters via this ratio. For instance, a silver waveguide ( $v_R = .121$  @585nm) with a diameter of 300 $\mu$ m is equivalent in collectable power to an aluminum waveguide ( $v_R = .826$  @585nm) with a diameter of  $\sim 2.05$ mm. If the smallest possible waveguide-area is sought for detector matching (as we will discuss in the next section), then the material with the lowest possible real index of refraction at the wavelength of interest should be used. The other important feature to note is the output behavior towards large angles. Obviously, angles beyond 90 degrees will produce Stokes photons in the wrong direction, and will not contribute to single-ended collection. As angles approach 90 degrees, the loss approaches infinity, which corresponds to the absence of Raman output at 90 degrees. If we compare the large-angle behavior of the perturbation solution of the characteristic equation, to the “fixed-form” simplifications offered by Crenn, we note that the simplification is only rigorously correct to about 10 degrees. Also, the absolute power output should level-off completely and asymptotically approach its value at 90 degrees, instead of increasing at a higher rate. Figure 69 compares the two solutions in a silver waveguide with a 320 $\mu$ m ID:

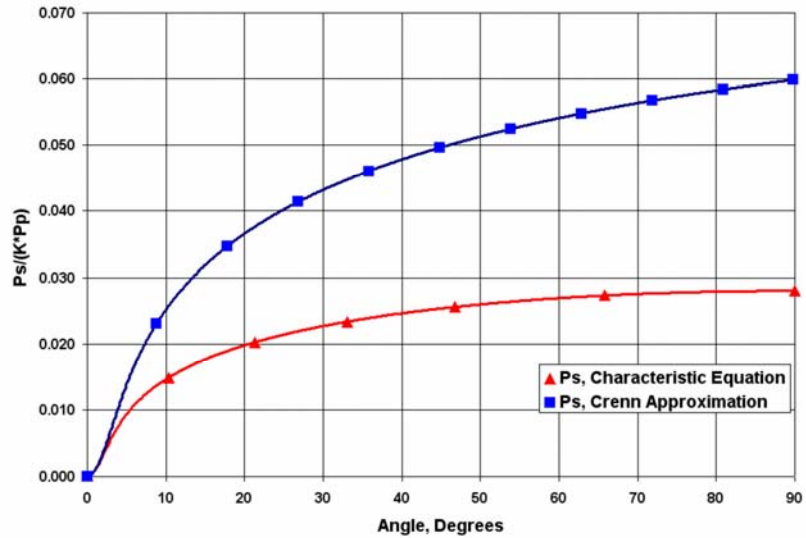


**Figure 69 - Collectable Stokes power calculated using the characteristic equations or the Crenn simplification**

### 7.3 LARGE WAVEGUIDE DETECTOR MATCHING

Initially, we outlaid the inherent problem with Raman scattering collection of large signals being the omni-directional nature of scattering. The basic ideas behind this problem have not changed. In essence, the notions suggested for effective collection of single-transverse mode Raman signals emerging from an HC-PBF are the same. We are simply now burdened with a much less constrained collection optic in the form of a multimode capillary waveguide. As we have shown, these waveguides do in fact produce large angular output patterns, which will obviously not ‘fit’ into fixed angular-aperture detection equipment. Furthermore, the large diameters of metallized waveguides are far less compatible with spectroscopic detection equipment relying on small slit widths and fixed linear dispersion.

We can, however, illustrate the preferred means of matching such a waveguide to a detection system for measurement. Previously, we observed that all optical detectors possess some fixed-area, fixed angular-acceptance collection aperture. Our goal is now to ensure that Stokes power reaching the detector is maximized. We will consider three possible scenarios. Firstly, we can describe a single-mode fiber with limited angular output impinging on a spectrometer with fixed entrance with free-space coupling optics. We can also look at reasonable-diameter multimode waveguides impinging on the same spectrometer with free-space optics. Finally, we will discuss the use of fiber-bundle style coupling for very large guides.

Before we begin our discussion of detector matching, we should briefly define some non-standard terminology. The angular acceptance value (or aperture) of a lens is given by some value  $\theta_{\max}$ . This is the half-angle of the largest cone of light that can enter or exit the lens. We define the Numerical Aperture (NA) of that lens by:

$$\text{Equation 57 } NA = n_o \cdot \sin(\theta_{\max})$$

where  $n_o$  is the index of refraction of the medium surrounding the lens. Traditionally, the divergence exhibited by optical fiber output (or input) is also described by an NA value. For step-index fibers, the NA is calculated in exactly the same way. Some optical fibers or waveguides exhibit output patterns which decrease in intensity towards larger angles, instead of dropping to 0 at some maximum angle. In that case, we will define  $\theta_{\max}$  where the output intensity drops to  $1/e^2$  of its maximum value. We define the same parameter for Gaussian beams, allowing us to invoke the NA or f# of a Gaussian beam to describe its divergence. When discussing the angular acceptance of detectors or detection equipment, the term f# (pronounced “eff-number”) is more commonly used. The f# is calculated as:

$$\text{Equation 58 } f\# = \frac{f}{D} = \frac{1}{2 \cdot NA}$$

where  $f$  is the focal length and  $D$  is the diameter of the entrance aperture or lens. In this work, we use the terms  $f\#$  and NA to describe the angular acceptance or output of various waveguides, lenses, detectors, or other devices. We do not attempt to adhere to any convention regarding the use of one term over the other, despite drawing the ire of traditional opticians or photographers.

*Case #1 – Single mode waveguide coupling to spectrometer in free space*

The simplest form of detector matching required for these experiments involved mating a single-mode (HC-PBF) waveguide or fiber to a spectrometer using free space optics. Figure 70 details the components.

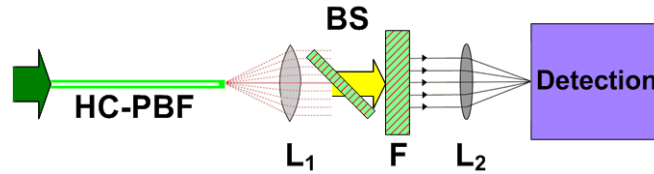


**Figure 70 – Single-mode coupling and magnification**

Basically, lens  $L_1$  is used to collimate the Stokes output from the fiber. To ensure total light collection, this lens must have an NA larger than that of the fiber. The size of the collimated Gaussian mode given by geometric optics will be approximately:

**Equation 59**     
$$D = 2f_i \tan\left(\sin^{-1}\left(\frac{NA}{n_o}\right)\right)$$

This beam diameter ( $D$ ) indicates the size of clear aperture required for subsequent portions of the optical train, such as the clear diameter of  $L_2$ . In a forward scattering arrangement where  $L_1$ 's only purpose is to collect Raman, (and not to focus a pump beam)  $L_1$  need not subscribe to any other parameters but the minimum NA requirement for collecting all of the angular Raman output. In the case where  $L_1$  is also used to focus the pump beam, (backward scattering)  $L_1$ 's focal length must be chosen with the pump beam diameter in mind for low-loss pump propagation within the NA of the waveguide. Because of the broadband spectral nature of

Raman scattering,  $L_1$  should be as achromatic as possible to ensure that the pump beam coupling and Raman output collimation occur at the same lens position in space.

The choice of  $L_2$  is somewhat more complicated in the single mode coupled system. In choosing it, we must first attempt to match the  $f\#$  of the spectrometer to that of the waveguide. In the two lens system (where the distance between  $L_1$  and  $L_2$  is rigorously  $f_1+f_2$ ), an image of the fiber end-facet is produced on the spectrometer entrance slits (or detector, etc.). The size of this image is:

$$\text{Equation 60} \quad D_2 = \frac{f_2}{f_1} D_1 = M D_1$$

where  $D_1$  is the fiber diameter and  $M$  is the magnification factor. If  $f_2$  is increased, the size of the fiber-image increases, while the maximum angle of incidence decreases. The magnification can thusly be tuned so that all emitted Stokes rays make it through the spectrometer and are detected where:

$$\text{Equation 61} \quad NA(\text{fiber}) / NA(\text{spectrometer}) = \frac{f_2}{f_1}$$

Unfortunately, as the angular output of the waveguide in question becomes larger and  $f_2$  is increased to fit all rays into the detection equipment, the size of the focused entrance image becomes larger. We can then see how maintaining large angular output incurs a decrease in available resolution. Slit size must be increased in order to “fit” the magnified fiber image. In a standard dispersive spectrometer, larger slits imply less spectral resolution, which is undesirable for Raman transitions or other spectroscopic studies with closely-spaced emission lines. Therefore, matching a waveguide with a particular NA to a spectrometer with a fixed entendue will result in a limited resolution for total-power collection, or lower collection efficiency traded for high resolution. In many cases, a balance of the two features can be reached with the proper

choice of coupling lenses. In many of the PBF experiments reported here, a unity magnification was implemented because the angular output of visible HC-PBF modes was usually on the order of  $NA \approx .12$ , which was smaller than that of our  $\frac{1}{2}$ -m imaging spectrometer (JY iHR550) apertured at  $f/6.4$ . Therefore, unity imaging of the fiber core ( $\sim 5\mu\text{m}$  I.D.) would provide extremely high spectral resolution while still collecting all of the rays emitted by the fiber. Slight magnification could have been performed to more uniformly fill the angular entrance aperture for maximum grating efficiency, but was not deemed necessary.

*Case #2 – Multimode waveguide coupled to a spectrometer in free space*

The same resolution vs. power tradeoff is apparent when attempting to collect the maximum possible power from a large multimode waveguide using free-space optics. The problem however, becomes much more acute. Common spectrometer slit widths are usually in the range of  $25\mu\text{m}$  to  $2\text{mm}$ , owing to the manufacturing limits on dispersive holographic or ruled gratings and the physical size of available spectrometers. Available metal-lined capillaries were obtained with inner diameters in the  $300\mu\text{m}$ - $2\text{mm}$  diameter range. According to Figure 68,  $1/e^2$  power output can occur at angles as large as  $\sim 40$  degrees. Common spectrometer entrance apertures are in the range of  $f/2$  to  $f/9$ , or between  $14.4$  and  $3.2$  degrees ( $1/2$  angle). Obviously, in some cases the slit size will be large enough to allow for similar free-space magnification of the capillary output image to facilitate near-full collection. Regardless of how much magnification is used, some fraction of capillary angular output will be lost near  $90$  degrees. If a free-space optical setup is used (see Figure 70),  $L_1$  must again be chosen with an NA large enough to collect a majority of the capillary output. It is also necessary to utilize a higher-quality aspheric lens in this application to properly collimate rays propagating far from the lenses' center

line. In most cases, magnification of a  $>300\mu\text{m}$  diameter fiber image will result in spectral resolution that is far too coarse for accurate Raman measurements.

Often, the best possible solution to the large waveguide coupling problem is to simply optimize the collimation and focusing lenses for maximum power. To that end, we should first determine the acceptable wavelength-resolution for detecting all of the Raman species in question. That resolution will imply the size of the output image at the detector or spectrometer slits. The image size gives the maximum value of magnification that can be used while still fitting the entire capillary image into the slits. Next, the angular collection can be determined. In the event that the required resolution implies the loss of too much angular output, then we are again at an impasse with no possibility for improvement. In essence, in the case of the largest waveguides, we have returned to the same set of problems evident in free space. We are left with divergent rays at large angles which must be reduced, along with a large cross-section which must also be reduced for maximum power collection. As we noted, the collected size and angle vary inversely in free space optics. The use of larger waveguides or cells therefore does not improve the collected power given fixed-entendue detection equipment. In theory, larger Stokes signals can be obtained from larger diameter capillaries; but are ultimately limited by detector size and aperture.

### *Case #3 – Large guides and Fiber Bundles*

The solution to the large waveguide/detector coupling problem has emerged in the use of fiber-optic bundles. A fiber bundle is basically an area-transforming device, illustrated in Figure 71. Therein, tens or hundreds of optical fibers are arranged in a particular “shape” or pattern at one end; which is mated to the capillary or to the magnified capillary image. The other ends of the bundle-fibers are arranged in an entirely different shape, such as a slit rectangle. This type of

device exhibits macro-characteristics which are dramatically different from free-space beam propagation. The spatial grouping of a large number of multimode fiber waveguides creates a macro-optic device which is capable of affecting propagation in ways which conventional waveguides can not, while introducing minimal optical losses. We can, in many cases, design a fiber bundle to collect a majority of the Stokes output from a large hollow waveguide. Our procedure for this design will be as follows. First, we will reduce the angular output from a large capillary waveguide using free space optics such that the image of the capillary is increased in size; and the angular output is reduced to fit the detector. A fiber bundle will then be used to transform the even larger resultant round image into a rectangular image to provide high spectral resolution for subsequent single dimensional dispersion.

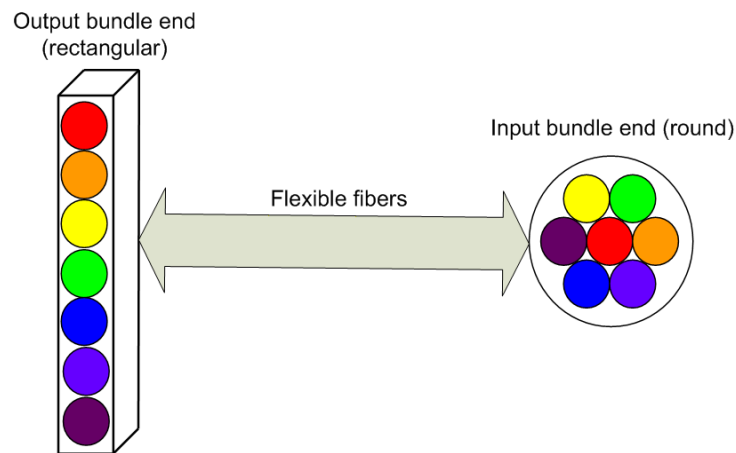


**Figure 71 - Fiber bundle diagram: individual fibers shown in different colors**

A few rules should be followed in the design of such a bundle. First, the solid angle of light entering each fiber in the bundle will essentially be the same as the solid angle at the output, provided that the launch light falls within the fiber NA. In this case, the NA of a multimode step-index fiber is given approximately by:

$$NA = \frac{1}{n_0} \sqrt{n_{core}^2 - n_{cladding}^2}$$

where  $n_{\text{core}}$  is the index of refraction of the core,  $n_{\text{cladding}}$  is the index of refraction of the cladding, and  $n_0$  is the index of refraction of the surrounding medium. It is important to understand that the fiber bundle itself will not alter the angular output of the Stokes signal. We must still perform a magnification operation before or after the bundle in order to facilitate angular matching to the spectrometer. The merits of the fiber bundle are apparent when we consider available resolution and total detector area.

Ruled or holographic dispersion gratings produce dispersion in 1-dimension (usually in the horizontal plane). Detectors often possess significant area ( $1\text{-cm}^2$  for some PMTs and CCD arrays), but in order to achieve high resolution in the dispersion direction, we must limit the horizontal size of images in the slit plane in order to effectively discriminate wavelength information in the detector plane. The fiber bundle allows us to do just that. We will choose to first magnify the large capillary image to an even larger size in order to limit its angular divergence to fit into the bundle-fibers. The larger image is then focused onto the round end of the bundle. The bundle-fibers' other ends are arranged in a vertical line to match the slit or detector area. Because of the single axis dispersion and generally large detector area, high resolution can be maintained while preserving a majority of incident optical power. In this case, the spectral resolution is a function of the core diameter of individual fibers in the bundle. Slit width must be set to the core diameter of the bundle fibers for optimal coupling. The total area of the fibers in the bundle should be equal to the area of the magnified capillary image, while still being less than or equal to the slit and detector area. It is also important to be aware of the properties of the fibers used in the bundle, as they may affect collection adversely. Because the fibers have some finite cladding diameter, it is not possible to create a bundle without any "dead space". Light launched directly into the cladding at the entrance end of the bundle will be lost.

In addition, normal propagation losses will occur in the bundle, which will reduce the total collected power. If these losses can not be minimized appropriately, use of a bundle may ultimately not be helpful, as its aim is to increase total collected power. Finally, the use of standard multimode step index fibers in a bundle can always introduce additional noise or artifact signals such as silica Raman, cladding fluorescence, or impurity transitions which can also have adverse effects on SNRs.

In order to clarify the use and practice associated with fiber bundle operation, we will illustrate a short example using actual experimental parameters. Figure 72 shows a portion of a Raman sensing apparatus featuring a large-diameter capillary waveguide. In order to achieve high-power collection of Raman signals from the capillary (C) in the Figure, we must choose the components as dictated above. First, we will begin by assuming that we have a 300 $\mu\text{m}$  ID capillary waveguide, a spectrometer with a dispersion of 1.37nm/mm, and that we require a measurable resolution of about 0.25nm. The spectrometer dispersion and required resolution dictate the slit width as  $S = 0.25\text{nm}/1.37\text{nm/mm} = 0.182\text{mm}$ . The slits must be less than 0.182mm wide in order to achieve the desired resolution. We will then specify all of the system components to achieve maximum power collection at that resolution. For simplicity, we will assume a fiber bundle that uses a single row of fibers at the output and a round assembly at the input. In that case, the core diameter of the fibers will be  $D_f = 182\mu\text{m}$ . The rectangular ( $B_2$ ) end of the bundle will be placed in the slit entrance plane of the spectrometer. Actual slits are technically unnecessary because the fiber diameter serves as the delimiting aperture. To specify the number of fibers in the bundle, we must know the slit or detector height (whichever is smaller). Dividing the height of the slits by the outer diameters of the available fibers to be bundled yields the number of fibers in the bundle. If the slits are 1cm high, and the 182 $\mu\text{m}$  core-

fibers have outer-diameters of about 200 $\mu\text{m}$ , then 50 such fibers will “fit” in the slit area with little loss of the light emerging from the bundle.

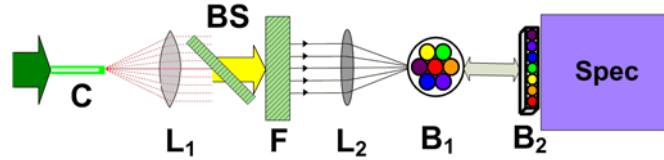


Figure 72 - Fiber bundle design example

After choosing a fiber-bundle based on the necessary resolution and slit height, we must match the large-waveguide output to the fiber bundle input end. We have already specified the cross-sectional area of the fibers at the output end, so it is simple to specify the overall bundle-size at the input end. The area of the bundle at the output end ( $B_2$ ) is:

$$\text{Equation 62: } A_{B_2} = 50 \cdot \pi \cdot \left( \frac{200 \mu\text{m}}{2} \right)^2 \approx 200 \mu\text{m} \cdot 1\text{cm} = A_{B_1}$$

We can now calculate the diameter of the input end of the bundle from its area if we ignore the imperfect packing associated with bundling the fibers into a round shape. The total fiber bundle input diameter ( $D_1$ ) is then found by solving:

$$\text{Equation 63: } A_{B_1} = \pi \left( \frac{D_1}{2} \right)^2, D_1 = 1.41\text{mm}$$

We note that the fiber bundle input facet is several times larger than the waveguide diameter. From the previous Chapter, we know that the angular output of a large capillary waveguide exists up to 90 degrees, so the largest angular collection is accomplished with the largest magnification of the capillary image. We will then magnify the image of the capillary using  $L_1$  and  $L_2$  so that the capillary image is as large as possible on the bundle input facet. This implies that the magnification should be:

**Equation 64:**  $m = \frac{L_2}{L_1} = \frac{D_1}{D_{cap}} = \frac{1.41mm}{0.3mm} = 4.7$

A 4.7X reduction in capillary angle will result from this image magnification. Therefore, the spectrometer will collect 4.7X more angular output than in the case where the capillary is placed directly in front of the slits.

Finally, we can make choices with regard to  $L_1$  and  $L_2$  themselves. Although only the ratio of their focal lengths is important for matching the capillary image to the spectrometer, we must ensure that the NA of both lenses is large enough to accept the light being collected. For this, we should first look at the NA of the bundle-fibers. For this example, we assume that the fibers are of a standard multimode variety having an NA=0.22. First, this NA should be smaller than that of the spectrometer to ensure that rays do not miss the grating or detector inside the spectrometer. If this condition is met, we must then ensure that rays are not lost at either lens. If not, we must consider reduction of the magnification until this condition is met.  $L_2$  should have an NA of at most 0.22 to match that of the fibers.  $L_1$  should have an NA 4.7X larger, or >1.03. In general, there will also be a requirement placed on  $L_1$  by the necessary pump-launch angle required for low loss pump propagation. That will determine the minimum focal length of  $L_1$ . If the focal length of  $L_1$  is known, then the diameter is implied by the NA requirement. Then,  $L_2$  is determined by the magnification ratio. If our pump beam is adequately launched by a 25mm-efl lens, then (following Equation 58) it's size must be  $D > 2 * 1.03 * 25mm > 51.5mm$  in diameter. The diameter of  $L_2$  must be at least as large as  $L_1$  so that the collimated Raman beam is not apertured by the second lens. Using this simple method, we can calculate the appropriate bundle and coupling lenses for any such setup.

## **8.0 RAMAN SENSING EXPERIMENTS USING METAL-LINED CAPILLARY WAVEGUIDES**

In order to verify predictions regarding the transmission and other properties of reflective metal-lined capillary waveguides, a number of such devices were purchased for evaluation. To date, a very limited number of manufacturers of such waveguides exist. Doko Engineering (Japan) has emerged in this field as a leader in waveguide quality. Their commercial waveguide offerings are currently restricted to silver and aluminum waveguides with internal diameters ranging from 320 $\mu\text{m}$  – 1mm. Structurally speaking, these waveguides are all produced using a temperature-controlled MOCVD process to deposit the silver or aluminum inside the capillary tubes. Silver guides are produced with an additional, very thin polymer coating on the inner surface to protect the silver from oxidation on exposure to air, which does not adversely affect the transmission properties of the waveguide [63].

In the following sections, we will review experimental results designed to provide specific operational data. First, some review of the basic spectra and intrinsic spectral features of the waveguides will be conducted. Then, experiments designed to verify the mode simulation results from the previous chapter will be introduced. The final section will cover information necessary for the realization of an operable real-time Raman system including gas-transfer characteristics and a comparison of detection limits with previously-explored PBF systems.

## 8.1 CAPILLARY RAMAN SPECTRA AND NOISE

The first step in evaluating reflective capillaries as Raman collection cells was to construct a capillary Raman system and review the Raman spectra from various gas sources. Then, the system could be evaluated in terms of the noise-sources present, as well as the observed collection efficiency. In previous PBF experiments, the primary source of system noise was determined to be a background of silica Raman emanating from the solid glass structure surrounding the fiber-core. Noise in the capillary system could similarly be a result of silica Raman from the glass walls. Since the capillary is constructed with a polymer jacket (outside the glass) as well as a protective polymer lining (inside the metal), the capillary may exhibit fluorescence when pumped with a short-wavelength laser. Polymers of various types are known to fluoresce when excited with high-enough energy photons, so this source of noise will be carefully considered. Finally, yet unknown sources of noise could be present.

To evaluate the plausibility of Raman collection using a capillary waveguide, the experimental apparatus in Figure 73 was constructed. Many similarities exist between this setup and the one used previously to implement sensing with PBFs. The lenses  $L_1$  and  $L_2$  serve basically the same functions as those in the PBF setup. The purpose of  $L_1$  is still to collimate the emerging Raman beam and to focus the pump beam into the capillary. The purpose of  $L_2$  is simply to focus Raman light into the spectrometer. Recall that mathematical analysis of capillary guides indicated that large output Raman angles can easily be collected, so  $L_1$  was chosen to have a very high NA. In practice,  $L_1$  had a 20mm focal length and a diameter of 1" (25.4mm). In order to ensure that the pump beam, which is also launched through this lens, propagates in only in the lowest order, lowest loss waveguide-modes; a 5:1 beam compressor was inserted in the pump-beam path before the beam was reflected off of the dichroic

beamsplitter (BS) into the capillary. The overall effect of the beam compressor is to reduce the size of the pump beam by 5X so that after focusing, its launch-angle is still very small, resulting in propagation in low-order waveguide modes despite the short efl of  $L_1$ . The capillary used in initial experiments was a  $320\mu\text{m}$  inner-diameter silver-lined guide, 1-meter in length.

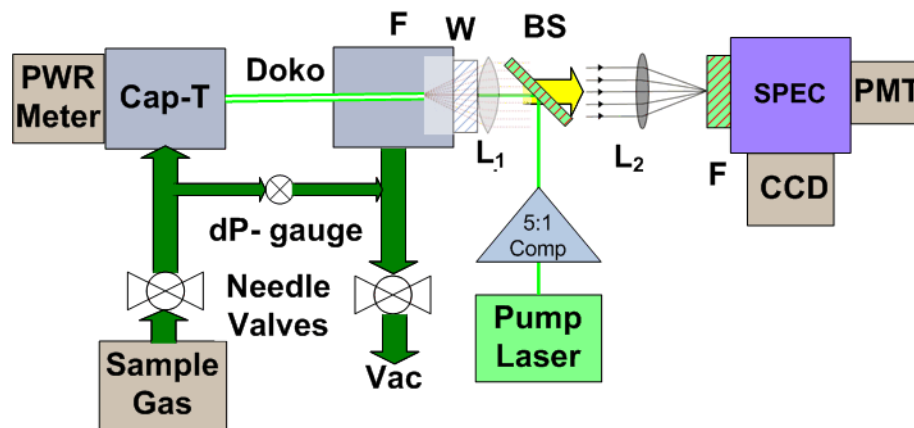
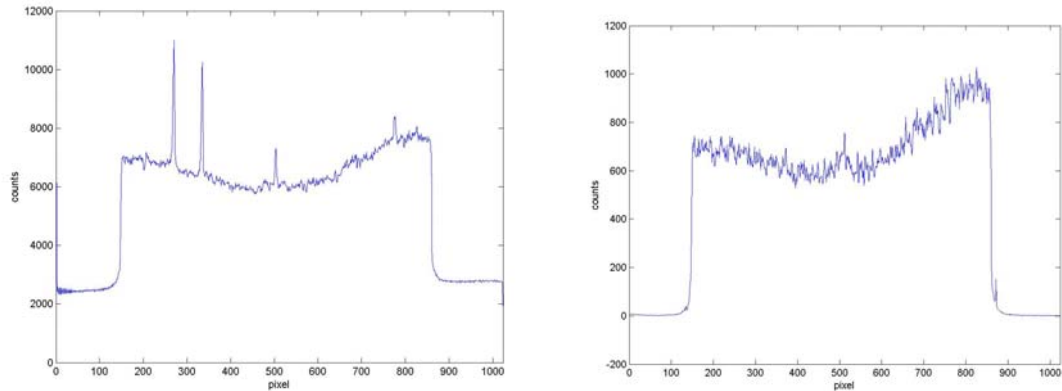


Figure 73 - Diagram of experimental capillary Raman system

Figure 73 also diagrams the various gas-transfer components included in the capillary Raman instrument. In general, the hollow core of a capillary guide is around 2 orders of magnitude larger in diameter than the PBFs used in our systems. At similar pressures, gas flow through these capillaries will be extremely fast if the capillary itself is the only restriction to flow. That is why several additional gas-handling components have been added to the system. First, flow-control valves have been added to the upstream and downstream ends of the capillary. A differential pressure gauge has been placed across the capillary to allow measurement of the differential pressure in addition to measurement of the upstream head pressure. This setup enables the capillary to be kept at any given upstream pressure, while controlling the downstream pressure with the applied flow. Thus, the entire capillary can be pressurized up to several 10's of atmospheres while the differential pressure can be maintained as low as a few psi. By maintaining high overall sample pressure along the capillary length, large Raman signals can

be generated even near the lower-pressure output end of the tube. The exact value of the small differential pressure will determine the sample-exchange rate as was outlined in Chapter 5.0 . The output end of the capillary is again fitted with a small capillary t-fitting to ensure an air-tight connection, with light power being diverted through a window in the t-fitting to a power meter for alignment purposes. A vacuum line is provided to allow vacuum spectrum measurements, although it was found to be unnecessary to evacuate the capillary as it was in the case of PBF for the elimination of residual samples.

During initial experimentation, an argon-ion laser operating at 514.5nm was used to pump the capillary in the backscattering configuration shown in Figure 73. About 30mW of pump power was measured at the output of the guide. Initially, the capillary was filled with atmospheric pressure air as a control experiment designed to measure known nitrogen and oxygen lines in the presence of background generated by this experimental configuration. Figure 74 records the air-spectrum on an Eg&G intensified linear silicon array (1421IR). Part A of the Figure is a silicon array recorded spectrum centered on the 584.5nm ( $2231\text{cm}^{-1}$ ) nitrogen line, with calibration lines (at 577 and 579nm or pixels  $\sim 293$  and 351 respectively) added from a mercury lamp switched on briefly during the 5 second exposure. Part B of the same figure is centered at 559nm and displays the weaker oxygen line. A large background signal is noted.



**Figure 74 - Preliminary capillary Raman spectrum, A: Nitrogen line centered at 584.5nm with mercury calibration lines at 577 and 579nm. B: Oxygen line at 559nm.**

To evaluate the source of the background noise in Figure 74, it was next necessary to view a much larger portion of the output spectrum. Figure 75 shows the same Raman air-spectrum recorded from 500-820nm. This spectrum was obtained by recording 15 individual ~20nm wide spectra and concatenating the results. Concatenation without any sort of intensity correction across this particular detector array results in the “scalped” appearance due to higher responsivity near the ends of the array. The important features to observe in the spectrum include firstly, a large peak emerging near the cut-on of the long-pass filter (at about 517nm) which appears similar to the silica Raman band previously viewed in PBF experiments. Secondly, a very broad (several hundred nanometers) continuous background appears (in addition to the large near-pump peak) with a peak near ~630nm.

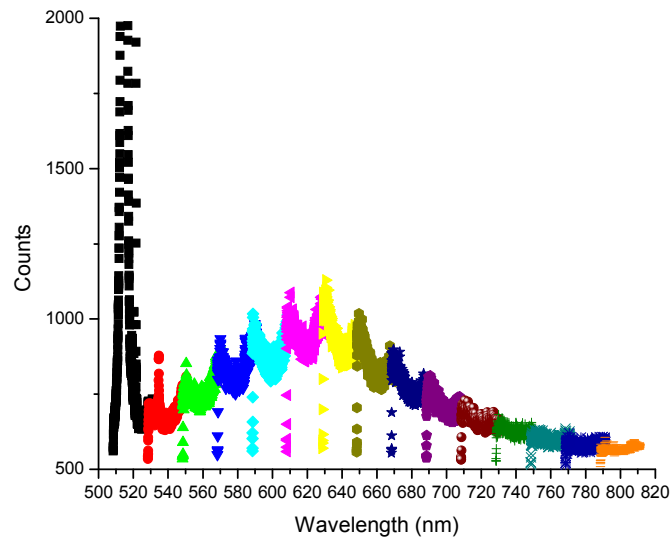


**Figure 75 - Raman spectrum from an air filled capillary, 514.5nm pump wavelength, 320 $\mu$ m ID, 1-m long**

Reviewing the wide-band Raman spectrum allows us to infer the sources of noise present in the capillary spectrum. Because the larger peak in the spectrum appears similar in shape and location to previously-observed silica Raman bands, we can infer that some silica Raman component is being produced and collected by the capillary. This is entirely reasonable given the finite loss of the silver coating and inevitable pump-leakage into the solid glass walls of the tube. The second peak in the spectrum is somewhat more difficult to characterize. Because there is a trend of increasing power moving away from the pump wavelength and peaking somewhere in the red portion of the spectrum, it is likely that broadband fluorescence is being produced by one of the polymer capillary components. Removal of the capillary itself for a single exposure with all other optical components present proved that this signal is indeed also generated by the capillary.

An additional simple experiment was designed to clearly indicate the source of the broadband noise present in initial capillary experiments. Because a broad peak suspected to be

some fluorescing part of the capillary was observed, it was necessary to conduct an experiment pumping the capillary with a much longer wavelength source. By pumping with a wavelength longer than the suspected fluorescence peak, it may be possible to eliminate such fluorescence and definitively indicate the source of emissions. Figure 76 shows a spectrum of the same capillary pumped with a tunable Ti:sapphire laser operating near 775nm. It is important to note that all of the filters, beamsplitter, and detector were replaced for measurement at the longer wavelength. The detector used herein was in fact the 2D Roper scientific 1024X252 pixel device described previously. This spectrum shows the same silica-Raman near-pump peak observed in the visible spectrum. It is, however, absent of the broadband peak observed with visible pumping, indicating the presence of fluorescence in the visible scheme. The small peak from atmospheric nitrogen (at ~946nm) is observable, although the peak from oxygen is too weak to see at this longer pump wavelength. One additional line is present near ~952nm which was determined to be plasma emission from the argon laser pumping the Ti:sapphire source.

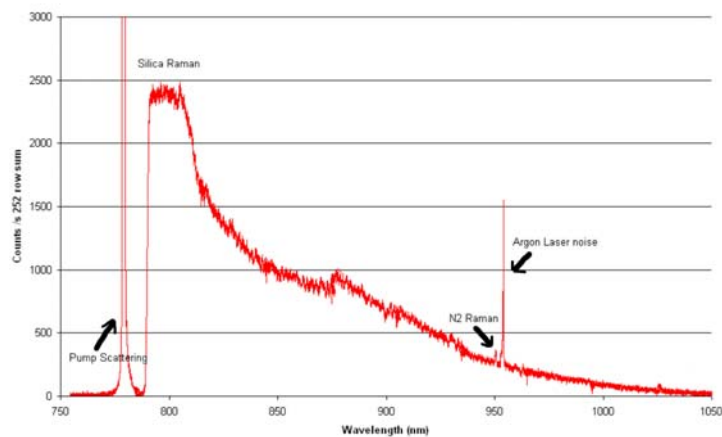


**Figure 76 - Raman spectrum from an air filled silver-lined capillary, 320 $\mu$ m ID, 1-m long, 775nm pump wavelength**

Conducting a long-wave pumping experiment allowed the identification of fluorescence being emitted by the capillary polymer coatings. It is therefore desirable to pump the capillary

with a wavelength slightly longer than the fluorescence peak to avoid excitation of this emission – i.e., longer than about 630nm. After this basic evaluation of noise, it is possible to clearly label the spectral components in the visible pumped spectrum. Figure 77 shows these labeled components in a visible-spectrum recorded with the same detector array as used in the 775nm pumped experiment.

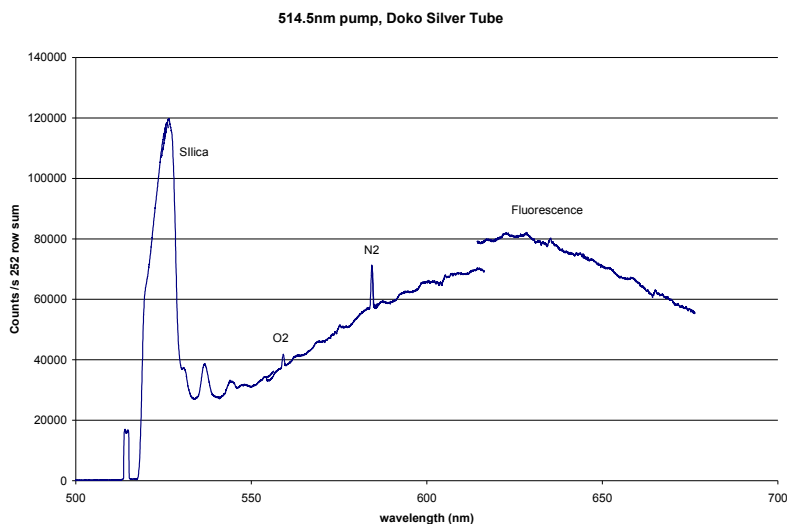


**Figure 77 - Capillary noise sources**

One final procedure was performed to clarify the sources of noise in the capillary system. This experiment involved imaging the capillary output onto the 2D array detector in order to provide a “map” of the noise emission sources in both wavelength and real space. These imaging procedures were not successful using the 514.5nm visible pump, as fluorescence appeared to obscure the clarity of images. A small 659nm solid state laser diode was obtained along with the necessary beamsplitter and filters for operation at this wavelength. The emission spectrum of this particular source is shown in Figure 78 over a range of operating temperatures. Because this pump wavelength was slightly longer than the peak in the observed fluorescence spectrum, no fluorescence was noted. The characteristic silica-Raman peaks were still present. Figure 79 shows a 2D image of the fiber output at the spectrometer’s detector plane. Again, the

X-axis represents about 35nm worth of spectral space centered on 780nm, while the Y-axis maintains the spatial picture of the capillary end-facet. The capillary was filled with 75psi pure nitrogen in order to obtain a stronger gas-Raman output and enable simpler focusing of the capillary image during alignment.

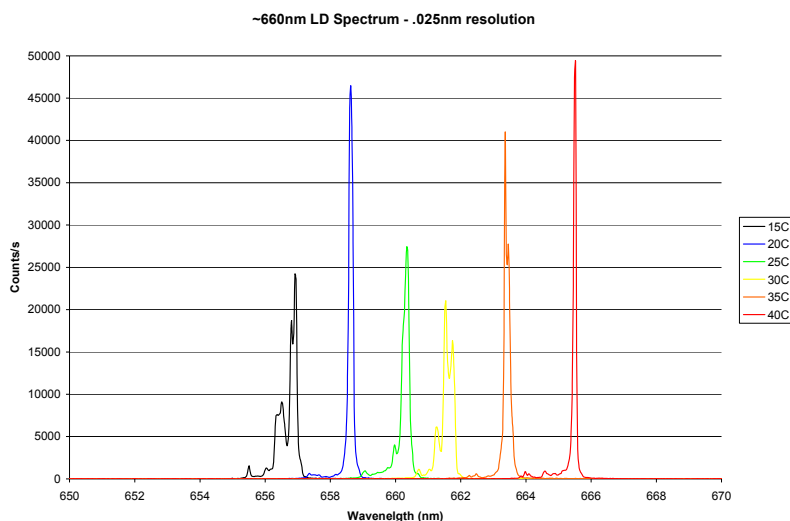


**Figure 78 - 659nm laser diode spectrum**

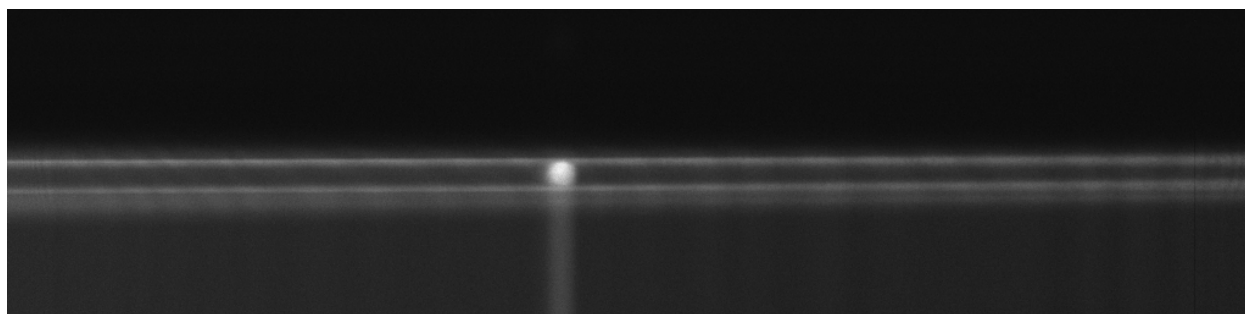


**Figure 79 - CCD array detector image of 659nm pumped, 1-m long, 320 $\mu$ m ID silver-lined capillary with 75psi N<sub>2</sub>. x-axis: wavelength, y-axis: real image space**

The features observed in Figure 79 provide excellent insight into the sources of light emitted by the capillary collector. First, the bright spot at the N<sub>2</sub> Raman line location indicates that Raman is indeed being generated in the capillary core, and is propagating therein. Second,

the two horizontal broadband lines in the image indicate that silica Raman is being emitted most strongly by the capillary walls, which themselves contain and propagate a significant portion of the silica Raman light. This is a clear indication that the silica Raman emitted by the capillary is amenable to spatial filtering, exactly as it was in the PBF case. A number of experiments were conducted using the “digital spatial filtering” technique described previously; which resulted in significant improvements in signal-to-noise ratios and smaller detection limits in most gases.

## 8.2 SUPPORT FOR CAPILLARY RAMAN THEORIES

Thus far, a great deal of theory regarding the transmission properties of metal-lined capillary waveguides has been presented. Next, we will present experiments designed to prove or disprove the theories of capillary mode propagation proposed in Chapter 7.0. These experiments included measurements of the polarization of propagating capillary modes, the angular spectrum of these modes, and the collected Raman power.

The initial assumption in our theory of Raman modes in metal guides is that the Raman modes propagate in a linearly polarized fashion. We indicated that this was probably the case given the application of a linearly polarized pump beam and the absence of any significant depolarization ratio in most gases of interest. This would theoretically result in the propagation of only the set of  $EH_{1n}$  modes, which are linearly polarized. Figure 80 is an experimental verification of the linear polarization emerging from a capillary. The Figure shows the polarization distribution of the 514.5nm radiation entering and leaving the 320  $\mu\text{m}$  diameter silver-coated capillary. A cube-polarizer (vertical pass polarization) is introduced at the output of the 514.5 nm argon laser to ensure that the laser’s output polarization is very well defined

(linear, >1000:1 polarization ratio). The top curve (red) shows the collimated capillary-output power passed through a second polarizer as that polarizer is rotated. The top (red) curve shows that the polarization of the light input to the capillary is in fact well-defined and vertical. The polarization of the light that emerges from the capillary is recorded as a second polarizer is placed at the capillary's output and is rotated. The sinusoidal variation of that curve (bottom curve, green) implies that the output from the capillary is also vertically polarized. The small non-zero minimum of this curve indicates that there is either some small amount of random scattering, or that some small portion of the total propagating power is contained in non-polarized modes. We can then infer that the capillary must be mostly propagating the linearly polarized  $\text{EH}_{1n}$  mode-set as was predicted.

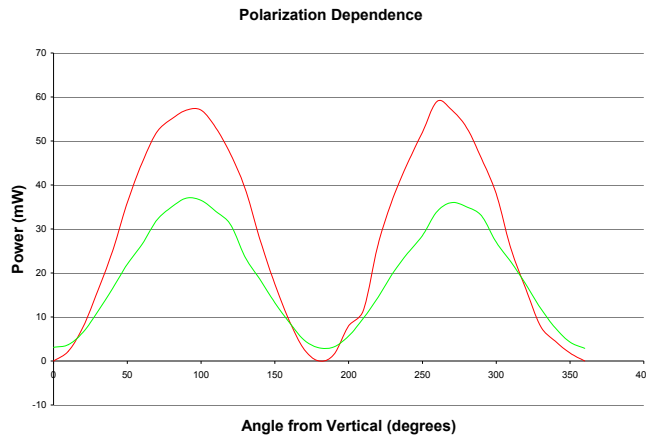


**Figure 80 - Capillary input/output polarization**

The next experiment designed to extract the physical properties of the capillary was a series of angular output measurements. The same Raman system shown in Figure 73 was constructed, with  $L_1 = 20\text{mm}$ ,  $L_2 = 75\text{mm}$ , and  $L_{\text{capillary}} = 42\text{cm}$ . A variable ruled-aperture in the collimated beam path right behind  $L_1$  allows simple measurement of the integrated Stokes Raman power versus total output angle. Even in the event that that Raman beam is not perfectly collimated via slight misplacement of  $L_1$ , placing the aperture immediately behind the lens

ensures accurate measurement of the angular output. The image of the capillary is produced on the spectrometer entrance slits with a size  $D = \frac{2af_2}{f_1} = 2a \cdot 3.75 = 2 \cdot 160\mu\text{m} \cdot 3.75 = 1.2\text{mm}$  (where  $a$  is once again the radius of the capillary core). The angular spread of the Raman output from the capillary is reduced by the same factor (3.75). This reduction in angular spread results in more of the Raman capillary angular output “fitting” into the spectrometer. Because modes exist with angles  $\theta$  up to 90 degrees, some overfilling of the spectrometer’s angular aperture still occurs. The spectrometer slits are set at 2mm wide to allow the entire capillary image ( $D=1.2\text{mm}$ ) to be collected.

The capillary was filled with pressurized (200psig) UHP methane. A 35 nm wide spectrum centered at the  $2917\text{cm}^{-1}$  methane Stokes line was detected. A noise background of fluorescence and of silica Raman produced by the glass capillary substrate was observed as in previous visible-pumping experiments. Detection integration times of 1-second were used. The signals from all of the pixels on the CCD array were summed to produce a single Stokes power plus noise measurement. The methane is then vacuumed from the capillary and the noise is measured separately and subtracted. Figure 81 is a plot of the background subtracted Stokes power versus output collection angle derived from these measurements. Also shown in Figure 81 are the results of our simulation analysis ( $L_{\text{capillary}} = 42\text{cm}$ ,  $a = 160\mu\text{m}$ ). The measured angular Stokes output matches the theoretical curve well up to about 20 degrees. Beyond that angle, overfilling of the spectrometer occurs, limiting collection of the Stokes output from the capillary.

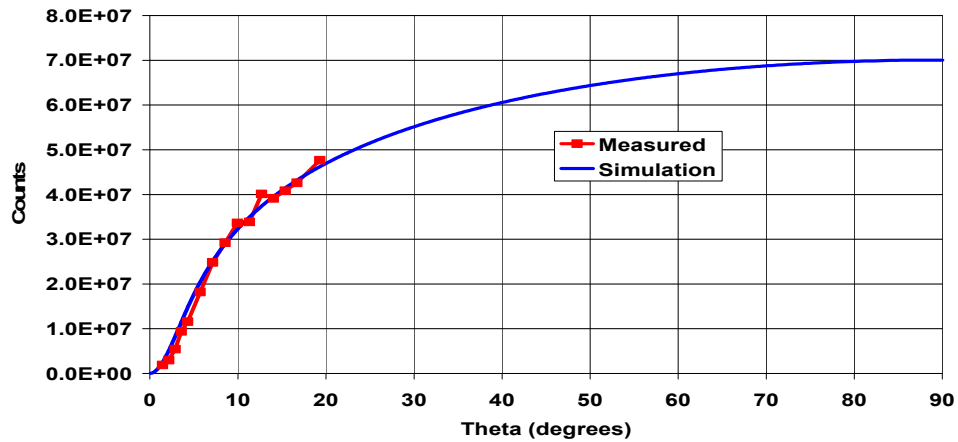


**Figure 81 - Angular dependence of collected Stokes power from a silver-lined 320 $\mu$ m ID capillary**

In general, this limited capillary experiment shows that our theory of Stokes modes inside metal waveguides is most likely accurate. It also indicates the inherent difficulty of collecting such large angles from capillary guides. Because large angles must be collected in order to efficiently utilize a capillary guide for Raman collection, the power enhancement realized using the guide itself over standard free-space Raman is somewhat diminished. Basically, the problem of omni-directional scattering has been reduced to one of large-angle collection; which presents a significant challenge, but not impossibility. Largely, the determination of which guide to use for a particular Raman system has more to do with the availability of detectors and the necessary optical resolution rather than the ideal size of guides and the theoretical maximization of collectable power.

One additional angular experiment was conducted to verify the assumed loss in pump propagation in the forward direction. To accomplish this, a  $\sim$ 633nm helium-neon laser beam was focused into a 530 $\mu$ m ID, 2m long, silver-lined capillary using a 3.1mm efl aspheric singlet. The purpose of using such a short efl pump-coupling lens was to ensure that modes propagating at large angles were excited uniformly. The input f/# of the launch is therefore about

3.1mm/~2mm = 1.55 (if the input beam is 2mm in diameter). This angular launch is wide, and should excite modes propagating up to about 18° (half angle). At the output of the capillary, a 20mm 1" diameter aspheric singlet was used to collimate the emerging HeNe beam. A variable aperture was placed in the collimated beam in front of a power meter in order to produce a plot of pump angular output for forward propagation, displayed in Figure 82 (◊ points). In the same Figure, a simulation of the forward propagating power is supplied (solid line). This simulation was performed in exactly the same way as previous calculations (characteristic equation based) for mode loss and angle were performed. In this case, all modes are assumed to be excited equally at the guide entrance, and the portion of power remaining in each mode after propagation in the guide is plotted. This is different from the case where Raman is generated along the entire length of the guide, because the Raman case allows for light generated near the output end of the guide to propagate to the output without much loss, instead of being heavily attenuated along the entire propagation length.

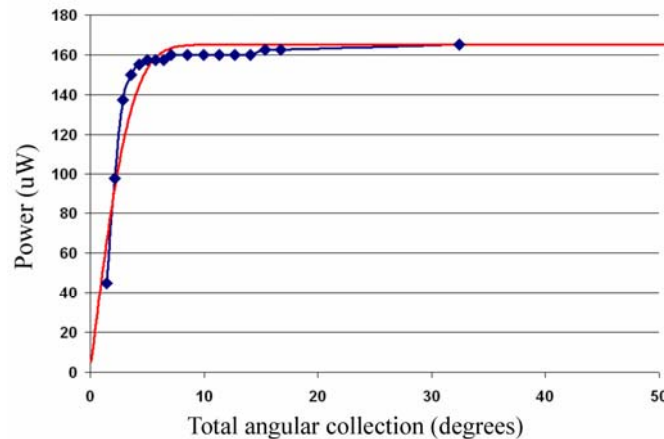


**Figure 82 - 632.8nm HeNe laser power throughput in a 530um ID 2-m long silver-lined capillary measurements are labeled with ◊ symbols, and the simulation is shown with the solid red curve.**

We observe once again that calculated losses match fairly well with experimental data in the above figure. We also can infer the reasoning behind launching the pump beam at a very

shallow angle. Above about 5 degrees, loss is extremely high (see Figure 65), and pump power does not propagate to the end of the guide. Instead, it is lost through the silver walls and leaks into the solid glass surround. The excellent agreement of these angular propagation results and our simulations, combined with the mode-polarization results, are strong evidence of the accuracy of our application of mode theory to capillary waveguides.

### 8.3 FURTHER CAPILLARY CHARACTERIZATION

To provide a more complete picture of the operational characteristics of metal-lined capillaries used as gas-Raman cells, a few more pertinent tests were conducted. Some quantitative observation of the gas-flow and filling times in various capillaries was conducted. Finally, analysis of the signal-to-noise ratios achievable in available capillaries was performed.

First, a continuous-measurement experiment was designed similar to previous PBF experiments, in which the flow characteristics of capillary waveguides could be observed via collected Raman signals. The Raman rise and fall times measured for a 1-m long, 320 $\mu\text{m}$  ID, silver capillary and a 2-m long, 530 $\mu\text{m}$  ID capillary are shown in Figure 83. The capillary was first held under vacuum and a valve was opened allowing  $\sim 150$ psi methane to fill the waveguide. Gases were later re-evacuated while the methane-Raman signal was integrated for 0.5 seconds and continuously recorded on the 2D CCD array described previously. The pump wavelength was 775 nm (from a Ti:sapphire laser) and Stokes scattering from the 2917  $\text{cm}^{-1}$  line produced a Raman output at 1001.4 nm. The fast (1-2 sec) rise time corresponds to the time required for the methane to fill the capillary. The rise time shown here provides an indication of the possible rate of signal change given constant-pressure feedstock with changing-concentration. The rise time

is similar in magnitude for either case shown in the figure, although the larger capillary did indeed prove to exhibit quicker flow under the same conditions when measured with a fast-enough measurement system. The slow (tens of seconds) fall time is the limit imposed by the vacuum pump removing the residual gases in the sealed capillary, which is a much slower procedure than one-directional flow under pressure. Again, the larger capillary is quicker to vacuum under the same conditions. We can then infer the filling or gas transfer characteristics of the capillary under any applied pressure or sample conditions as is discussed in chapter 5.

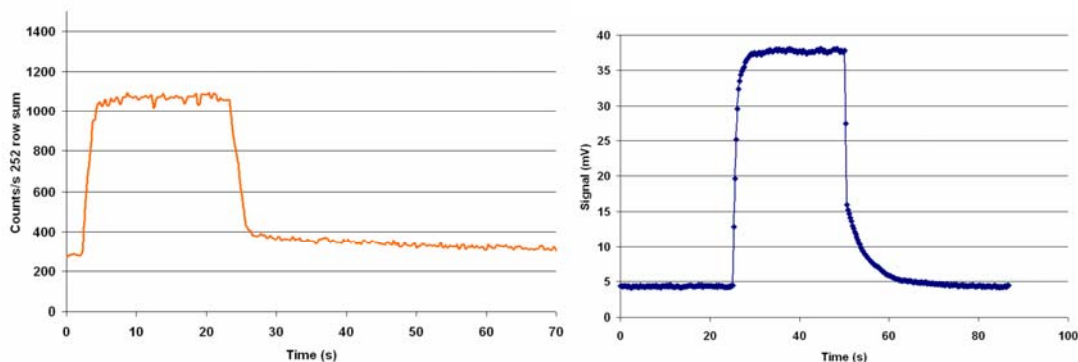


**Figure 83 - Methane Raman line rise time in silver-lined capillaries A: 320µm ID 150psi, diode array recording B: 530µm ID 200psi, single photodiode recording**

In general, the rise-times observed in the smallest of our available capillaries are quick enough to allow accurate single-second measurement of a number of species to high accuracy. A more careful analysis of the gas spectra obtained with capillary gas cells was performed in order to provide comparison between some of the particular systems we have detailed. To produce this comparison, standard “air” spectra were obtained for a number of different capillaries pumped with different wavelengths and varying spectral resolutions. The best-SNR spectra from each setup were recorded. Figure 84 shows such a sample atmospheric spectrum. The recorded spectrum was then evaluated to provide a functional description of the SNR (or more appropriately, of the ratio  $R$  defined by **Error! Reference source not found.**) in at any spectral

location. This meant first taking a vacuum spectrum of the noise background. The background was then statistically fitted with a linear relation that describes the noise level at a particular wavelength. The linear relation was then subtracted from the Raman spectrum as shown in the Figure. The equations (along with their statistical coefficients of determination:  $R^2$ ) shown in the Figure represent these linear relations. Each line in the remaining (Raman – noise) spectrum was then integrated to determine the signal level for each constituent. The average noise level was then found as the square root of the magnitude of the linear noise-fitting curve, owing to the Poisson-distribution of the noise background. Signal strengths for a number of other gases of interest were then estimated via the relative cross sections of those gases with respect to Nitrogen, which then resulted in accurate predictions of the ratio R for those gases of interest. Table 3 lists some possible detection limits based on the ratio R for different gases.

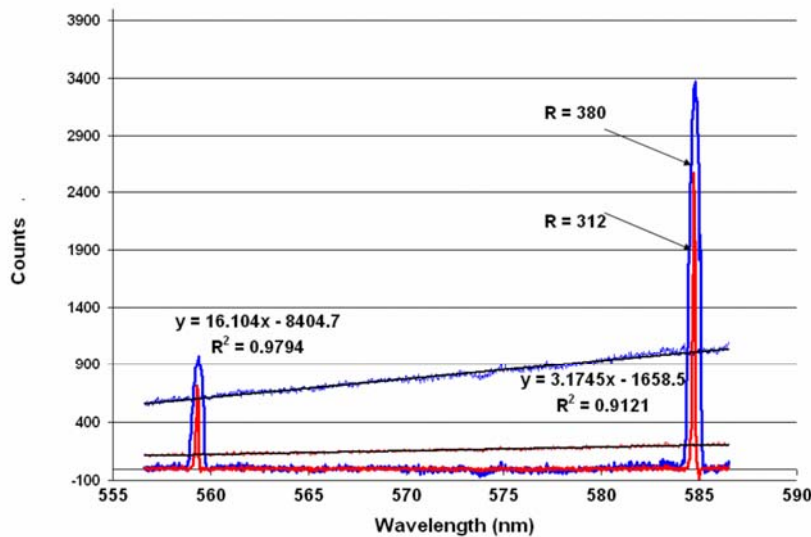


**Figure 84 - Reference 'air' spectrum for SNR determination, 100mm efl pump launch lens, linear Background Subtraction, 514.5nm Pump, 1second integration, .1mm and .5mm slits.**

Table 3 expresses some different possible detection limits for a 1-meter length of 700 $\mu$ m ID Aluminum-lined capillary pumped at 514.5nm, a 1-meter long HC-580 PBF cell pumped at 785nm, and a 1-meter length of HC-580 pumped at 514.5nm. What this basic comparison shows

is that ultimately, a good-quality large-bore aluminum capillary waveguide is usually capable of detection in the hundreds of PPM-range for most gases. Slightly better results were obtained with similar silver-lined guides. Ultimately, the capillaries tested never attained detection limits as small as those shown in best-case PBF results, but exhibited transfer characteristics well over an order of magnitude faster than their PBF counterparts.

**Table 3 - Estimated detection limits (PPM) for different systems**

<b>Gas</b>	<b>Frequency Shift (cm-1)</b>	<b>PBF HC-580 514.5 nm</b>	<b>Doko Al - 514.5 nm</b>	<b>PBF HC-800 - 785 nm</b>
<b>Methane</b>	<b>2917</b>	<b>36</b>	<b>376</b>	<b>x</b>
<b>Ethane</b>	<b>2914</b>	<b>15</b>	<b>150</b>	<b>x</b>
<b>Propane</b>	<b>2906</b>	<b>11</b>	<b>115</b>	<b>x</b>
<b>CO2</b>	<b>1388</b>	<b>580</b>	<b>1116</b>	<b>885</b>
<b>Nitrogen</b>	<b>2331</b>	<b>518</b>	<b>2106</b>	<b>4825</b>
<b>Oxygen</b>	<b>1556</b>	<b>590</b>	<b>1415</b>	<b>215</b>
<b>CO</b>	<b>2143</b>	<b>530</b>	<b>2196</b>	<b>5470</b>
<b>H2S</b>	<b>2611</b>	<b>31</b>	<b>319</b>	<b>700</b>
<b>SO2</b>	<b>1152</b>	<b>317</b>	<b>264</b>	<b>75</b>

Ultimately, we can see that metal-lined capillaries are excellent choices for Raman sensing cells requiring extremely fast gas transfer. The simple metal internal structure makes them resistant to contamination, high temperatures, and transmission loss by wear. Furthermore, numerous process applications could utilize the combination of <1second sampling and

exchange time, along with detection limits in the <0.01% range offered by the capillary configuration.

## 9.0 INSTRUMENTATION ENGINEERING

Significant progress has been made in the theoretical understanding of Raman scattering collection systems for gas spectroscopy. We have enumerated a working theory of both photonic bandgap fiber collection cells and metal-lined capillary collection cells. We have also generally detailed the gas dynamics, noise sources, and spectral response in these systems. Examinations of recorded Raman spectra show that our novel configurations provide significant improvements over traditional Raman methods. Furthermore, we have shown how a particular system can be application-designed for speed, accuracy, and resolution. Certainly, a significant case has been made for the utilization of this Raman collection technology in commercial and scientific applications. What has not been described in detail so far are the few questions regarding the conversion of these experimental systems into robust and reliable instruments.

In this chapter some of the pertinent technical details regarding the production of viable, field-ready, Raman gas sensing instruments will be discussed. First, we will review experiments conducted using PBF and extremely short wavelength (405nm) pump sources. The aim of such experiments was to increase the Raman output (by  $\omega_{\text{stokes}}^4$ ) to allow the use of less expensive front-illuminated CCDs with lower quantum efficiencies and larger dark noise, while maintaining similar detection limits as compared to the longer wavelength pump sources previously employed. In addition, the recent popularity of BlueRay DVD burners has drastically dropped the price of 405nm laser diodes, making them ideal low-cost sources for production

instruments. We will evaluate the prospect of using these short-wavelength solid-state sources in our PBF-Raman systems.

Although a great deal of effort has been spent characterizing the optical properties of novel-waveguide Raman collectors, less detail has been lavished on the dispersive detection system itself. Although dispersive spectrometers are essentially well-established technologies, we have reviewed some methods of miniaturizing or even eliminating the dispersive spectrometer portion of the spontaneous Raman collection system. While Section 3.4 covered most of the popular types of detectors used in Raman experiments, and Section 2.2 briefly described the elements of one type of dispersive spectrometer, this Chapter will suggest some innovative possible methods for making less expensive fieldable systems.

## **9.1 SHORT WAVELENGTH PUMPING**

Recent improvements in the quantum-structure of solid-state semiconductor laser diodes have allowed for the inexpensive production of near-UV (~405nm) sources. These diodes have been subject to further economy of scale price reductions due to the huge demand for high-speed BlueRay DVD burners. In a DVD burning application; high output power, fair beam quality, and short wavelengths are required for accurate inscription at high data rates. These qualities seem to correlate well to source requirements in our Raman systems.

A suitable 405nm laser diode was obtained for experimentation. The diode (Mitsubishi ML101J27-01) had a measured output power of about 100mw, and exhibits a ~2X diffraction-limited beam quality in the horizontal direction and a ~3X larger expansion in the vertical direction (than in the horizontal direction), resulting in an elliptical beam. The laser diode was

mounted on a thermo-electric Peltier-cooled mount and heatsink powered by a digitally controlled laser diode power supply and TE cooler controller (Thorlabs ITC 510). Initially, the laser diode was evaluated spectrally by scattering a small portion of the laser beam power into the spectrometer. Figure 85(a) shows the laser diode spectrum as the mount temperature was increased from 20°C to 60°C in 5 degree increments. Although the total output power changes little over this temperature range, the laser's output center wavelength shifts more than 5nm towards longer wavelengths. Part b of the same figure plots the peak wavelength as a function of diode temperature. The resultant exponential curve was subsequently used to roughly set the diode's output wavelength simply by warming or cooling the diode with the TEC. Finally, using the limited datasheet supplied with the laser diode mount TEC, a plot of mount temperature versus thermocouple resistance was produced. It is displayed in Figure 86. From this curve we can derive the relation between thermocouple resistance and mount temperature as:

$$\text{Equation 65: } T(^{\circ}C) = 62.6e^{\frac{-R}{8956}} + 4.5$$

$$\text{or, } R = -8956 \ln\left(\frac{T - 4.5}{62.6}\right)$$

Such careful characterization allows control of the diode wavelength via temperature control while using the onboard thermocouple as a reference. A similar procedure was conducted to characterize the 659nm laser diode.

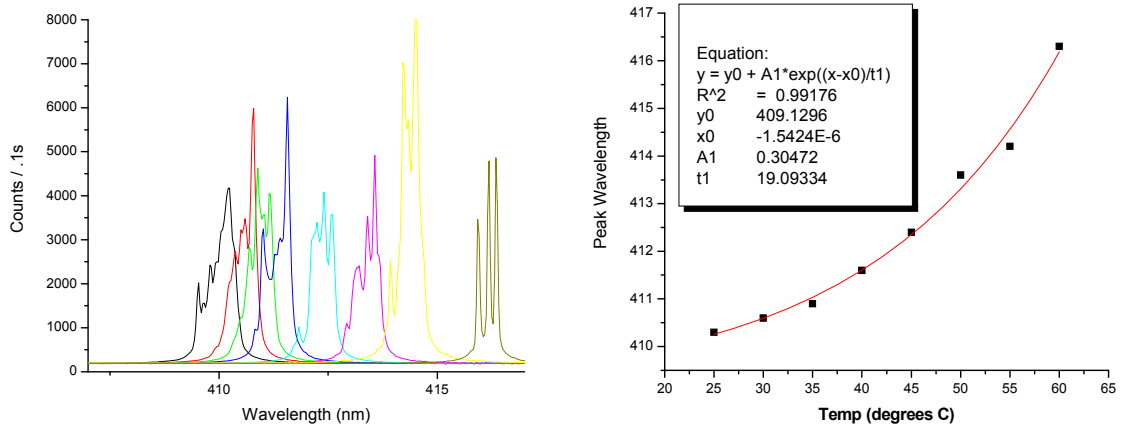


**Figure 85 - BlueRay laser diode spectra (a) and peak wavelength (b)**

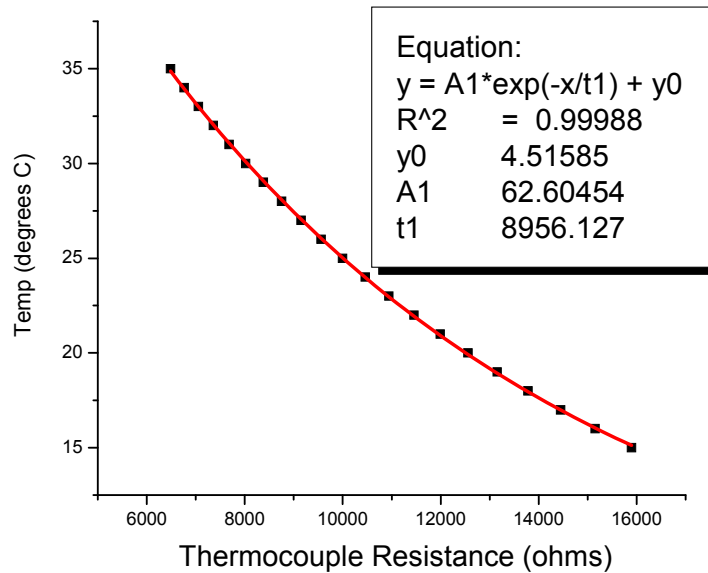


**Figure 86 - TEC temperature and thermocouple resistance**

It should also be apparent in the Figure that the linewidth of this particular diode is fairly large (~2nm) owing to the lack of wavelength stabilization in the diode. More recently, 405nm laser diodes with internal wavelength stabilization have become available. One common method of accomplishing such stabilization and line narrowing is the use of the external-prism Littrow

configuration. In such a configuration, a similarly broad-emitting laser diode is manufactured with an anti-reflection coating in place of the output coupler to extend the cavity beyond the diode package. Then, an external prism and output coupler can be added to provide precise wavelength selectivity and proper feedback for stabilization. We note that although this sort of configuration can be produced in the lab at very low cost, commercially-available wavelength stabilized 405nm lasers are currently very expensive due to lack of demand, and not mechanical complexity.

As was accomplished with a variety of other pump sources, the 405nm laser diode was next incorporated into a Raman system similar to that shown in Figure 27. The collection cell, in this case, is a 2-m length of Crystal Fibre HC-440, which exhibits a  $\sim 100\text{nm}$  wide bandgap centered on 440nm. Note that the 405nm pump emission is again nearest the left-hand (short wavelength) end of the transmission band. In this configuration, the  $4155\text{cm}^{-1}$  hydrogen Raman line should be well within the spectral bandgap. A 3.1mm aspheric lens was used to collimate the laser diode beam. Although a more Gaussian (round) beam can be produced from an elliptically-emitting diode by using a combination of 2 cylindrical lenses, this technique was determined to be less practical due to the space limitations imposed by the laser diode mount. After being directed through a  $\sim 2\text{nm}$  bandpass line-filter, the pump beam was reflected off of a dichroic beamsplitter, through a 25mm focusing asphere, and into the 2-m fiber. Backscattered Raman was focused into the 0.2mm spectrometer slits using a 6cm singlet. This produced a  $\sim 2.4\text{X}$  magnified image of the fiber end facet on the 2D CCD array. Figure 87 shows the resultant Raman spectrum with the fiber filled with only ambient atmosphere.

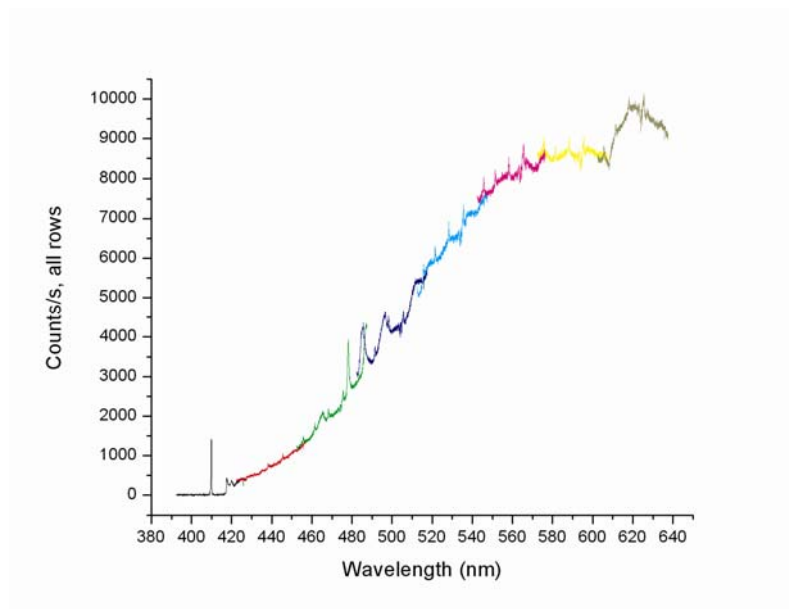


**Figure 87 - Initial 405nm pumped Raman spectrum in PBF (no gas-Raman lines discernable)**

Features present in this figure seem to indicate some significant problems with utilization of this particular source. Firstly, a series of evenly-spaced narrow peaks exists throughout the transmission band. These were later determined to be spontaneous emissions from the laser diode, which were of intensity large enough to obscure Raman signals, even in the presence of the laser-diode bandpass cleanup filter used to mitigate this response. Most importantly, the main characterizing feature of this spectrum is the large, continuous background peaking near ~620nm. As we have observed in the case of metal-lined capillaries pumped with green light, the background is due to the fluorescence of some component of the PBF itself. Although more testing would be required to determine the nature of the fluorescence, it is believed that the plastic fiber jacket contributes a significant amount of fluorescence to the spectrum.

We were, however, also interested in determining whether or not some quantity of silica Raman was being collected. It was therefore necessary to firstly eliminate most of the laser's spontaneous emission in order to clearly view any possible remaining spectral peaks for identification. In a very rudimentary experiment, the collimated laser beam was reflected off of

a 600 groove/mm linear dispersion grating. The 1<sup>st</sup> order beam was directed through a small aperture for wavelength selection. This technique was successful in eliminating the majority of spurious spontaneous emissions, but did not stabilize the peak power near the center wavelength. Figure 88 shows a portion of the resultant Raman spectrum obtained with the PBF filled with only ambient air, but this time filtering out the extra laser-produced spontaneous emission and “digitally” spatial filtering the output CCD image to eliminate a large portion of the fluorescence signal noted to propagate outside the fiber core. This Figure illustrates the clear presence of a silica Raman band because the most prominent peaks align with known Raman transitions corresponding to the bending and stretching modes of the silica molecules. The Raman peak from oxygen is difficult to distinguish in the figure, because optical alignment was performed using the silica Raman peak near ~425nm. Significant chromatic aberration in the coupling lens tends to cause de-focusing of Raman peaks spaced farther from the peak used for alignment. This problem is easily rectified by using a desired Raman peak for optical alignment instead of the silica Raman peaks. Indeed, focusing was conducted in this way only to provide a clear picture of the silica Raman peaks in the figure, and not of the gas-Raman signatures.

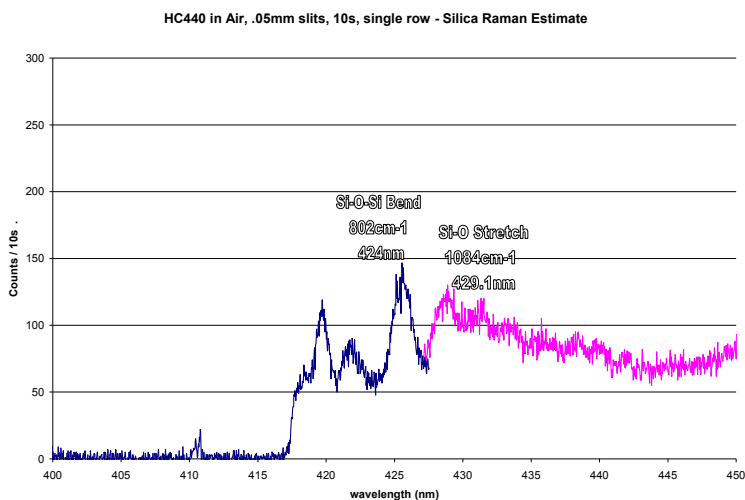


**Figure 88 - Silica Raman noise in HC-440 fiber**

In addition to aiding in the determination of the presence of silica Raman, the previous setup (utilizing a diffraction grating for LD cleanup) resulted in clearly observable Raman peaks from the Nitrogen and Oxygen present in the atmosphere when alignment was performed using the nitrogen-Raman line. These peaks are shown in the spectrum in Figure 89. Note that the Raman peaks appear similar in linewidth to the pump diode. Because the pump wavelength is rather broad, the Raman peaks appear slightly broader, which has adverse effects on the resolution and sensitivity of the detection system.

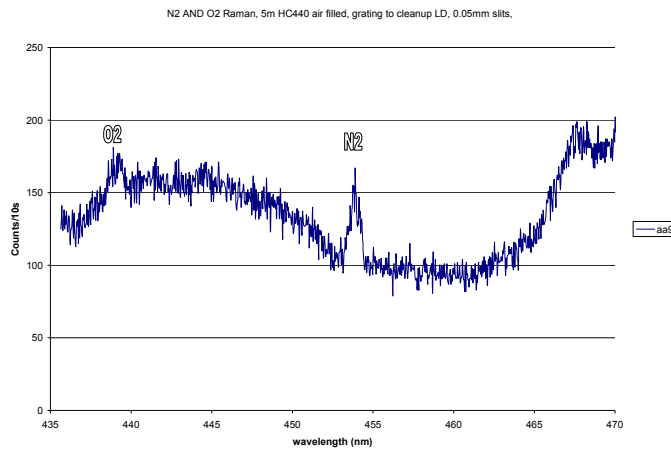


**Figure 89 - Atmospheric Raman inside HC-440 with a ~405nm pump**

In general, we can draw some conclusions from the simple atmospheric results garnered from these experiments. First, we can ascertain that collection in this particular configuration is not very efficient. This is primarily due to high transmission losses in the HC-440 fiber at the pump wavelength. Additionally, poor mode quality in the pump-mode results in lower coupling efficiency, and consequently higher background noise from silica Raman and plastic fiber-jacket fluorescence. Although there could be significant theoretically-attainable improvements in detection SNR using 405nm lasers, the available HC-440 fiber and low-cost laser diode utilized in these experiments were not capable of realizing such improvements. If the fiber losses could be reduced through better design and/or process control, along with improvements in the laser

source linewidth and noise without drastically increasing the cost; then a viable system may be producible at this wavelength.

## 9.2 SPECTROMETER ALTERNATIVES

In our preceding treatises on light collection, we have primarily dealt with the prospect of coupling collected Raman light into a linearly dispersive spectrometer, usually of the holographic or ruled dispersion-grating type. This approach was taken primarily because it embodies the traditional methodology for spectral measurement. In constructing a portable Raman instrument, the generally large physical dimensions of a traditional spectrometer are prohibitive. Additionally, the high cost of such an instrument is a large portion of the cost of a complete Raman sensing system; imploring us to seek its replacement with a simpler device. We will therefore look briefly at some possible alternatives for spectral discrimination without the use of a full-fledged moving-grating dispersive spectrometer.

Recently, miniature dispersive spectrometers have become available that purport lower costs, no moving parts, and customer-specified operating parameters. It is indeed possible to implement the standard Czerny-Turner configuration shown in Figure 10 in a relatively small package. By simply employing a shorter internal focal length, the instrument size can be reduced. Of course, this also has the effect of decreasing spectral resolution. Using a fixed dispersion grating instead of a movable grating eliminates the need for complicated control electronics and accurate grating-positioning systems, although it fixes the observable wavelengths to a small range. A fixed-grating spectrometer also requires multi-channel detection, with each channel measuring a fixed portion of the spectrum. CCD arrays are

commonly used for this purpose as they provide both large detection areas and small pixel sizes. This arrangement will essentially fix the spectral detection range to a small window determined by the size of the CCD employed, the spectrometer focal length, and the grating dispersion. Still, little more is required for such a construction than input and output apertures (slits), a fixed dispersive element, and a CCD detector. Usually, small commercial systems provide fiber-optic inputs in order to delimit the angular acceptance to that of the fiber, as well as simply using the fiber's core as the input aperture.

In our Raman gas-sensing system, extensive characterization measurements were made using a laboratory-quality  $\frac{1}{2}$  meter spectrometer and an assortment of detectors. To demonstrate the portability of the proposed system, the larger spectrometer was replaced with a  $\sim 100$ mm efl  $f/4$  Ocean Optics Miniature Spectrometer (HR4000). This experiment was performed by Dr. Steven Woodruff (NETL, Morgantown) as part of an ongoing collaboration in instrumentation development. The spectrometer utilized therein operates in the Czerny-Turner configuration, although the dispersed and un-dispersed light-paths are crossed in order to make the system fit in a small ( $\sim 150$ mmX $100$ mm) package. In reviewing the various possible hollow waveguides for use with such a detection system, it was determined that metal-lined capillaries operated best with low detection-resolution, due to the large size of the capillary bore and the large Raman-angles collected. In such systems, if a large portion of the capillary-emitted Raman power is to be collected, the entrance aperture size or angle must also be correspondingly large as was determined in Chapter 7.0 . It was possible, with  $3/2$  demagnification, to couple a  $300\mu\text{m}$  bore diameter, one-meter long, silver lined capillary output image to the Ocean Optics spectrometer using a  $200\mu\text{m}$  core-diameter multimode fiber after pump light removal had been performed with a long-pass filter. The fiber had the additional affect of filtering some silica Raman noise

emitted from the solid-glass region of the capillary due to limited spatial collection of the output image similar to the “digital spatial filtering” technique described previously.

Figure 90 shows a 532nm pumped sample spectrum of methane, ethane, and propane as recorded with the Ocean Optics spectrometer. The strongest Raman lines emitted by these gasses are found near  $2900\text{cm}^{-1}$ . Although the source linewidth was extremely narrow ( $<10\text{cm}^{-1}$ ), the Raman spectra appear as spectrally-broad overlapping peaks. This is primarily the effect of the low detection resolution realized with this particular spectrometer. Fortunately, a few Raman lines do exist that do not significantly overlap outside this spectral region. Still, the lower resolution implies increased detection limits and smaller signal-to-noise ratios, making unknown sample detection more difficult.

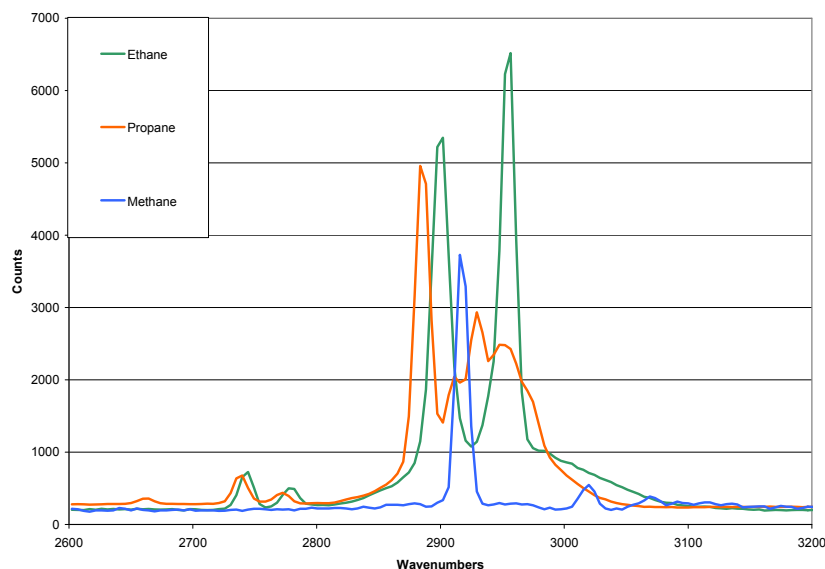


**Figure 90 - Example gas-Raman spectrum recorded on a miniature spectrometer [79]**

In the presence of overlapping spectra while using low-resolution spectrometers, some techniques are known for the separation of a composite spectrum into spectra representative of each component present. This process is generally known as “Principal Component Analysis”

(PCA) [57]. Although there are many applications (including image processing and data compression) of PCA, we will discuss a short example detailing the analysis of a mixed-gas Raman spectrum. Firstly, we must obtain the Raman spectra of individual pure gasses for reference. These spectra can be obtained from theoretical knowledge of electronic structure or more simply from experimental data taken with gas standards. This step is not necessary to conduct the component analysis mathematically, although it is necessary for the identification of resultant separated spectra.

Mathematically, the separation of such a spectrum is rather simple, and can most likely be performed on continuously acquired spectra in real-time. First, it is beneficial to remove the background portion of a spectrum. This step is usually accomplished simply by vacuuming the collection waveguide of any gasses and recording a spectrum of the empty waveguide for subtraction from subsequent sample spectra. We can then introduce our unknown gaseous sample and record a spectrum. The mean is then subtracted from the resultant spectral data in order to produce a spectrum with zero-average intensity. The covariance matrix of the spectrum is then calculated. For 1-D spectra (i.e., simple intensity versus wavelength plots without spatial information) the covariance matrix will be  $2 \times 2$  in size. Next, the Eigenvalues and Eigenvectors of the covariance matrix are determined. The Eigenvalues are then arranged from largest to smallest. The largest Eigenvalue represents the largest or Principal Component. We can now generate a “feature matrix” which contains rows of Eigenvectors in the same order as their corresponding descending Eigenvalues. By multiplying the original data with each row of the new feature matrix, we can produce individual spectra representative of each gaseous component. By statistically comparing each resultant spectrum (by sum of squared error, etc) to each of our reference spectra, we can identify the detected components by name. By dividing the

Eigenvalues of components by their corresponding Raman cross sections, we can produce a vector containing the actual concentration of each component. Thus, with a few simple mathematical steps, we can extract the concentrations of gaseous components present in a mixture with overlapping Raman lines. Furthermore, this technique has the added benefit of extracting each of the contributing spectral components in a mixture, regardless of whether or not its presence is recognized a priori. If an unknown component is present, the user is immediately aware of its spectral content, and can proceed to classify it according to Raman spectral databases or additional experimentation.

Despite the attractive features found in small fixed-grating spectrometers and the use of PCA to compensate for their poor resolution, unit costs are still somewhat prohibitive given that miniature spectrometer units cannot currently be purchased for less than a few-thousand dollars. Because numerous applications could benefit from Raman spectroscopy if costs were significantly reduced, we will suggest one additional method for spectral measurement in a simplified instrument. The natural-gas fired turbine control-application which largely encouraged this project is one such example. Therein, the monitoring of only 3-5 gases is necessary for accurate turbine control. In the situation where only 3-5 spectral lines are of interest, one should begin to doubt the necessity for any sort of linear dispersion instrument. Herein, we propose the use of a system of holographic beamsplitters instead of a complicated dispersive instrument.

Throughout this work, there has been extensive use of holographic beamsplitters for backscattered Raman collection. For Stokes collection, a long-pass  $45^\circ$  beamsplitter is used. This element passes longer wavelengths with high transmission at  $45^\circ$ , while reflecting shorter wavelengths at the same angular incidence. This has allowed us to introduce a pump beam in the

backward propagating direction while passing forward scattered Raman into the detection equipment. Figure 91 shows a proposed detection system utilizing a series of these sorts of holographic beamsplitters to efficiently separate Raman lines and direct them towards individual detectors. Therein, each diode detector receives the Raman scattering from a single gas transition. The bandwidth of each reflecting beamsplitter should be spectrally equal to the width of the Raman line for the best SNR. Instead of using band-reflection beamsplitters for each gas, it is also possible to simply use long pass beamsplitters. This option makes it more likely that non-target lines will be detected by a particular detector, but may reduce costs significantly. It should also be noted that a setup like this one lends itself well to a MEMS implementation with the possible integration of pump source, waveguide, beamsplitters, and detectors on a single substrate.

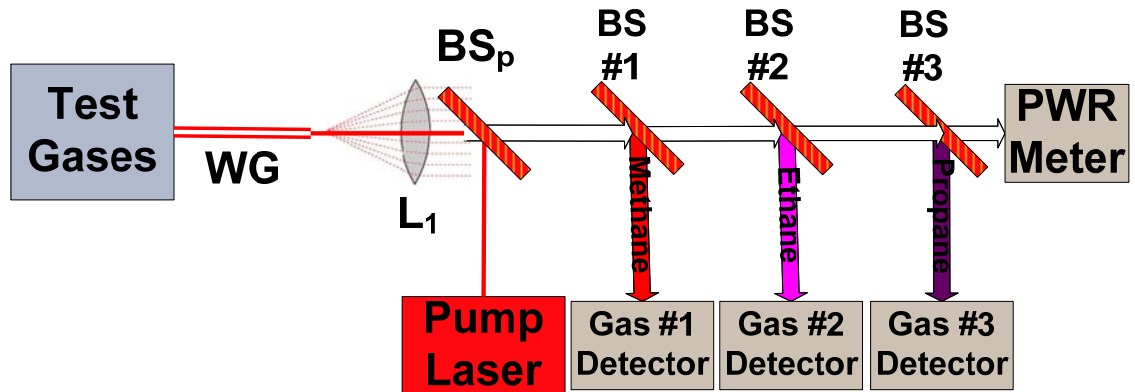


**Figure 91 - Multi-line gas Raman detection without a spectrometer**

Although a system as specific as the one shown in Figure 91 was not constructed, a simpler single-gas axial spectrometer-less system was constructed to illustrate proof of the concept. Therein, a single 90°-transmission 15nm bandwidth bandpass filter centered at 605nm was used to separate the principal methane line from the rest of the spectrum. This filter was again used in conjunction with the same beamsplitter and long-pass (pump rejection) filters used in previous visible experiments. The pump source was a 514.5nm argon-ion laser and the

waveguide used was a silver-lined 45cm long 320 $\mu$ m I.D. capillary. At the filter output, a cooled silicon photodiode was used to record the collected intensity without any spectrometer. This setup allows 15nm worth of bandwidth around the methane-Raman line of interest to reach the diode. Obviously, this system would not exhibit adequate precision to separate closely spaced hydrocarbon lines, although it could be used as a simple and inexpensive methane/air mixture controller with poor rejection of other species. In the following Figure, the silicon diode detector's response to methane pressure in the capillary is shown. Also shown for comparison is the response resultant when the spectrometer is used as the measurement system without the bandpass filter. The slit widths in that case imply a bandpass through the spectrometer about 3nm wide.

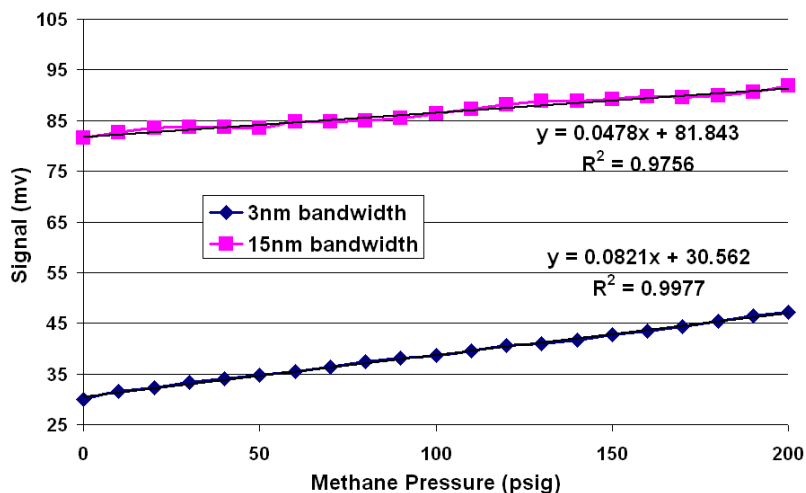


**Figure 92 - Spectrometer-less instrument operation with methane.  $\diamond$  -data points recorded with the spectrometer operating with a 3nm bandwidth.  $\square$  - data points recorded without the spectrometer using a 15nm bandpass filter**

Notably, the above Figure tells us about the issues arising from implementing a spectrometerless filter-based system. The signal-to-noise ratio becomes significantly worse when using a bandpass filter that is much broader than the Raman line of interest. This is

observed at the Y-axis crossing (zero methane pressure) where all contributions are from silica or fluorescence noise. When the bandwidth of the pass-filter is similar to the bandwidth of the spectrometer, then the same SNR is expected from either system, given similar grating and filter throughput. In practice, the throughput of a holographic filter can be significantly higher than that of a well-designed grating spectrometer. Currently, it seems that a commercial system designed to measure only a few gases could employ specially-designed filters with extremely narrow bandwidths and high pass-band transmission, resulting in a lower-cost and higher-sensitivity system than a comparable spectrometer-based instrument. Most importantly, such filters are only a fraction of the cost of a full-fledged dispersive spectrometer. Although there are a few other systems of conducting spectral measurement (including tunable fiber-optic filters like FBGs, acoustically tunable free-space filters, absorptive glass filters, etc), it is likely that these simple dielectric filters may provide the lowest cost solution for a simple Raman system.

### **9.3 CONCLUSIONS AND SUMMARY**

Up to this point in history, the detection and characterization of gases has proposed a daunting challenge to researchers and scientists. Although numerous methods have emerged to conduct such analysis, none of them clearly has the ability to deduce the concentrations of an assortment of similar molecules such as hydrocarbons and diatomics in a mixture in real-time. We have shown that this task is well suited to Raman spectroscopy, although the minute Raman cross sections of most gases of interest have historically prevented the effective use of Raman in such applications.

The laws governing scattered light collection have long imposed a seemingly insurmountable challenge to increasing Raman signals. We have shown that novel hollow waveguides like photonic bandgap fibers and metal-lined capillaries used as the gas cell and Stokes light collector are indeed capable of collecting more scattered light than any previously known collection method. Furthermore, we have shown how these waveguides can be used to increase detection sensitivity, decrease detection time, and allow previously impossible Raman measurements to be made. It is our ambition that this new technology be used to allow Raman instrumentation to replace old inefficient gas detection systems throughout the industrial and scientific sector. Furthermore, we believe that exploration of the suggestions provided herein for miniaturization and cost reduction will eventually enable these Raman instruments to be used for much simpler applications. In that reasoning, it seems that applications like automotive engine diagnosis and control, operating room anesthetic breathing analysis, industrial smoke stack emissions recording, transformer oil dissolved gas analysis, most gas chromatography applications, the detection of biological and chemical agents, mine safety devices, and environmental monitors could all benefit from our Raman system.

In the extensive operational examination of our experimental Raman systems, we have uncovered a number of interesting problems with, and solutions for realizing this technology. Because each different waveguide type was evaluated independently, we were able to suggest methods for operational implementation and the mitigation of undesirable features of the different waveguides. Furthermore, we were able to suggest preferred embodiments of each system, with the suggestion of appropriate applications with respect to speed and accuracy. Even after such extensive characterizations, there are numerous aspects of the Raman system which could be additionally improved upon to produce a better sensing instrument. Ultimately, the

sensitivity, resolution, and accuracy of such systems will be determined on a case by case basis. While we have shown that these operational characteristics are, for the most part, theoretically calculable, and have provided measurements of the pertinent characteristics of several laboratory test-systems; exact measurement of the response of every possible waveguide collection apparatus is neither necessary nor possible. The Raman gas sensing research provided herein will serve as a complete and robust background for the construction of utilitarian Raman instruments free from the high costs and technical difficulties previously preventing the widespread use of Raman spectroscopy in science and industry.

## BIBLIOGRAPHY

1. D.A. Long, "Raman Spectroscopy", McGraw-Hill, 1977
2. J. Kiefer, T Seeger, S Steuer, S Schorsch, M C Weikl, A Leipertz, "Design and characterization of a Raman Scattering – based sensor system for temporally resolved gas analysis and its application in a gas turbine power plant," Meas Sci Technol 19 (2008), 085408
3. Scott, R.P., "Introduction to Analytical Gas Chromatography", Dekker, 1998
4. Jasinski, P., "Solid State Electrochemical Gas Sensors", Materials-Science Poland, Vol. 24, No.1, 2006
5. Stern, E.S., Timmons, J.C., "Introduction to atomic absorption spectroscopy in organic chemistry", Wiley, 1997
6. R. L. McCreery, Raman Spectroscopy for Chemical Analysis, Wiley-Interscience, (1977)
7. P. Roberts, F. Couny, H. Sabert, B. Mangan, D. Williams, L. Farr, M. Mason, A. Tomlinson, T. Birks, J. Knight, P. St. J. Russell, "Ultimate low loss of hollow-core photonic crystal fibres", Optics Express, 13, 236 (2005)
8. P. Russell, IEEE LEOS Newsletter, 21, 11, (October 2007)
9. A. M Zheltikov, "Ultrashort light pulses in hollow waveguides", Physics-Uspekhi, 45, 687, (2002)
10. S. Sensarn, S.N Goda, G.Y. Yin, S.E. Harris, "Molecular modulation in a hollow fiber", Optics Letters, 31, 2836, (2006)
11. M.Nisoli, S. De Silvestri, O. Svelto, "Generation of high energy 10fs pulses by a new pulse compression technique" Appl. Phys. Lett., 68, 2793 (1996)
12. R. B. Miles, G. Laufer, G.C. Bjorklund, "Coherent anti-stokes Raman scattering in a hollow dielectric waveguide", Appl. Phys. Lett., 30, 417, (1977)

13. A.M. Burzo, A.V. Chugreev, A.V. Sokolov, "Optimized control of generation of a few cycle pulses by molecular modulation", *Optics Communications*, 264, 454, (2006)
14. S. M. Howdle, K. Stanley, V.K. Popov, V.N. Bagratashvili, "Can high-pressure Raman spectroscopy be simplified? A microscale optical-fiber capillary cell for the study of supercritical fluids", *Applied Spectroscopy*, 48, 214, (1994)
15. S.O. Konorov, A.B. Fedotov, A.M. Zheltikov, R.B. Miles, "Phase-matched four-wave mixing and sensing of water molecules by coherent anti-stokes Raman scattering in large-core-area hollow photonic-crystal fibers", *JOSA. B.*, 22, 2049, (2005)
16. A.B. Fedotov, S.O. Konorov, V.P. Mitrokhin, E.E. Serebryannikov, A.M. Zheltikov, "Coherent anti-Stokes Raman scattering in isolated air-guided modes of a hollow-core photonic-crystal fiber", *Physical Review A* 70, 045802, (2004)
17. S. D. Schwab, R.L. McCreery, "Remote, long-pathlength cell for high-sensitivity Raman spectroscopy", *Applied Spectroscopy*, 41, 126, (1987)
18. M.J.Renn, R. Rastel, "Particle manipulation and surface patterning by laser guidance", *Vac. Sci. Technol. B.* 16, 3859 (1998)
19. R. Paster, A. Sturthers, R. Ringle, J. Rogers and C. Rohde, " Laser trapping of microscopic particles for undergraduate experiments", *Am. J. Phys.* 68, 993 (2000)
20. A.Yariv, P. Yeh, "Optical Waves in Crystals", Wiley-Interscience, 1984
21. C. C. Gregory, "Attenuation, modal, and polarization properties of  $n < 1$ , hollow dielectric waveguides", *Applied Optics*, 32, 5302, 20 September 1993
22. E.A.J. Marcatili and R.A. Schmeltzer, "Hollow metal and dielectric waveguides for long distance optical transmission and lasers", *Bell Syst. Tech. J.* 43, 1783, 1964
23. P. Russell, "Photonic Crystal Fibers", *Science*, 299, 358, (2003)
24. F. Benabid, G. Antonopoulos, J.C. Knight and P. St. J. Russell, " Stokes Amplification Regimes in Quasi-cw Pumped Hydrogen-Filled Hollow-Core Photonic Crystal Fiber", *Phys. Rev. Lett.*, 95, 213903 (2005)
25. T. Ritari, J. Tuominen, H. Ludvigsen, J. C. Petersen, T. Sorensen, T.P. Hansen and H.R. Simonsen, "Gas sensing using air-guiding photonic bandgap fibers", *Optics Express*, 12, 4080 (2004)
26. P. Russell, "Photonic Crystal Fiber: Finding the Holey Grail", *OPN*, 18, 26, (2007)

27. F. Benabid, J. C. Knight, G. Antonopoulos, and P. St. J. Russell  
“Stimulated Raman Scattering in a hydrogen filled hollow-core photonic crystal fiber”,  
Science Vol. 298, 399, Oct. 2002
28. Shu-Guang Li, Si-Ying Liu, Zhao-Yuan Song, Yin Han, Tong-Lei Cheng, Gui-Yao Zhou,  
and Lan-Tian Hou, “Study of the sensitivity of gas sensing by use of index-guiding photonic  
crystal fibers”, Applied Optics, 46, 5183-5188 (2007)
29. W. Fenner, H. A. Hyatt, J. M. Kellam, S.P.S. Porto, “Raman cross section of some simple  
gases”, JOSA, 63, 73 (1973)
30. A. Yariv, “Quantum Electronics”, 3rd ed., Wiley 1989
31. M. M. Carrabba, K. M. Spencer, C. Rich, D. Rauh, “The utilization of a holographic Bragg  
diffraction filter for Rayleigh line rejection in Raman spectroscopy”, Appl. Spectroscopy, 44,  
1558 (1990)
32. S.O. Konorov, C.J. Addison, H.G. Schulze, R.F.B. Turner, M.W. Blades, “Hollow-core  
photonic crystal fiber-optic probes for Raman spectroscopy”, Optics Letters, 31, 1911 (2006)
33. Evett, Cheng, and Liu, “Fundamentals of Fluid Mechanics”, McGraw-Hill, 1987
34. J. Henningsen, Hald, J. “Dynamics of gas flow in hollow core photonic bandgap fibers”,  
Applied Optics, 47, 2790 (2008)
35. B.E.A. Saleh and M.C. Teich, “Fundamentals of Photonics”, 2nd ed. Wiley-Interscience,  
2007
36. M.P. Buric, K.P. Chen, J. Falk and S.D. Woodruff, “Enhanced spontaneous Raman scattering  
and gas composition analysis using a photonic bandgap fiber”, Applied Optics, 47, 4255,  
August 10, 2008
37. X. Cao, C.N. Hewitt, “Detection methods for the analysis of biogenic non-methane  
hydrocarbons in air”, Journal of Chromatography A, 710 (1995) 39-50
38. M.R. Beychok, “Coal gasification and the Phenosolvan process”, American Chemical  
Society 168th National Meeting, Atlantic City, September 1974
39. N.V. Wilding, P.S. Light, F. Couny and F. Benabid, “Experimental comparison of  
electromagnetic induced transparency in acetylene-filled kagomé and triangular lattice  
hollow core photonic crystal fiber”, CLEO 2008 paper JFA3, May 9, 2008
40. V. Shahraam Afshar, Y. Ruan, S.C. Warren-Smith, and T.M. Monro, “Enhanced  
fluorescence sensing using microstructured optical fibers: a comparison of forward and  
backward collection modes”, Optics Letters, Vol. 33 Issue 13, pp.1473-1475 (2008)

41. HC-580 HC-PBF datasheet, retrieved September 3, 2008 from <http://www.i-waveco.com/category/pdf/5131-HC58001.pdf>
42. HC-800-01 HC-PBF datasheet, retrieved November 3, 2008 from <http://www.crystal-fibre.com/datasheets/HC-800-01.pdf>
43. Semrock beamsplitter data sheet. Downloaded from <http://www.semrock.com/Catalog/RamanEdgeDichroic.htm>, July 23, 2008
44. J. J. Barrett and N. I. Adams, III, “Laser-Excited Rotation-Vibration Raman Scattering in Ultra-Small Gas Samples”, Journal Optical Society of America, Vol. 58, No. 3, March 1968
45. Joannopoulos, J., Johnson, S., Winn, J., Meade, R., “Photonic Crystals, molding the flow of light”, Princeton, 2008
46. [http://en.wikipedia.org/wiki/File:Raman\\_energy\\_levels.jpg](http://en.wikipedia.org/wiki/File:Raman_energy_levels.jpg), March 20, 2006
47. Buric, M.P, Falk, J., Chen, K., Woodruff, S., “Improved sensitivity gas detection by spontaneous Raman scattering”, Applied Optics, submitted December 2008
48. Benabid, F., Hollow-core photonic bandgap fiber – New light guidance for science and technology”, Philosophical transactions of the Royal Society, 2006
49. Semrock filter datasheet. Downloaded from [http://www.semrock.com/Data/Spectra/LP02-514RE\\_Spectrum.txt](http://www.semrock.com/Data/Spectra/LP02-514RE_Spectrum.txt) July, 2008
50. <http://upload.wikimedia.org/wikipedia/en/e/e8/Czerny-turner.png>, January, 2010
51. Walrafen, G.E., Stone, J., “Raman spectral characterization of pure and dopes fused silica optical fibers”, Applied Spectroscopy, Vol. 29, No. 4, 1975
52. Electro-optic-Systems datasheet. Downloaded from: [http://www.eosystems.com/pdf/spectral\\_response\\_uv\\_s\\_ge\\_iga.pdf](http://www.eosystems.com/pdf/spectral_response_uv_s_ge_iga.pdf)
53. PMT diagram. Downloaded from <http://www-hep2.fzu.cz/roznov/SiliconPhotomultiplier/Read%20Out%20of%20Scintillation%20Crystals.htm> November, 2008
54. Burle Ind., “Photomultiplier Handbook”, downloaded from: <http://www.burle.com/cgi-bin/byteserver.pl/pdf/Photo.pdf>, November, 2008
55. Eg&G Model 1121 Discriminator manual, Princeton Applied Research Corp., 1976
56. Charge Coupled Device Theory Brief, University of Toronto, downloaded from: <http://www.astro.utoronto.ca/~bridge/handouts/ccd.pdf>, November, 2008

57. Smith, Lindsay, "A tutorial on principal component analysis"  
[http://www.cs.otago.ac.nz/cosc453/student\\_tutorials/principal\\_components.pdf](http://www.cs.otago.ac.nz/cosc453/student_tutorials/principal_components.pdf), January 1, 2010
58. Abe, Y., Matsuura, Y., Shi, Y., Wang, Y., "Polymer-coated hollow fiber for CO<sub>2</sub> laser delivery". *Optics Letters*, Jan. 1998m Vol. 23, No. 2
59. Abe, Y., Shi, Y., Matsuura, Y., and Mitsunoba, M., "Flexible small-bore hollow fibers with an inner polymer coating", *Optics Letters*, Feb. 2000, Vol. 25, No. 3
60. Komachi, Y., and Sato, H., "Raman probe using a single hollow waveguide", *Optics Letters*, Nov. 2005, Vol. 30, No. 21
61. Matsuura, Y., and Hanamoto, K., Sato, S., and Miyagi, M., "Hollow-fiber delivery of high-power pulsed Nd:YAG laser light", *Optics Letters*, Dec. 1998, Vol. 23, No. 23
62. Matsuura, Y., Saito, M., and Miyagi, M., Hongo, A., "Loss characteristics of circular hollow waveguides for incoherent infrared light", *J. Optical Society of America A*, March 1989, Vol. 6, No. 3
63. Matsuura, Y., Takada, G., Yamamoto, T., Shi, Y., Mitsunobu, M., "Hollow fibers for delivery of harmonic pulses of Q-switched Nd:YAG lasers", *Applied Optics*, Jan. 2002, Vol. 41, No. 3
64. Matsuura, Y., Shi, Y., Abe, Y., Yaegashi, M., Takada, G., Mohri, S., Miyagi, M., "Infrared-laser delivery system based on polymer-coated hollow fibers", *Journal of Optics and Laser Technology*, 2001, Vol. 33, pp. 279-283
65. Matsuura, Y., and Miyagi, M., "Hollow optical fibers for ultraviolet and vacuum ultraviolet light", *IEEE Journal of Quantum Electronics*, Nov/Dec. 2004, Vol. 10, No. 6
66. Crenn, J.P., "Optical study of the EH<sub>11</sub> mode in a hollow circular oversized waveguide and Gaussian approximation of the far-field pattern", *Applied Optics*, Oct. 1984, Vol. 23, No. 19
67. Marcatili, E., and Schmeltzer, R., "Hollow metallic and dielectric waveguides for long distance optical transmission and lasers", *Bell Systems Technical Journal*, July 1964, pp. 1783-1809
68. S. M. Howdle, K. Stanley, V.K. Popov, V.N. Bagratashvili, "Can high-pressure Raman spectroscopy be simplified? A microscale optical-fiber capillary cell for the study of supercritical fluids", *Applied Spectroscopy*, 48, 214, (1994)
69. S. D. Schwab, R.L. McCreery, "Remote, long-pathlength cell for high-sensitivity Raman spectroscopy", *Applied Spectroscopy*, 41, 126, (1987)

70. William F. Pearman, J. Chance Carter, S. Michael Angel, and James Wai-Jeung Chan, "Multipass Capillary Cell for Enhanced Raman Measurement of Gases," *Appl. Spec.* 62, 285 (2008)
71. William F. Pearman, J. Chance Carter, S. Michael Angel, and James Wai-Jeung Chan, "Quantitative measurements of CO<sub>2</sub> and CH<sub>4</sub> using a multipass Raman capillary cell," *Appl. Opt.* 47, 4627 (2008)
72. R. M. Flores, V. G. McDonell, and G. S. Samuelsen, "Impact of Ethane and Propane Variation in Natural Gas on the Performance of a Model Gas Turbine Combustor," *J. Eng. Gas Turbines and Power* 125 (2003) 701
73. R. L. Hack and V. G. McDonell, "Impact of Ethane Propane and Diluent content in Natural Gas on the Performance of a Commercial Microturbine Generator," *Proc ASME Turbo Expo 2005: Power for Land, Sea and Air*, June 6-9, 2005, Reno-Tahoe, Nevada, USA
74. D. Ferguson, G. A. Richard, and D. Straub, "Fuel Interchangeability for Lean Premixed Combustion in Gas Turbine Engines," *Proc ASME Turbo Expo 2008: Power for Land, Sea and Air*, June 9-13, 2008, Berlin, Germany
75. N. Slavinskaya, M. Braun-Unkloff, and P. Frank, "Reduced Reaction Mechanisms for Methane and Syngas Combustion in Gas Turbines," *J. Eng. Gas Turbines and Power* 130 (2008) 021504-1
76. C. Prathap, Anjan Ray, and M. R. Ravi, "Investigation of nitrogen dilution effects on the laminar burning velocity and flame stability of syngas fuel at atmospheric condition," *Combust. Flame* 155 (2008) 145-160
77. Stratton, J.A., "Electromagnetic theory", McGraw-Hill, P.524, 1942
78. Figure courtesy of Steven Woddruff, National Energy Technology Laboratory; Morgantown, WV